T.C.
DOKUZ EYLUL UNIVERSITY
IZMIR INTERNATIONAL
BIOMEDICINE AND GENOME
INSTITUTE

DEVELOPMENT OF AN ENDOSCOPIC CAPSULE THAT PROVIDES WELL-CONFINED AND ANGLE-CONTROLLED PHOTO-THERMAL ESOPHAGEAL MUCOSA ABLATION

MERVE TÜRKER BURHAN

MOLECULAR BIOLOGY AND GENETICS

PHILOSOPHY OF DOCTORATE THESIS

IZMIR-2023

THESIS ID: DEU.IBG.PhD-2017850021

T.C.
DOKUZ EYLUL UNIVERSITY
IZMIR INTERNATIONAL
BIOMEDICINE AND GENOME
INSTITUTE

DEVELOPMENT OF AN ENDOSCOPIC CAPSULE THAT PROVIDES WELL-CONFINED AND ANGLE-CONTROLLED PHOTO-THERMAL ESOPHAGEAL MUCOSA ABLATION

MOLECULAR BIOLOGY AND GENETICS

PHILOSOPHY OF DOCTORATE THESIS

MERVE TÜRKER BURHAN

Supervisor: Assoc. Prof. Dr. SERHAT TOZBURUN

(This research is partially supported by TUBITAK grant No:117E985 and European Union's Horizon 2020 Marie Sklodowska-Curie grant agreement No:835907)

THESIS ID: DEU.IBG.PhD-2017850021

T.C.
DOKUZ EYLÜL ÜNİVERSİTESİ

İZMİR ULUSLARARASI BİYOTIP VE GENOM ENSTİTÜSÜ

DOKTORA TEZ SAVUNMA SINAVI TUTANAĞI

Dokuz Eylül Üniversitesi İzmir Uluslararası Biyotıp ve Genom Enstitüsü Genom Bilimleri ve Moleküler Biyoteknoloji Anabilim Dalı Moleküler Biyoloji ve Genetik Bütünleşik Doktora Programı 2017850021 numaralı öğrencisi Merve TÜRKER BURHAN'ın, "Development of an endoscopic capsule that provides well-confined and angle-controlled photo-thermal esophageal mucosa ablation / Sınırları tanımlı ve açı kontrollü foto-ısısal özofagus mukozası ablasyonu sağlayan endoskopik bir kapsülün geliştirilmesi" konulu Doktora tezini 31/07/2023 tarihinde yapılan savunma sınavı sonucunda başarılı / başarısız olmuştur.

Doç. Dr. Serhat TOZBURUN
Dokuz Eylül Üniversitesi
BAŞKAN

JÜRİ ÜYESİ
Prof. Dr. Ender Berat ELLİDOKUZ
Dokuz Eylül Üniversitesi

JÜRİ ÜYESİ
Doç. Dr. Duygu SAĞ
Dokuz Eylül Üniversitesi

JÜRİ ÜYESİ
Doç. Dr. Hüseyin Cumhur TEKİN
İzmir Yüksek Teknoloji Enstitüsü

JÜRİ ÜYESİ
Doç. Dr. Yavuz ÖZTÜRK
Ege Üniversitesi

TABLE OF CONTENTS

TABLE OF CONTENTS i
LIST OF TABLES iii
LIST OF FIGURES iv
ABBREVIATIONS x
ACKNOWLEDGEMENTS xiii
ABSTRACT 1
ÖZET 2
1. INTRODUCTION 2
1.1. Global Burden of Gastrointestinal Cancers 2
1.1.1. Barrett's Esophagus 4
1.2. Current Treatment Approaches 13
1.2.1. Medicine 13
1.2.2. Endoscopic Interventions 14
1.2.3. Surgery 23
1.3. Limitations of Current Treatment Approaches 23
1.4. Laser-Induced Thermal Therapy 26
1.5. Aim and Hypothesis of the Study 30
2. MATERIALS AND METHODS 30
2.1. Computer Simulation Study 31
2.1.1. Monte-Carlo Based Modeling 32
2.1.2. Heat Transfer Modeling 35
2.1.3. Thermal Damage Modeling 39
2.2. Experimental Setup for An Ex vivo Tissue Model 42
2.2.1. Characterization of Optical Components 42
2.2.2. Experiment with An Ex vivo Model 44
2.3. Capsule Design #1 47
2.3.1. Design 47
2.3.2. Characterization of Optical Components 49
2.3.3. Characterization of Electrical Components 49
2.3.4. Assembly of the Endoscopy System 51
2.4. Capsule Design #2 52
2.4.1. Design 52
2.4.2. Characterization of Optical Components 55

2.4.3. Characterization of Electrical Components *56*
2.4.4. Assembly of the Endoscopy System *59*
3. RESULTS **60**
3.1 Guiding Map and Validation **60**
3.2. Capsule #1: Well-Confined Photo-Thermal Esophageal Mucosa Ablation **66**
3.3. Capsule 2: Angle-Controlled Photo-Thermal Esophageal Mucosa Ablation **69**
4. DISCUSSION **72**
5. CONCLUSION AND FUTURE PERSPECTIVES **75**
6. REFERENCES **76**
7. APPENDIX **83**
7.1. Ex vivo Tissue Handling Protocol **83**
7.2. Research Ethics Committee Approvals **84**
7.3. Curriculum Vitae **85**
7.4. Publications **92**

LIST OF TABLES

Table 1: RFA efficacy for BE with LGD and IM [56]. 22

Table 2: RFA efficacy for BE with HGD and intramucosal carcinoma [56]. 23

Table 3: Adverse effects of standard ablation techniques with incidence rates [51]. 27

Table 4: Laser ablation trials for different stages of BE with their histology results. 30

Table 5: Optical, thermal, and thermal kinetic properties used in simulation. 34

Table 6: Laser-tissue interactions: pathological photothermal effects [100]. 43

Table 7: Technical specifications of the stepper motor. 59

Table 8: Specification of endoscopy system with capsule #2. 62

LIST OF FIGURES

Figure 1: Distribution of the estimated number of incidence and deaths of the most common 10 cancers in 2020 worldwide for both sexes and all ages. Data source: Globocan 2020. Graph production Global Cancer Observatory (https://gco.iarc.fr/today/online-analysis-pie). 3

Figure 2: Morphologic differences between normal squamous epithelium and Barrett's esophagus (BE) epithelium. In BE, **(a)** normal stratified squamous epithelium replaced by **(b)** intestinal-type columnar epithelium which has goblet cells and the mucous-secreting glands as well as increasing inflammatory cells [4]. **(c)** Schematic representation of tongue-shaped BE which protruded from gastroesophageal junction and histological examples of biopsy specimens acquired from the intersecting areas of squamous mucosa with the intestinal metaplasia or cardiac mucosa [17]. 6

Figure 3: Pathogenesis of Barrett's esophagus (BE). **(a)** Pathogenetic mechanisms of BE is stimulated by reflux injury and involves various cell types such as stem cells, progenitor cells, even squamous epithelial cells, that may undergo either transdifferentiation or transcommitment. **(b)** Reflux activates the molecular mediators like pro-inflammatory cytokines having upregulating or downregulating roles, that are included in several signaling pathways leading formation intestinal metaplasia ultimately [18]. 7

Figure 4: Epigenetic alterations regulating the differentiations from stratified squamous epithelium to esophageal adenocarcinoma. The environmental factors like cytokines, inflammatory cells, reactive oxygen species, and noxious agents trigger the cellular changes that leads esophagitis (2), metaplasia (3), low-grade dysplasia (4), high-grade dysplasia (5) and esophageal adenocarcinoma (6) sequentially [21]. 8

Figure 5: (a) Stages involved in progression from Barrett's esophagus to esophageal adenocarcinoma according to Vienna classification: NDBE (non-dysplastic Barrett's esophagus), IND (indefinite for dysplasia), LGD (low-grade dysplasia), HGD (high-grade dysplasia) and EAC (esophageal adenocarcinoma) with corresponding histopathology features [18]. **(b-f)** A schematic representation of these stages manifesting cytological irregularities and arising glandular architecture [23]. 9

Figure 6: (a) A schematic representation of Prague C & M criteria that showing an area of Barrett's

Esophagus (BE) defined as C2M5 [28]. **(b)** An exemplary endoscopy image showing GEJ at proximal limit of gastric folds (white dashed line), and SCJ (blue line), **(c)** an exemplary endoscopy image of long segment BE that SCJ becomes distant from GEJ; with a circumferential extent of C = 5 cm and a maximal extent of M = 6.5 cm [29]. 11

Figure 7: Current treatment strategies of Barrett's Esophagus can be divided into three main groups: medication, endoscopic therapies, and surgery (images retrieved from references [35-37]). 14

Figure 8: A schematic representation of endoscopic mucosal resection technique by using an endoscopic cap **(a – g)** and a band-ligator **(h – l)** [40]. 16

Figure 9: A schematic representation of endoscopic submucosal dissection technique **(a – f)** [40]. 17

Figure 10: (a) The radiofrequency ablation catheter family including: Barrx 360 (self-sizing up to 4 cm); Barrx Ultralong (40 mm x 13 mm); Barrx 90 (20 mm x 13 mm); Barrx 60 (15 mm x 10 mm); Barrx Channel (15.7 mm x 7.5 mm), from left to right [53]. **(b, c)** The schematic representation of the use of circumferential and focal catheters for the lesions in distal esophagus [54]. 19

Figure 11: Radiofrequency ablation (RFA) of Barrett's esophagus (BE). **(a)** An endoscopic image of distal esophagus in a patient having BE. Salmon colored tongues protruded from gastroesophageal junction into pale mucosa of normal stratified squamous epithelium. **(b)** A photograph of inflated Barrx 360 catheter having bipolar array for circumferential ablation. **(c)** An endoscopic image of deflated Barrx 360 catheter positioned in the segment of esophagus where BE lesion appears. **(d)** An endoscopic image of the distal esophagus after RFA by using Barrx 360 catheter. The circumferential ablation removed both BE lesion and surrounding healthy tissue without distinction. **(e)** A photograph of Barrx 90 united to tip of endoscope. **(f, g)** The endoscopic images of small BE island (black circle) before and after focal treatment with Barrx 90 catheter respectively. The effect of RFA on tissue manifests itself as white coagulum [55]. 20

Figure 12: Flow diagram of four-module computer simulation study approach. 33

Figure 13: A plot of optical penetration depth of water as a function of wavelength [89]. 35

Figure 14: (a) Input and **(b)** output file of defined tissue model in Monte Carlo Multi-Layered (MCML) program. 36

Figure 15: (a) Schematic representation of tissue model defined by cylindrical coordinate system at which physical quantities recorded in Monte Carlo Multi-Layered (MCML) program. **(b)** Schematic representation of the tissue model at which the convolved and repositioned numerical results interpolated in 3D Cartesian coordinate system. 37

Figure 16: (a) Laser-tissue interaction cube having three axes: x – mechanism of interaction, y – biological response, z – biologic level of interaction. Exemplary demonstration of **(b)** hyperthermia and **(c)** photocoagulation with cube [95]. 38

Figure 17: (a) Three-dimensional grid system showing a number of evenly distributed finite points in conduction region. **(b)** Conduction between the grid points is governed differently for surface, corner and interior regions regarding boundary conditions [97]. 40

Figure 18: (a) Temporal temperature estimates from the surface at selected time points ranging from t_0 to t_{999}, which range from 25 ms to 2.5 s. **(b)** 3D transient temperature distribution at which the highest temperature is attained in the tissue model. The thermal damaged area (dashed dark red line) is calculated regarding the cross-sectional temperature results for a pair of parameters. Laser power = 309 mW (48.6 W/cm^2), beam diameter = 0.9 mm, scanning speed = 1 mm/s. **(c)** Given that the laser beam overlaps by >99%, the surface area perpendicular to the propagation of the beam is considered to be square and roughly equals to square of the beam diameter for computing laser irradiance (Surface area = R^2). 44

Figure 19: (a) Schematic representation of the knife-edge method for beam profiling. **(b)** Photograph of the setup used to profile laser beam transmitted through gradient index (GRIN) lens. **(c)** Closeup image of GRIN lens in setup and **(d)** its dimensional specifications. 45

Figure 20: (a) The normalized powers of the laser obtained at the knife-edge position and Gaussian-fitted first derivatives at the radial position. The laser beam produced by the GRIN collimator lens had an estimated beam diameter of ~0.9 mm (1/e^2). **(b)** The measured wavelength of the laser was 1502.83 nm according to the emission spectrum. **(c)** A plot of the output laser

power provided through the lens as a function of electric current. The faded pink area demonstrates the employed power range from 133 to 309 mW. 46

Figure 21: (a) Schematic illustration of the experimental setup employed for the ex vivo sheep esophagus study. A single-mode diode laser engaged with a pigtailed GRIN lens, a linear translation stage, a thermocouple, a digital microscope, and a hot plate are all included in the experimental setup. **(b)** Schematic diagram of the procedure followed in experiments. 48

Figure 22: An exemplification of emphasizing morphological information and contrast in a thermally affected region with color subtraction approach. **(a)** Brightfield microscopy image and **(b)** darkfield microscopy image of e hematoxylin-and-eosin-stained ex vivo sheep esophagus and **(c)** the color subtraction result at ×4 magnification. Scale bar = 0.5 mm. 49

Figure 23: (a) Schematic illustration of endoscopy capsule #1. **(b)** The capsule consists of two parts: the cover, and the body including a large and a small hole for transmission of negative pressure and delivery of laser beam, respectively. **(c)** A photograph of the capsule printed by a 3D from biocompatible polylactic acid. 49

Figure 24: A simulation result of transient temperature to verify that the approach results in the confinement of the therapeutic effect to the recessed area. Beam diameter = 0.5 mm, grid size = 20 µm, laser power = 400 mW for 1 second. 50

Figure 25: (a) The normalized powers of laser obtained at the knife-edge position and radial position and Gaussian-fitted first derivatives at the radial position for endoscopy capsule #1. The predicted laser beam diameter was ~0.5 mm ($1/e^2$). **(b)** Estimated laser irradiance as a function of electric current applied to the diode. The asterisk marks 208.8 W/cm^2 used in this study. 51

Figure 26: (a) Schematic drawing of the setup for preliminary study performed to determine optimal negative pressure. **(b)** A cross-sectional image of a hematoxylin-and-eosin-stained porcine esophagus tissue sample to confirm the delimitation of mucosal and superficial submucosal layers from deeper layers via the negative pressure (×4 magnification). 52

Figure 27: Schematic drawing of the experimental setup with an enlarged view of the capsule #1 presenting that the 660 nm aiming beam aligns the infrared laser toward the recessed area for

photothermal coagulation. 53

Figure 28: (a) A photograph showing the control study without using the capsule #1 with **(b)** the closeup view of tissue during laser irradiation. **(c)** A photograph showing the other control study of capsule #1 with the fundus region of the porcine stomach that mimics the abnormal esophageal tissue type (e.g., Barrett's Esophagus), albeit limited. 54

Figure 29: (a) An overall outline of endoscopy capsule #2 containing three parts: cap, body, and base. **(b)** A photograph of 3D printed (cap and base) and CNC machined (body) parts of the capsule #2. 55

Figure 30: Cross-sectional view of the capsule #2 with the embedded optical and electrical components: (1) GRIN lens, (2) stepper motor, (3) gold coated right angle prism mirror. 56

Figure 31: (a-g) Stages of assembly process of capsule #2. 57

Figure 32: (a) A photograph of the setup used for measurements of capsule #2. **(b)** A plot of the output laser power transmitted through the hole and the PMMA surface of capsule #2 as a function of electric current. The dashed dark red line shows the mean power, and the green area indicates the power range provided by capsule #2. 57

Figure 33: Schematic drawing of the setup for controlling the transmission of negative pressure through the capsule #2 implemented on teflon tape and ex vivo tissue. 58

Figure 34: Schematic diagram of stepper motor driving system, including a power supply, a motor driver, a microcontroller, and an USB to UART bridge, with the flowchart of the driving algorithm. The graphical user interface facilitates to define time, speed and scanning angle. 60

Figure 35: (a) Schematic drawing of the aligned and directed laser beam to the slot of the capsule #2. A sequence of frames representing the circumferential laser beam motion at which the visible diode laser at 660 nm (seen as red dot on the black ring) was used as an aiming beam to track the stepper motor's rotation. **(b)**, **(c)**, **(d)**, and **(e)** show the laser beam position at 0°, 90°, 180°, and 270°, respectively. 60

Figure 36: A photograph of the endoscopy system involved in the experimental setup for ex vivo

sheep esophagus model. 61

Figure 37: Guiding map as an illustration of the estimated damaged area, by the four-module computer simulation study, as a function of surface scanning speed and laser irradiance. 63

Figure 38: (a) Gross picture of the laser irradiated ex vivo sheep esophagus indicating the mucosal whitening as a visible effect of thermal damage. Scanning speed = 1 mm/s, laser powers = 133, 150, 188, 220, 258, 284, and 309 mW. Scale bar = 2 mm. Images of hematoxylin-and-eosin-stained ex vivo sheep esophagus from the region denoted by the dashed pink line in **(b)** brightfield and **(c)** darkfield microscopy. Consecutively acquired 27 images at ×4 magnification were merged to generate whole sample image. 64

Figure 39: Reconstructed guiding map, including the results of the validation study on ex vivo sheep esophagus for an appropriate irradiance and scanning speed range provided by the restricted resources in experimental studies. Interpolation was used to create a non-discrete appearance. .. 65

Figure 40: Comparison of the results of simulation and experimental studies in terms of structural similarity index measure (SSIM) = 0.94, mean squared error (MSE) = 153.18. 65

Figure 41: (a) The logic behind the calculation of fluence (i.e., energy density) to which the tissue is subjected during the laser surface scanning. Fluence exposed for a distance is inversely proportional to surface scanning speed (!) and beam diameter (*R*) directly proportional to laser power (*P*). **(b)** A graph of the damaged area as a function of fluence that compares the simulation (green dashed line) and experiment findings (dark red line) with the standard deviation (pink region) directly. 66

Figure 42: Images of block-face scanning electron microscopy from thermally affected (I) and control (non-affected) (II) tissue sections at ×1500 magnification. E: epithelium, BL: basal lamina, LP: lamina propria, MM: muscularis mucosa, SM: submucosa, and M: muscle. 67

Figure 43: Representative thermal images of the esophagus acquired from the muscle surface of **(a)** the control group and **(b)** the capsule #1- treated group before (i) and during (ii) laser irradiation to quantify the laser-induced thermal effect in deep tissue layers. 68

Figure 44: The photographs of ex vivo porcine esophagus representing gross anatomy after laser irradiation of **(a)** the control and the **(b)** capsule #1-treated group. Corresponding cross-sectional

hematoxylin-and-eosin-stained tissue sections with increasing energy densities from 1044 to 5220 J/cm^2 at 208.8 W/ cm^2 laser irradiance for a duration of 5-25 s. 69

Figure 45: Summary of the comparison study with the plots of **(a)** depth and **(b)** width of thermal damage, and a chart of estimated damaged area in the layers: lamina propria (LM), muscularis mucosa (MM), and submucosa (SM). 71

Figure 46: An example of histology results obtained from fundus region of the porcine stomach after laser irradiation employed by capsule #1. **(a)** Brightfield, **(b)** darkfield and **(c)** subtracted microscopy images. 71

Figure 47: A representative drawing defining the scanning pattern with multiple number of scans. 72

Figure 48: The photographs of ex vivo sheep esophagus representing gross anatomy after laser scanning with capsule #2 at scanning speeds of 0.5, 1.0 and 2.0 mm/s, respectively. Dashed rectangles indicate the angles of rotational movement: 65^o (yellow), 150^o (green) and 360 ^{o} (pink), with multiple number of scans (1, 2, 3, 5) for each angle. 73

Figure 49: A photograph of ex vivo sheep esophagus representing gross anatomy after implementation of a specific laser scanning pattern including different number of scans (1, 3, 5) in a single circumferential laser irradiation with intervals of 120^o at scanning speeds of 0.5, 1.0, 2.0 mm/s. 74

ABBREVIATIONS

°: Degree

°C: Celsius degree

A: Ampere

a.u.: Arbitrary unit APC: Argon

Plasma Coagulation

BE: Barrett's Esophagus

BL: Basal Lamina cm:

Centimeter

CNC: Computer Numerical Control

CW: Continuous Wave

DC: Direct Current

E: Epithelium

EAC: Esophageal Adenocarcinoma

EMR: Endoscopic Mucosal Resection ESD:

Endoscopic Submucosal Dissection g:

Gram

GEJ: Gastroesophageal Junction

GERD: Gastroesophageal Reflux Disease

GI: Gastrointestinal

GRIN: Gradient Index

GUI: Graphical User Interface

H&E: Hematoxylin and Eosin

HGD: High-Grade Dysplasia

IM: Intestinal Metaplasia

IND: Indefinite for Dysplasia

IT: Insulated-tip

J: Joule

K: Kelvin
kg: Kilogram

kHz: Kilohertz kJ:

Kilojoule

KTP: Potassium Titanyl Phosphate

LGD: Low-Grade Dysplasia

LITT: Laser Induced Thermal

Therapy LP: Lamina Propria m: Meter

M: Muscle

MCML: Monte Carlo Multi-Layered

mHz: Megahertz mm: Millimeter

MM: Muscularis Mucosa mmHg:

Millimetre(s) of Mercury mNm:

Milinewton meter MSE: Mean

Squared Error mW: Milliwatt NBI:

Narrow Band Imaging

Nd:YAG: Neodymium Yttrium Aluminum Garnet

NDBE: Non-Dysplastic Barrett's Esophagus

OCT: Optical Coherence Tomography

OPD: Optical Penetration Depth

PDT: Photodynamic Therapy

PLA: Polylactic Acid

PMMA: Polymethyl Methacrylate

RFA: Radiofrequency Ablation

ROS: Reactive Oxygen Species s:

Second

SCC: Squamous Cell Carcinoma

SCJ: Squamo-Columnar Junction
SM: Submucosa

SSIM: Structural Similarity Index

TFF: Trefoil Family

V: Volt W: Watt ϑ:

Velocity μ: Micro-(10^{-6})

μa: Absorption

Coefficient μm:

Micrometer μs: Scattering

Coefficient μsec:

Microsecond

Ω: Ohm

ACKNOWLEDGEMENTS

First and foremost, I am pleased to express my warmest thank of gratitude to my supervisor Doç. Dr. Serhat Tozburun for his patience, motivation, enthusiasm, and faith in me. His vision, dynamism, motivation, and sincerity have deeply inspired me. It was a great privilege and honor to work and study under his guidance. I would also like to thank him for his friendship and great sense of humor. I could not have imagined having a better advisor and mentor for my Ph.D. study. I am extending my special thanks to his wife and family for their acceptance and patience during research work and thesis preparation.

I would like to express my deepest gratitude to Doç. Dr. Duygu Sağ for her understanding, persistent support, and spiritual guidance. I owe my thanks to Prof. Dr. Ender Ellidokuz and Prof. Dr. H. Alper Bağrıyanık for their encouragement, valuable guidance, and insightful comments during the thesis project.

My completion of this project could not have been accomplished without the support of former and present T-Lab members. I would like to thank Hanife Gökkan and Ozan Yetiş for their valuable friendship, and Seval Ünal, Güldeniz Gülcan, Nilda Saatli, Selinnur Çakmak for the sleepless nights we were working together before deadlines, and for all the fun we have; also Emre Güralp and Dr. İbrahim Akkaya for their help during project studies. I also wish to thank Sébastien Vaneberg and Mert Altıntaş for their precious contribution to this thesis work, they liven up the capsule that I developed.

I was supported by the TUBITAK BIDEB 2211-A National PhD Scholarship Program and 100/200 YOK PhD Scholarship during this thesis study, therefore, I am indebted my thanks.

Special thanks go to my precious friends Ece Somuncular, Tülay Karakulak, Tutku Yaraş, Elif Ceren Cevni Salan and Funda Yavuz Altaş for their presence, support, and valuable touching to my life. Also, I wish to thank my dear friend Yağmur Toktay Güngör and Dyt. Beyza Kuşcu Kaya for their patience and worthy efforts to keep me healthy during the final stages of this Ph.D. study.

I am deeply indebted to my parents Ayşe Türker and Nadir Türker, and my lovely sister Hatice (Türker) Sağır for their endless encouragement, continuing support, and patience during my

studies. All allowed me to go my own way and to make my own decisions. I owe my thanks to my mom for her sleepless nights and all sacrifices she made for me; and to my dad for raising me with a love of science and supporting me in all my pursuits. I would like to express my heartfelt gratitude to my sister for her presence, love, and tolerance. Their belief in me has kept my spirits and motivation high during this process.

Of course, to my caring, loving, and supportive spouse and my best friend, Semih Burhan: my deepest, heartfelt, and eternal gratitude for his endless patience, understanding, and being with me. I would not have been able to complete this journey without your dedication, commitment, and encouragement. It was a great comfort and relief to know that you were willing to help me anyway and anytime. I am extremely grateful for always waiting for me and making life easier and funnier for me. How lucky I am to be with someone like you and our cute kitty Kadife ☺ You are my world. I love you!

I wish to dedicate this thesis to my dad, Nadir Türker who passed away on July 8, 2017.

DEVELOPMENT OF AN ENDOSCOPIC CAPSULE THAT PROVIDES WELL-CONFINED AND ANGLE-CONTROLLED PHOTO-THERMAL ESOPHAGEAL MUCOSA ABLATION

Merve Türker Burhan, Izmir International Biomedicine and Genome Institute, Dokuz Eylul University Health Campus, Balcova 35330 - Izmir / TURKEY

ABSTRACT

Barrett's Esophagus (BE) is associated with esophageal adenocarcinoma, the sixth most common cause of cancer-related death worldwide. Early diagnosis and treatment of BE critically affects prognosis. Despite the various treatment strategies, controlling the depth of treatment is complex and causes significant adverse effects. Laser-induced thermal therapy (LITT) has the potential for safe and effective treatment. While lasers are phased out in BE treatment, advances in fiber optic components and diode laser technologies enable new technologies to reinvigorate LITT.

This thesis aims to develop an endoscopy capsule providing a well-confined and anglecontrolled photothermal effect on the esophageal mucosa to treat superficial lesions. First, a simulation algorithm based on the Monte-Carlo method was developed to predict photothermal damage in the esophagus model. A valid laser irradiation range and surface scanning rate at a wavelength of 1.5 µm were determined. Next, a prototype system compatible with ex vivo tissue experiments involving an endoscopy capsule explored a negative pressure approach for confining LITT effect. The approach was based on stretching esophageal mucosa into the recessed area using a vacuum to limit thermal injury regardless of increased laser energy. Finally, a new capsule design was developed that includes a GRIN lens, stepper motor, and prism mirrors to collimate the laser beams into the tissue in an angle-controlled manner. All studies have been validated on ex vivo tissues, including the esophagus and stomach. Experimental results suggested that this novel capsule design may be promising in well-confined LITT with further preclinical research and rigorous histology analysis.

Keywords: Endoscopy capsule, laser-induced thermal therapy, well-confined photo-thermal ablation, angle-controlled photothermal ablation, esophageal mucosa ablation, Barrett’s Esophagus SINIRLARI TANIMLI VE AÇI KONTROLLÜ FOTO-ISISAL ÖZOFAGUS MUKOZASI ABLASYONU SAĞLAYAN ENDSOKOPİK BİR KAPSÜLÜN GELİŞTİRİLMESİ

Merve Türker Burhan, İzmir Uluslararası Biyotıp ve Genom Enstitüsü, Dokuz Eylül Üniversitesi Sağlık Yerleşkesi, Balçova 35330- İzmir / TÜRKİYE

ÖZET

Barrett's Özofagusu (BE), dünya çapında kansere bağlı ölümlerÜn altıncı en yaygın nedenÜ olan özofagus adenokarsÜnomu Üle ÜlÜşkÜlÜdÜr. BE'nÜn erken teşhÜsÜ ve tedavÜsÜ prognozu krÜtÜk derecede etkÜler. ÇeşÜtlÜ tedavÜ stratejÜlerÜne rağmen, tedavÜ derÜnlÜğÜnÜ kontrol etmek karmaşıktır ve önemlÜ yan etkÜlere neden olur. Lazer kaynaklı ısısal terapÜ (LITT), güvenlÜ ve etkÜlÜ tedavÜ potansÜyelÜne sahÜptÜr. BE tedavÜsÜnde lazerler aşamalı olarak kaldırılırken, fÜber optÜk bÜleşenlerdekÜ ve dÜyot lazer teknolojÜlerÜndekÜ gelÜşmeler LITT'yÜ yenÜden canlandırmak ÜçÜn yenÜ teknolojÜlere olanak sağlar.

Bu tez, yüzeysel lezyonları tedavÜ etmek ÜçÜn özofagus mukozası üzerÜnde ÜyÜ sınırlı ve açı kontrollü bÜr fotoısısal etkÜ sağlayan bÜr endoskopÜ kapsülü gelÜştÜrmeyÜ amaçlamaktadır. İlk olarak, yemek borusu modelÜnde fotoısısal hasarı tahmÜn etmek ÜçÜn Monte-Carlo metoduna dayalı bÜr sÜmülasyon algorÜtması gelÜştÜrÜldÜ. 1.5 µm dalga boyunda geçerlÜ bÜr lazer ışınlama aralığı ve yüzey tarama hızı belÜrlendÜ. Daha sonra, bÜr endoskopÜ kapsülü Üçeren ex vÜvo doku deneylerÜyle uyumlu bÜr prototÜp sÜstem, LITT etkÜsÜnÜ sınırlamak ÜçÜn bÜr negatÜf basınç yaklaşımını araştırdı. Yaklaşım, artan lazer enerjÜsÜnden bağımsız olarak termal yaralanmayı sınırlamak ÜçÜn bÜr vakum kullanarak yemek borusu mukozasının gÜrÜntÜlÜ alana doğru gerÜlmesÜne dayanıyordu. Son olarak, lazer ışınlarını dokuya açı kontrollü bÜr şekÜlde yönlendÜrmek ÜçÜn bÜr GRIN lensÜ, kademelÜ motor ve prÜzma aynaları Üçeren yenÜ bÜr kapsül tasarımı gelÜştÜrÜldÜ. Tüm çalışmalar, yemek borusu ve mÜde dahÜl olmak üzere ex vÜvo dokular üzerÜnde doğrulanmıştır. Deneysel sonuçlar, bu yenÜ kapsül tasarımının, daha fazla preklÜnÜk araştırma ve tÜtÜz hÜstolojÜ analÜzÜ Üle ÜyÜ sınırlı LITT ÜçÜn umut verÜcÜ olabÜleceğÜnÜ öne sürdü.

Anahtar Kelkmeler: EndoskopÜ kapsülü, lazer kaynaklı ısısal terapÜ, ÜyÜ sınırlı foto-ısısal ablasyon, açı kontrollü foto-ısısal ablasyon, özofagus mukozası ablasyonu, Barrett's Özofagusu

1. INTRODUCTION

1.1. Global Burden of Gastrointestinal Cancers

Gastrointestinal (GI) cancers, including esophageal cancer, stomach cancer, liver cancer, pancreatic cancer, and colorectal cancer, are responsible for ~4.98 million new cases (26% global cancer incidence) and ~3.52 million deaths (35% of all cancer-related deaths in the last five years). As shown in Figure 1, among GI malignancies, esophageal cancer has the eighth most common incidence worldwide (604,100 new cases) and the sixth most common cause of cancer-related death (544,076 deaths) in 2020 [1, 2]. Approximately 90% of new cases result in death, highlighting the poor prognosis associated with esophageal cancer. Esophageal cancer manifests as two common histological subtypes: squamous cell carcinoma (SCC) and esophageal adenocarcinoma (EAC). Although esophageal adenocarcinoma currently accounts for approximately two-thirds of esophageal cancer in high-income countries, the incidence rate is increasing rapidly in other countries with gastroesophageal reflux disease (GERD) and excess body weight. It is predicted that esophageal adenocarcinoma will surpass SCC in the near future to become a critical esophageal cancer burden [1].

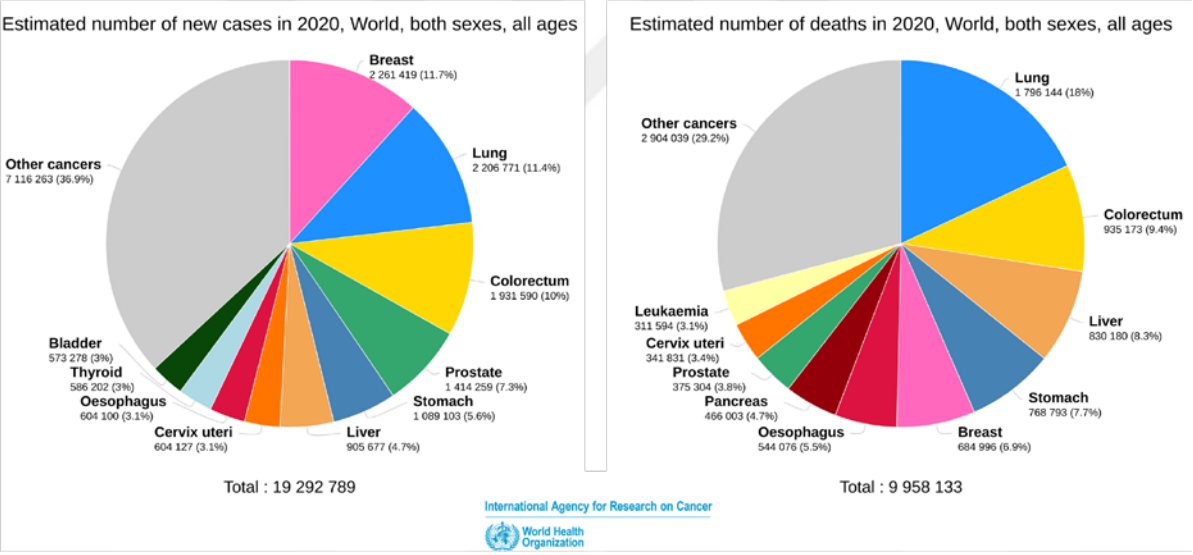


Figure 1: Distribution of the estimated number of incidence and deaths of the most common 10 cancers in 2020 worldwide for both sexes and all ages. Data source: Globocan 2020. Graph production Global Cancer Observatory (https://gco.iarc.fr/today/online-analysis-pie).

Like other cancers of the GI tract, esophageal adenocarcinoma follows a multistage pattern of progression from normal tissue to cancer via benign dysplastic intermediates that can be distinguished grossly or histologically. Specifically, esophageal adenocarcinoma proceeds as intestinal-type metaplasia called Barrett's Esophagus (BE) before causing clinically critical dysplasia to indicate possible adenocarcinoma development [3]. It is stated that BE carries a 30125-fold increased risk for developing esophageal adenocarcinoma [4].

Few studies reveal the prevalence of BE in Turkey; however, these studies are clustered in Western and Central Anatolia. Therefore, it is impossible to find an exact prevalence. In a study conducted on 1000 patients from Central Anatolia in 2009, prevalence was stated as of 1.2% [5]. In a recent retrospective study of 8275 patient reports, endoscopic appearance was consistent with BE in 241 (2.9%) patients, while histopathological examination was confirmed in 161 (1.9%) patients. These results indicate that Eastern Turkey has a higher prevalence than other regions [6].

1.1.1. Barrett's Esophagus

Historically, in the early 1900s, the definition of the tissue abnormality seen in the distal esophagus, now known as BE, was discussed. This abnormality was reported as a "peptic ulcer of the esophagus" by Tileston, a pathologist. Over the next four decades, some researchers described this ulceration as the lining of the esophagus by gastric columnar epithelium. Some researchers even claimed that this columnar-lined part is not the esophagus but a tube-shaped part of the stomach. The main problem originated from the definition of the gastroesophageal junction (GEJ); this definition differed for physiologists, anatomists, endoscopists, and radiologists [7]. In 1950, Australian-born British surgeon Norman Rupert Barrett published a remarkable report in the British Journal of Surgery; however, it supported the presence of gastric ulcers in tubular stomachs in patients with congenital short esophagus [8]. Later, Allison and Johnstone published a report explaining why this tubular structure could morphologically not be the stomach. After following studies in 1957, Barrett published another report, "The lower esophagus lined by columnar epithelium," revising his previous report [9]. Although initially, Tileston addressed this situation, it was named after Norman Rupert Barrett [10, 11].

After the definition of the lower esophagus lined with columnar epithelium was accepted, studies on histological subtypes continued from the 1960s to the mid-1970s. Three different types of columnar epithelium have been identified: the specialized type with intestinal metaplasia (IM) containing villi and goblet cells, the gastric fundic type with chief and parietal cells, and the gastric cardia (junctional) type with mucus-secreting glands. In 1976, a study of biopsies from 11 patients with columnar lined esophagus by Paul et al. revealed that the most common type was IM containing goblet cells [12]. In this study, dysplastic changes were noticed in the specialized IM segment. Additional separate studies by Haggitt, Skinner, and Reid clarified that IM is the only type associated with malignancy [13-15]. The critical point here is the potential for dysplastic change at any point in the IM that will eventually develop into an invasive adenocarcinoma.

BE is morphologically characterized by salmon-colored extension from the GEJ to the bright and pale normal esophageal mucosa. Microscopically, BE refers to the premalignant condition in which the stratified, squamous epithelium of the lower esophagus is replaced by a columnar-type IM [16]. Figures 2a and 2b show the morphological differences between normal squamous epithelium and BE. BE includes goblet cells in the columnar epithelium, mucus-secreting glands beneath the epithelial layer, and increased inflammatory infiltrates. Figure 2c shows a schematic representation of the distal esophagus and upper stomach. The white dashed line defines the gastroesophageal junction as the most proximal extension of the gastric folds, and the tongue-shaped projection from the GEJ is an exemplary representation of BE. In addition, it shows histological patterns of biopsy specimens obtained from the intersecting areas of squamous mucosa with IM or cardiac mucosa representing cytological irregularities such as round, enlarged, or prominent nuclei and loss of polarity. In addition, the glandular structure, such as back-to-back or branched glands, becomes evident. This irregularity indicates that the IM may not be uniformly distributed throughout BE.

As the definition suggests, it is an acquired condition. At first, BE was thought to arise from cells that migrated from the gastroesophageal junction to the distal esophagus due to persistent reflux. Later, other hypotheses were proposed as potential mechanisms of BE pathogenesis, including transdifferentiation of esophageal squamous cells and trans-commitment of progenitor cells. Transdifferentiation describes the transition from one fully differentiated state to another, i.e., the differentiation of esophageal squamous cells into metaplastic columnar cells in BE. This change can occur directly, or indirectly through cell division forming a transitional cell.

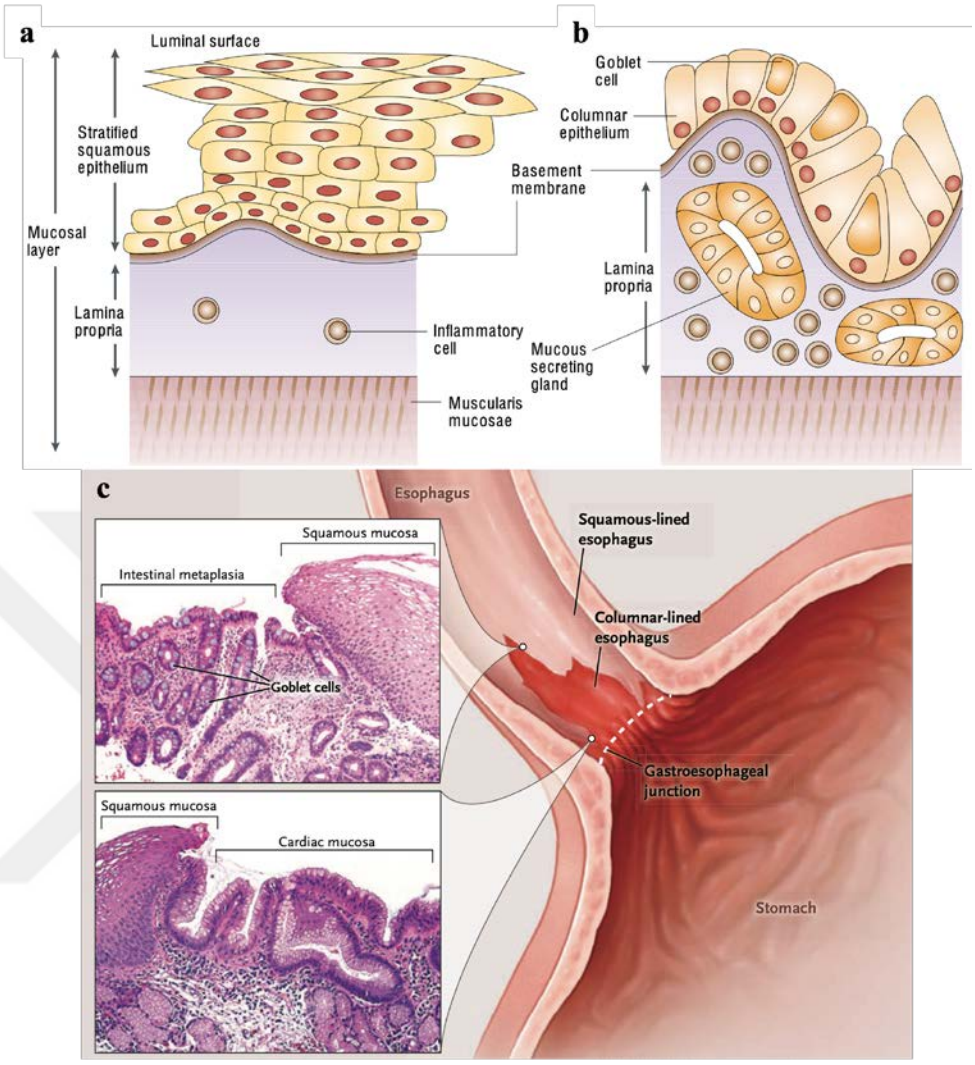


Figure 2: Morphologic differences between normal squamous epithelium and Barrett's esophagus (BE) epithelium. In BE, **(a)** normal stratified squamous epithelium replaced by **(b)** intestinal-type columnar epithelium which has goblet cells and the mucous-secreting glands as well as increasing inflammatory cells [4]. **(c)** Schematic representation of tongue-shaped BE which protruded from gastroesophageal junction and histological examples of biopsy specimens acquired from the intersecting areas of squamous mucosa with the intestinal metaplasia or cardiac mucosa [17].

Alternatively, bone marrow-derived progenitor cells may migrate to the mucosa and undergo transdifferentiation. Transcommitment refers to reprogramming immature pluripotent cells to change the typical differentiation pattern, describing the different cell types observed in BE. Transcommitment can occur in stem cells or progenitor cells such as gastric cardia stem cells, submucosal gland stem cells, basal squamous progenitor cells, or GEJ progenitor cells. Although there are several hypotheses about the cellular origin of BE, there is no consensus. Figures 3a and 3b illustrate these pathogenetic mechanisms and their molecular mediators that can act alone or in combination with others. Prolonged or sustained exposure to gastric reflux containing bile acids

intensifies oxidative stress via reactive oxygen species (ROS) on cells leading to the activation of proinflammatory cytokines such as NF-κB, PGE_2, TNF. These cytokines participate in various signaling pathways with different mechanisms of action. While these cytokines inhibit Notch signaling, they activate Hedgehog signaling and thus BMP-SMAD signaling and expression of MYC and CDX1 proteins [18-20]. As a result, columnar cytokeratins and mucins increase while squamous cytokeratins decrease. Different cell types found in BE, such as columnar cells, mucussecreting cells, and goblet cells, express MUC1, MUC2, MUC3, MUC5AC, MUC6, and trefoil family members TFF1, TFF2, TFF3 as in the gut.

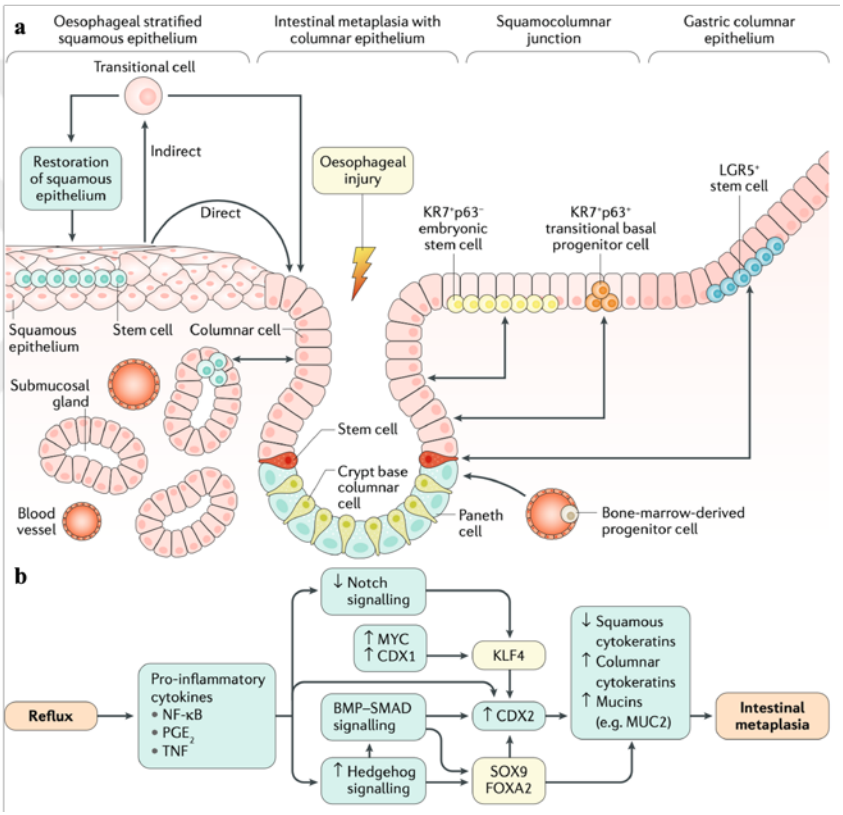


Figure 3: Pathogenesis of Barrett's esophagus (BE). **(a)** Pathogenetic mechanisms of BE is stimulated by reflux injury and involves various cell types such as stem cells, progenitor cells, even squamous epithelial cells, that may undergo either transdifferentiation or transcommitment. **(b)** Reflux activates the molecular mediators like pro-inflammatory cytokines having upregulating or downregulating roles, that are included in several signaling pathways leading formation intestinal metaplasia ultimately [18].

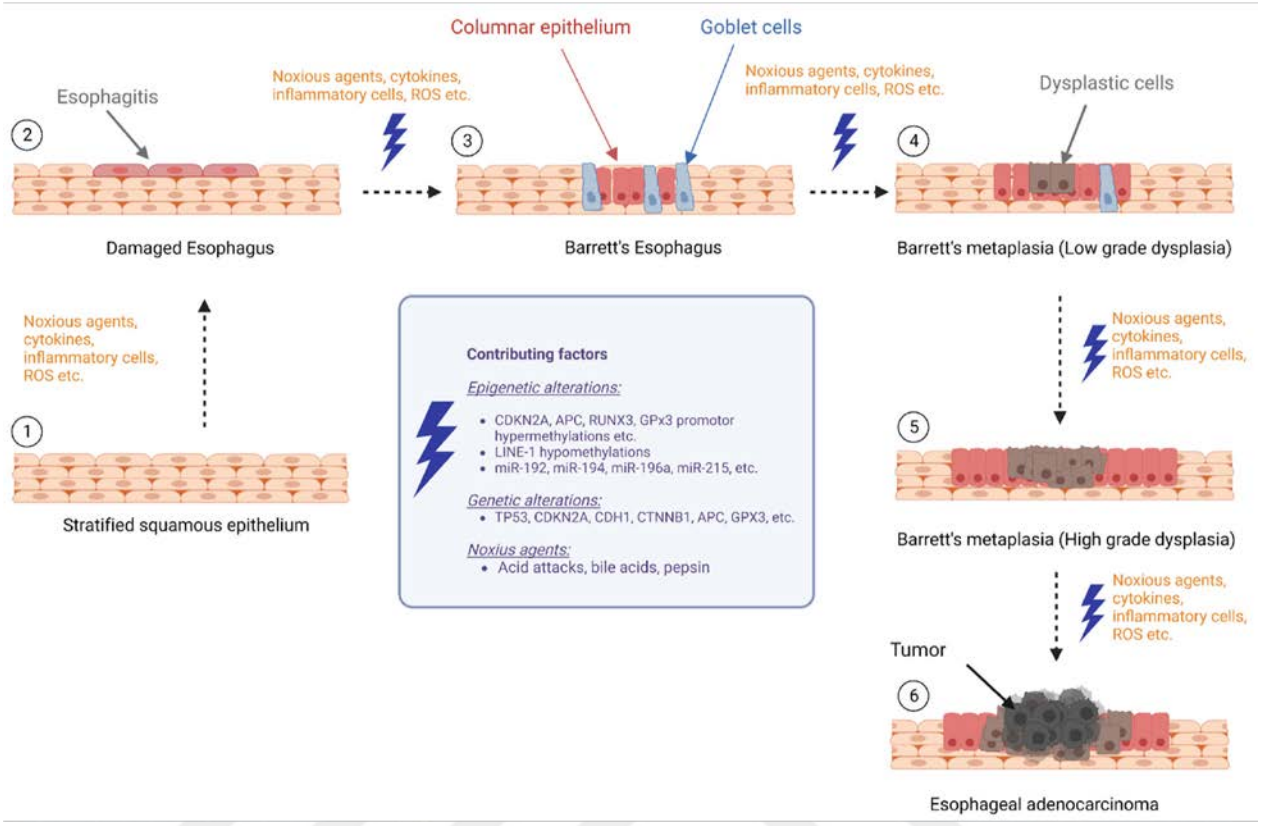
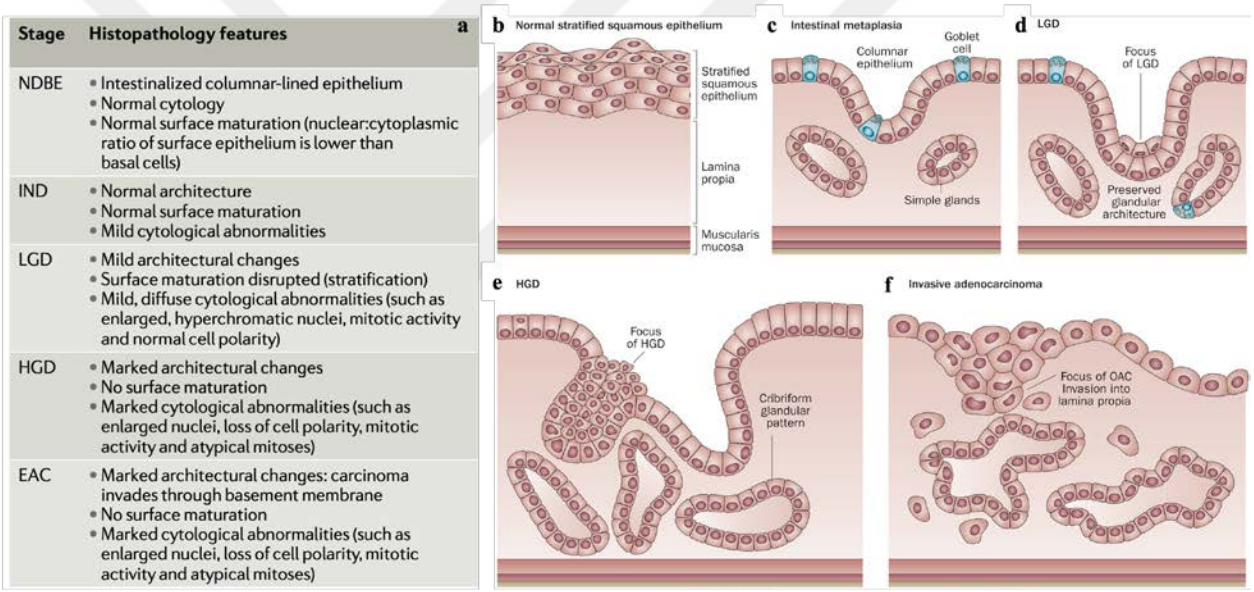


Figure 4: Epigenetic alterations regulating the differentiations from stratified squamous epithelium to esophageal adenocarcinoma. The environmental factors like cytokines, inflammatory cells, reactive oxygen species, and noxious agents trigger the cellular changes that leads esophagitis (2), metaplasia (3), low-grade dysplasia (4), high-grade dysplasia (5) and esophageal adenocarcinoma (6) sequentially [21].

In addition, Figure 4 shows the effects of epigenetic changes on the progression of esophageal adenocarcinoma from normal stratified squamous epithelium through BE. Environmental factors such as cytokines, inflammatory cells, reactive oxygen species, and harmful agents primarily trigger cellular changes that cause esophagitis. Continuous exposure to these factors results in complete differentiation of the metaplasia cell type. When cells become atypical and grow abnormally within a tissue, they are defined as dysplastic cells. Dysplasia is classified as low-grade or high-grade based on the severity of abnormal cell growth. High-grade dysplasia carries a high risk if left untreated because it is the critical step before invasive carcinoma [21]. According to Vienna classification, which is an international hierarchical system to classify figurative elements of trademarks, the stages of esophageal adenocarcinoma depending on histopathological features are specified in five categories: non-dysplastic Barrett's Esophagus (NDBE), indefinite for dysplasia (IND), low-grade dysplasia (LGD), high-grade dysplasia (HGD) and esophageal adenocarcinoma (EAC) (Figure 5a). Figures 5b-5f show a schematic representation of these stages with emerging cytological abnormalities and architectural changes [18, 22, 23].

However, the mechanism of the formation of BE is still contradictory. Some clinicians have suggested that the replacement process begins with transforming the cardiac mucosa into columnar epithelium, the only mucosal type that causes intestinal metaplasia. As a result, the columnar epithelium and intestinalization gradually spread to the esophagus. On the other hand, other clinicians support that BE emerges rapidly in all its dimensions and then undergoes minor changes. Studies on these concerns have shown that increased acid exposure in association with the severity of GERD causes a significant increase in the length of the columnar mucosa. A follow-up study in children showed intestinalization of columnar epithelium in the esophagus over five years. However, another follow-up study of approximately seven years resulted in no significant change in BE length compared to the baseline in all age groups [10].



Stage	Histopathology features
NDBE	• Intestinalized columnar-lined epithelium • Normal cytology • Normal surface maturation (nuclear:cytoplasmic ratio of surface epithelium is lower than basal cells)
IND	• Normal architecture • Normal surface maturation • Mild cytological abnormalities
LGD	• Mild architectural changes • Surface maturation disrupted (stratification) • Mild, diffuse cytological abnormalities (such as enlarged, hyperchromatic nuclei, mitotic activity and normal cell polarity)
HGD	• Marked architectural changes • No surface maturation • Marked cytological abnormalities (such as enlarged nuclei, loss of cell polarity, mitotic activity and atypical mitoses)
EAC	• Marked architectural changes: carcinoma invades through basement membrane • No surface maturation • Marked cytological abnormalities (such as enlarged nuclei, loss of cell polarity, mitotic activity and atypical mitoses)

Figure 5: (a) Stages involved in progression from Barrett's esophagus to esophageal adenocarcinoma according to Vienna classification: NDBE (non-dysplastic Barrett's esophagus), IND (indefinite for dysplasia), LGD (low-grade dysplasia), HGD (high-grade dysplasia) and EAC (esophageal adenocarcinoma) with corresponding histopathology features [18]. **(b-f)** A schematic representation of these stages manifesting cytological irregularities and arising glandular architecture [23].

Risk factors for BE include demographic factors (i.e., being a white male), presence of GERD, lifestyle factors (e.g., smoking, alcohol consumption, obesity, diet), family history, and age. In addition, the size of a hiatal hernia is associated with BE. In contrast to the infectious effects on the stomach and duodenum, *Helicobacter pylori* is associated with a lower prevalence in Barrett's Esophagus. Nevertheless, GERD is a significant risk factor for BE. Chronic exposure to acid has been linked with cellular and molecular alterations in the esophagus [18, 24]. Meanwhile, reflux causes deformation in GEJ, which has anatomical importance as the border between the esophagus

and the stomach. Distortion of GEJ precludes a definitive diagnosis of BE. Therefore, in the 1980s, Skinner et al. suggested a columnar lining of at least 3 cm as a diagnostic criterion [14]; however, in the mid-1990s, the diagnostic criteria evolved as short and long segment BE for the IM shorter and more prolonged than 3 cm, respectively [25, 26].

Although BE is asymptomatic, its clinical appearance is associated with GERD and can be followed up with endoscopy. Three critical findings need to be recognized during endoscopy: 1) GEJ to identify the end of the esophagus; 2) diaphragmatic pinch to detect the presence of hiatal hernia, and 3) squamo-columnar junction to check if it overlaps with the GEJ. BE may be recommended if the squamo-columnar junction (SCJ) is at least 1 cm above the GEJ. The second diagnostic criterion is the histopathology of biopsy samples taken randomly from suspicious areas. Classical staining with hematoxylin and eosin (H&E) reveals goblet cells in IM required for accurate diagnosis.

Along with the diagnosis, the definition of Barrett's esophagus is vital in terms of treatment. To avoid interobserver variability, a systematic study was conducted by the International Working Group on Esophagitis Classification, which decided on the Prague C & M Criteria. In this classification, GEJ is considered the origin (0.0), then a circumferential segment of BE is denoted C with its corresponding length. The maximum length reached by the tongue is indicated as M [27]. Figure 6a shows a schematic representation of the Prague C & M classification, identifying a region of BE as C2M5. Figures 6b and 6c exemplify the definition via endoscopy images of a healthy esophagus with the adjacent GEJ and SCJ and BE with 5 cm circumferential extension and 6.5 cm maximal extension from the GEJ [28, 29].

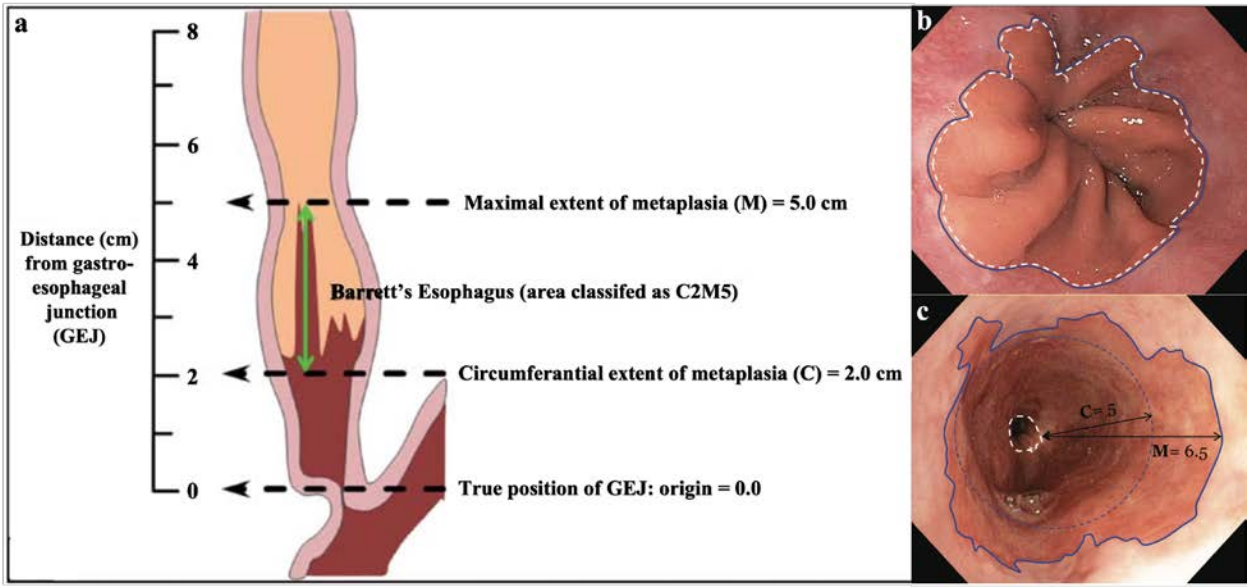


Figure 6: (a) A schematic representation of Prague C & M criteria that showing an area of Barrett's Esophagus (BE) defined as C2M5 [28]. **(b)** An exemplary endoscopy image showing GEJ at proximal limit of gastric folds (white dashed line), and SCJ (blue line), **(c)** an exemplary endoscopy image of long segment BE that SCJ becomes distant from GEJ; with a circumferential extent of C = 5 cm and a maximal extent of M = 6.5 cm [29].

Although conventional endoscopy imaging greatly aids in visualizing visible lesions, sensitivity may not be sufficient to recognize subtle changes in the mucosa. Therefore, various imaging procedures have been used to diagnose and screen BE. Commonly used optical techniques include [11, 18, 22, 30-33]:

White-Light Endoscopy: High-Definition upper gastrointestinal endoscopy is the preferred imaging modality as the gold standard. However, it is necessary to increase the resolution and contrast of white light endoscopy images to reduce missed rates compared to biopsy specimens.

Chromoendoscopy: A technique that requires topical application of a dye to enhance mucosal visualization by creating a contrast between normal and neoplastic mucosa. Lugol's iodine, which contains potassium and iodide absorbed by glycogen, is mainly preferred for the upper GI tract, although indigo carmine, methylene blue, and acetic acid are the primary dyes used. Lugol's iodine imparts a brownish color to normal squamous mucosa containing glycogen; this highlights Barrett's epithelium as white or yellowish due to the lack of glycogen in it.

Narrow Band Imaging (NBI): Using an optical filter that narrows the wavelength range of light to 400-430 nm (blue) and 525-555 nm (green), narrow-band imaging highlights vessels on the mucosal surface and vessels at different depths. Therefore, narrow-band imaging can be considered a virtual chromoendoscopy.

Flexible Spectral Imaging Color Enhancement: Alias Optical Band Imaging is another dyefree method to increase contrast. It is based on post-processing spectrum analysis software. Sixty spectral images taken at 5 nm intervals between 400 and 695 nm are digitally processed to combine appropriate wavelengths with specific conditions.

Blue Light Imaging: Similar to narrow-band imaging, the 410 nm laser helps to visualize the vascular microarchitecture at the mucosal surface, and the phosphor-tipped 450 nm laser helps to visualize larger blood vessels in the deeper layers.

Autofluorescence Imaging: Endogenous tissue fluorophores in the GI tract, such as collagen, elastin, and nicotinamide adenine dinucleotide hydride, are autofluorescent; exposure to the appropriate short wavelength results in the emission of longer wavelengths,

depending on the tissue type. The difference between the collagen and hemoglobin concentration in normal and abnormal (dysplastic to cancerous) tissue and the nuclear and cytoplasmic ratio alter the autofluorescence emission. For example, normal mucosa has a green reflection as a background, while dysplastic and neoplastic tissue appears magenta or purple.

Optical Coherence Tomography (OCT): This imaging method is based on obtaining crosssectional images at 1-2 mm depth by back-scattering the light transmitted to the tissue. OCT provides a high resolution of ~10 µm, reasonably close to histology level. Although it has a sensitivity of approximately 68% and a specificity of approximately 82%, it has not been used in clinical practice outside of research studies. Volumetric laser endomicroscopy, a new generation of OCT, provides helical peripheral scans with a laser (1350 nm) probe centered inside a transparent balloon. Large surface areas can be visualized with high resolution and speed with volumetric laser endomicroscopy.

Confocal Laser Endomicroscopy: This advanced technique requires significant operator expertise and provides subsurface analysis and in vivo histology during the endoscopy procedure with the visualization of cellular and microvascular structures at a higher spatial resolution up to 250 µm depth. With 98.1% sensitivity and 94.1% specificity, it provides high predictive rates for BE. Like OCT, confocal laser endomicroscopy is being evaluated by research studies.

Spectroscopy: This model relies on the scattering variation of full spectrum light due to tissue structure, vascularization, and size. Other advanced minimally invasive technologies:

Transnasal Endoscopy: As a procedure that does not require sedation, although the working channel is narrow, it provides a safe, efficient, cost-effective, tolerable, and rapid application compared to upper endoscopy.

Tethered Capsule Endomicroscopy / Esophageal Capsule Endoscopy: These techniques, which are non-invasive imaging methods, are designed to create 3D microscopic images without taking biopsy samples with optical frequency domain imaging technology in OCT.

Cytosponge™: Unlike Tethered Capsule Endomicroscopy / Esophageal Capsule Endomicroscopy, Cytosponge™ (Medtronic, Menneapolis, MN, United States) is a nonendoscopic cytological technique used to collect cells from the esophageal mucosa for histopathological analysis without providing images. It is a bound, compressed sponge combined with a biomarker test for trefoil factor 3 (TFF3), a cell marker for intestinal metaplasia.

Biomarker Panels: Although a single and ideal biomarker for Barrett's esophagus has not yet been identified, expression of the tumor suppressor gene - p53 - can be considered as a biomarker. Inactivation of this gene indicates the risk of progression of BE to dysplasia and EAC.

Breath testing: Electronic nose devices have been used to detect subtle differences in volatile organic compounds from breath. These devices convert chemical incomes to electrical outcomes that can be combined with machine-learning programs.

Wide area transepithelial sampling with 3-dimensional tissue analysis: An abrasive scrubbing tool is used to obtain transepithelial samples of BE for analysis by a high-speed computer system to detect suspicious cells.

1.2. Current Treatment Approaches

Treatment strategies for Barrett's Esophagus seek three primary outcomes: 1) cessation of reflux, 2) initiation of healing or regression of IM, and 3) suppression of progression to dysplasia [10]. Current approaches for these purposes can be grouped into three main groups: drug therapy, endoscopic interventions, and surgery (Figure 7). Combining these techniques can achieve the intended eradication results [17, 34].



Figure 7: Current treatment strategies of Barrett's Esophagus can be divided into three main groups: medication, endoscopic therapies, and surgery (images retrieved from references [35-37]).

1.2.1. Medicine

First, rehabilitation on lifestyle factors such as smoking, obesity, diet, and GERD probably has a more significant impact than chemoprevention. However, most patients with non-dysplastic BE begin treatment medically. Drug therapy focuses on reducing reflux symptoms, using proton pump inhibitors and histamine-2 receptor antagonists to suppress acid production [10]. It is aimed to provide relief by reducing the erosive effect while keeping the stomach pH above 4. In addition, non-steroidal anti-inflammatory drugs, including aspirin, are associated with a reduced risk of esophageal cancer due to their inhibitory effects on cyclooxygenase 2, which is involved in tumor invasiveness and angiogenesis. Also, statins are another alternative for drug therapy because of their anti-angiogenic, anti-proliferative, pro-apoptotic, and immunomodulatory effects that reduce cancer risk [22, 24, 28, 33].

While it is commonly assumed that acid suppression inhibits the progression of Barrett's Esophagus, clinical data has not confirmed it.

1.2.2. Endoscopic Interventions

Endoscopic management of Barrett's Esophagus includes non-ablative and ablative strategies, considering stages from indeterminate dysplasia to high-grade dysplasia and mucosal esophageal adenocarcinoma. Both are based on eliminating metaplastic or dysplastic mucosal tissue.

Non-ablative methods, referred as tissue acquiring techniques, endoscopic mucosal resection and endoscopic submucosal dissection are the preferred approaches in treating dysplasia and superficial esophageal adenocarcinoma. Figures 8 and 9 summarize techniques for treating BE. In endoscopic mucosal resection (EMR), the lesion is aspirated into an endoscopic cap (Figures 8a – 8g) or a band ligator (Figures 8h – 8l) before elimination. Endoscopic mucosal resection is appropriate for lesions smaller than 2 cm in diameter. In contrast, endoscopic submucosal dissection (ESD) can perform en-bloc resection of lesions larger than 2 cm in diameter (Figures 9a – 9f). Some endoscopic mucosal resection techniques and endoscopic submucosal dissection require a submucosal injection to lift the tissue. In endoscopic mucosal resection, resection is performed with a snare, whereas in endoscopic submucosal dissection, incision and tissue dissection are performed using a standard needle blade and insulated-tip (IT) knife. These approaches allow larger tissue samples than conventional biopsy for histopathological studies. Because both techniques require detailed application protocols, becoming an expert or receiving specific training from a qualified endoscopist before interventions is essential [18, 22, 24, 33, 38, 39].

Ablative methods that rely primarily on energizing the target tissue to induce a thermal or photochemical effect include multipolar electrocoagulation, argon plasma coagulation, laser (photothermal) ablation, photodynamic therapy, radiofrequency ablation, and cryoablation [18, 30, 33].

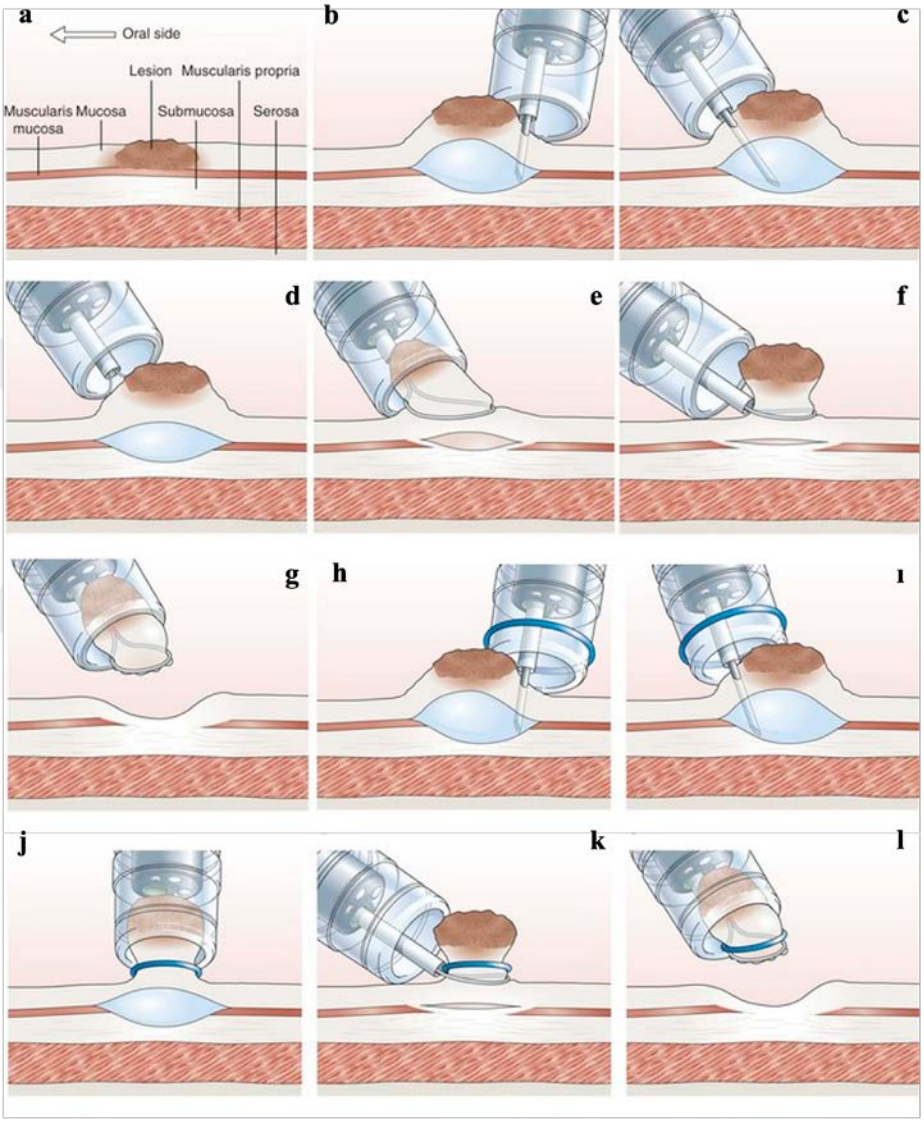


Figure 8: A schematic representation of endoscopic mucosal resection technique by using an endoscopic cap **(a – g)** and a band-ligator **(h – l)** [40].

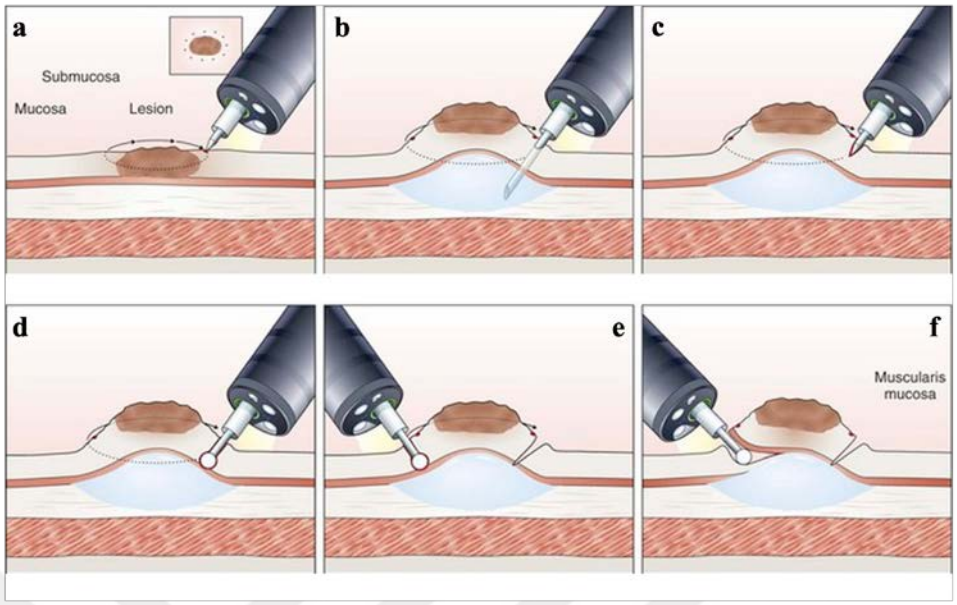


Figure 9: A schematic representation of endoscopic submucosal dissection technique **(a – f)** [40].

Multipolar electrocoagulation is a technique in which electrodes deliver an electrical current of approximately 15 to 50 W to tissue through direct contact. Acid suppression is performed before ablation. The duration of the electrical current implementation is coupled with the appearance of a white coagulum. The energy setting, duration, and pressure applied to the tissue affect the ablation depth achieved with multipolar electrocoagulation. Energy is usually delivered through 10F size (3.3 mm) electrical probes through the working channels of the endoscopes. Ablation can be performed from the probe's tip or side-firing; even tangential application is possible [33, 41-43].

In contrast, in argon plasma coagulation (APC), the high-frequency monopolar current is transmitted through ionized argon gas (argon plasma) without direct contact with tissue. The plasma flow setting, power setting, application time, and distance between the probe and the target lesion define the depth and degree of tissue coagulation. Argon plasma coagulation probes can be inserted through the endoscope's working channel, but it is essential to have a gap of at least 10 mm between the tip of the endoscope to protect the video chip. The distance to the tissue is recommended to be between 2-8 mm. For BE application, it is recommended that the single point application time should not be too long (>2 sec) at a power of 30-50 W in pulsed mode at a rate of 1-2 lt/min [39, 44].

Laser (photothermal) ablation relies on thermally injuring the target lesion by converting the absorbed laser energy into heat to a certain depth. Lasers used in BE treatment include the 488 nm – 514 nm argon laser, the 1064 nm and 1320 nm neodymium yttrium aluminum garnet (Nd:YAG) lasers, the 532 nm potassium titanyl phosphate (KTP) (i.e., the second harmonic of the Nd:YAG

laser), and the 805 nm and 940 nm diode lasers. Laser energy can be applied in free-space mode using a bare fiber or in contact mode using a sapphire tip and can vary for different laser wavelengths [45-50].

In photodynamic therapy (PDT), a photosensitizer (e.g., porfimer sodium, δ-aminolevulinic acid) that is selectively absorbed by specific cells with a high metabolic rate in the body (e.g., neoplastic cells) is activated by low-energy laser light of the appropriate wavelength to generate free oxygen radicals for cellular destruction. Photodynamic therapy requires intravenous injection of the solution and 48 hours of waiting time before exposure to light. In a study, it was shown that combining photodynamic therapy with argon plasma coagulation therapy resulted in more effective removal of Barrett's epithelium than photodynamic therapy alone [30, 39, 51].

Cryoablation is a non-contact, repetitive procedure involving low-pressure liquid nitrogen spraying at -196 °C or compressed carbon dioxide at -78 °C onto a tissue for rapid freezing followed by slow thawing until the tissue is thermally damaged. Cryoablation requires a unique protective decompression tube to prevent perforation, possibly caused by barotrauma. The catheter tip can be placed 5-10 mm from the tissue. The ablation dose is related to exposure time, but no standardization exists. Tissue whitening due to thermal damage defines the ablation time, typically 10 seconds. Due to the relative resistance of collagen and fibrin proteins to freezing, it can allow selective necrosis of cellular components while preserving the extracellular matrix. Thus, it causes less inflammation and fibrosis compared to other ablative techniques. In addition, the non-contact spraying feature of cryoablation enables rough, large areas to be affected and allows application in patients with luminal irregularities [39, 44, 51, 52].

Radiofrequency ablation (RFA) uses high-frequency energy transmission through a catheter to cause necrosis in unwanted tissue. After preliminary exploration with sizing catheters, the RF energy generator connected to the ablation catheter is placed in a suitable position to deliver approximately 12-15 J/cm of energy. With the contribution of BARRX Medical HALO systems, RFA is preferred more frequently than other ablation techniques. These devices contain a series of electrodes separated by micrometers. The focal devices – Barrx Channel, Barrx 60, Barrx 90, and Barrx Ultralong – were designed for smaller tongues, while a balloon-based Barrx 360 was designed for more extensive or circumferential BE segments (Figure 10a). However, focal catheters were mainly preferred because of their maneuverability and allowing endoscopic imaging even in circumferential ablation In that case, multiple therapy sessions are required to complete ablation [22, 33, 39, 44, 51, 52]. Figures 10b and 10c depict the schematic representation of RFA application to the distal esophagus, while Figure 11 shows actual endoscopic views of BE before and after RFA

treatment using Barrx 360 and Barrx 90 catheters. Extensive area BE lesions are candidates for circumferential therapy for their maximum length as defined by the Prague C&M criteria, although the lesion is not uniform over its entire length. Before the ablation procedure, the endoscope and sizing catheter are inserted multiple times into the esophagus to determine BE position and inflated balloon size.

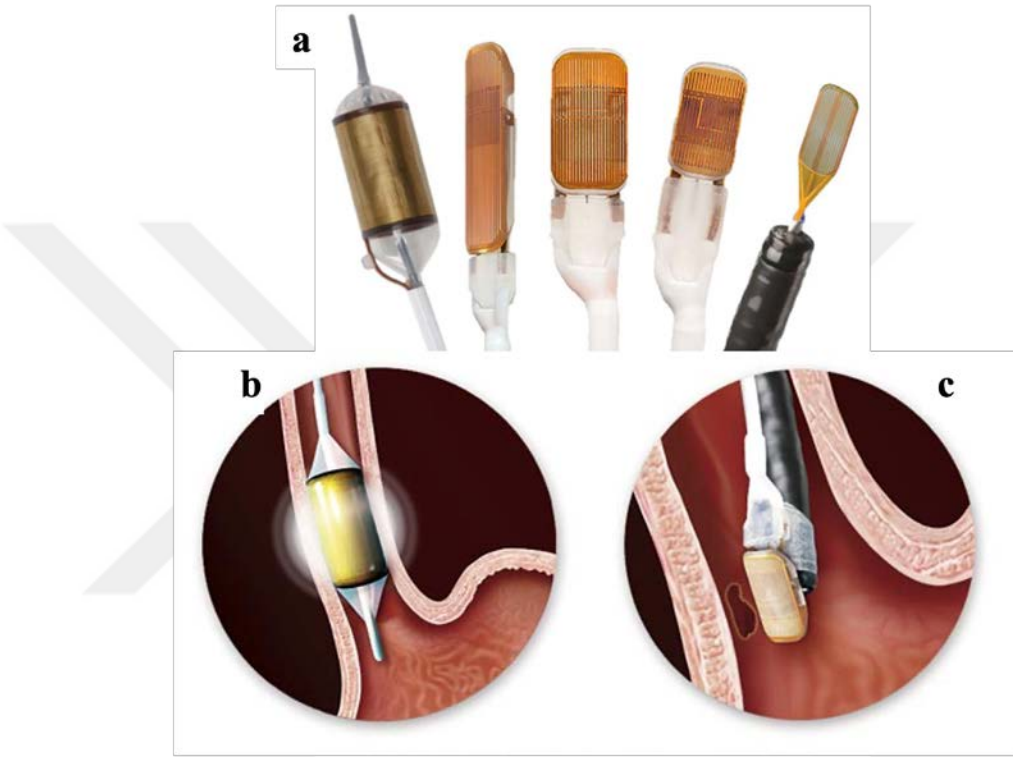


Figure 10: (a) The radiofrequency ablation catheter family including: Barrx 360 (self-sizing up to 4 cm); Barrx Ultralong (40 mm x 13 mm); Barrx 90 (20 mm x 13 mm); Barrx 60 (15 mm x 10 mm); Barrx Channel (15.7 mm x 7.5 mm), from left to right [53]. **(b, c)** The schematic representation of the use of circumferential and focal catheters for the lesions in distal esophagus [54].

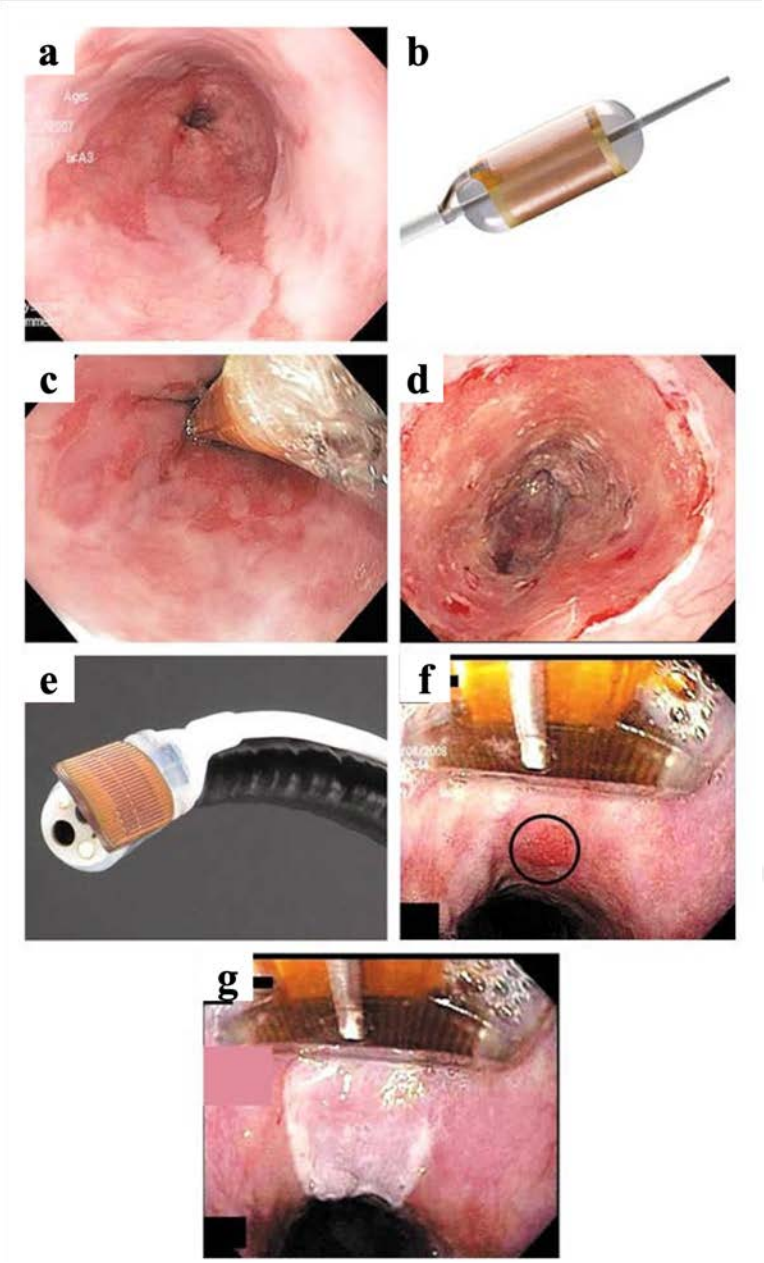


Figure 11: Radiofrequency ablation (RFA) of Barrett's esophagus (BE). **(a)** An endoscopic image of distal esophagus in a patient having BE. Salmon colored tongues protruded from gastroesophageal junction into pale mucosa of normal stratified squamous epithelium. **(b)** A photograph of inflated Barrx 360 catheter having bipolar array for circumferential ablation. **(c)** An endoscopic image of deflated Barrx 360 catheter positioned in the segment of esophagus where BE lesion appears. **(d)** An endoscopic image of the distal esophagus after RFA by using Barrx 360 catheter. The circumferential ablation removed both BE lesion and surrounding healthy tissue without distinction. **(e)** A photograph of Barrx 90 united to tip of endoscope. **(f, g)** The endoscopic images of small BE island (black circle) before and after focal treatment with Barrx 90 catheter respectively. The effect of RFA on tissue manifests itself as white coagulum [55].

Figure 11a shows an endoscopic view of the distal esophagus of a patient diagnosed with BE. The Barrx 360 (Figure 11b) is positioned towards the Barrett's Esophagus lesion (Figure 11c) and then inflated and brought into contact with the mucosa layer that obstructs the view of the

endoscope. With RFA, the BE lesion and surrounding healthy mucosal tissue were excised circumferentially, and local bleeding points were observed along the ablation site (Figure 11d). Barrx 90 (Figure 11e) is suitable for focal and short BE islands. This catheter can be placed on the tip of an endoscope. The black circled BE island in Figure 11f is ablated until a white coagulum is visible on the mucosal surface. Similarly, the normal stratified squamous epithelium surrounding the island of BE is affected by thermal damage during the ablation procedure and visualization of the lesion is blocked by catheter.

These devices using RFA have been evaluated in several studies, summarized in the two tables shown in Table 1 and Table 2 [56]. The effectiveness, recurrence, and complication rates of the RFA technique in different stages of BE were investigated.

Histological assessments have demonstrated that ablation studies support the replacement of BE with squamous epithelium in a reflux-free setting. The newly formed epithelium is called the neosquamous epithelium. The type of therapy determines the degree of squamous regeneration. Although the similarity between neosquamous epithelium and healthy esophageal epithelium has been suggested as an anecdotal experience considering its structural and cellular similarity, the pathological features of neosquamous epithelium have not been systematically studied. Thus, the origin of newly developed squamous cells has been debated. However, this re-epithelialization could potentially inhibit the progression of esophageal adenocarcinoma. It should also be noted that incomplete eradication may result in the burial of Barrett's metaplasia under the neosquamous epithelium [46, 47, 49, 57-59].

1: RFA efficacy for BE with LGD and IM [56].

Author (et al.)	Study Design	Setting	Number	BE length in cm	ER before RFA (%)	Efficacy (end of treatment)		Recurrence		Complications
						CE-D (%)	CE-IM (%)	D (%)	IM (%)	
Sharma	RS	SC	10	4.4 (mean)	0%	90%	90%	0%	0%	10% (1 bleeding)
Sharma	PS	SC	38	4 (median)	0%	95%×	87%×	NR	NR	2.6% (1 stricture)
Shaheen	RCT	MC	42	4.6 (mean)	NR	90.50%	81%	–	–	9.5% (5 stricture, 1 bleeding, 2 chest pain)
Pouw	PS	MC	11	8 (median)	96%	91%	91%	0%	0%	8% (1 bleeding, 1 stricture)*
Lyday	RS	MC	13	3 (median)	0%	100%×	85%	NR	NR	3.9% (9 stricture, 3 bradycardia, 4 bleeding, 1 superficial mucosal injury, 1 fever)*
Shaheen	RCT	MC	52	4.5 (mean)	9%	98%	98%	2%	2%	10.9% (1 bleeding, 3 chest pain, 9 esophageal stricture)*
Okoro	RS	SC	13	4.5 (mean)	0%	61.5%×	61.5%×	NR	NR	16.6% (10 stricture, 5 chest pain)*
Bulsiewicz	RS	SC	44	4 (mean)	9%	93%	86%	NR	NR	8.2% (18 stricture, 2 bleeding)*
Dulai	RS	SC	ULSBE:5	10.8 (median)	38%*	100%	77%*	0%	23%*	21% (7% postablative mucosal tears and 14% stricture)
			LSBE:7	4.7 (median)	24%*	100%	82%*	0%	16%*	
Phoa	RCT	MC	68	4 (mean)	–	92.60%	88.20%	1.60%	10%	19.1% (8 stricture, 3 mucosal laceration)
Small	RS	MC	45	5 (median)	4.40%	95.60%	77.80%	16%	NR	–

ive data.

ett's Esophagus; ER: endoscopic mucosal resection; RFA: radiofrequency ablation; RCT: randomized controlled trial; PS: prospective study; RS: retrospective study; SC: single center; MC: multicenter; ULSBE: ultra-long Barrett's Esophagus, NR: not reported; CE-D: complete eradication of dysplasia; CE-IM: complete eradication of intestinal metaplasia; D: dysplasia; IM: intestinal metaplasia. × : efficacy at end of follow up.

giano C, Iabichino G, Eusebi LH, Arena M, *et al.* Outcomes of radiofrequency ablation for dysplastic barrett's esophagus: A comprehensive review. Gastroenterol Res Pract 2016: 4249510, 2016.

RFA efficacy for BE with HGD and intramucosal carcinoma [56].

Author (et al.)	Study Design	Setting	Number	BE length in cm	ER before RFA (%)	Efficacy (end of treatment)		Recurrence		Complications
						CE-D (%)	CE-IM (%)	D (%)	IM (%)	
Gondrie	PS	SC	11	7 (median)	58%	91%	100%	0%	0%	9% (1 stricture)
Gondrie	PS	SC	9	5 (median)	55%	88.90%	100%	NR	0%	0%
Ganz	RS	MC	142	6 (median)	17%	80.4%×	54.3%×	NR	0%	0.4% (1 stricture)
Sharma	PS	SC	24	6 (median)	8%	79%×	67%×	NR	NR	0%
Shaheen	RCT	MC	42	5.3 (mean)	NR	81%	74%	–	–	9.5% (5 stricture, 1 bleeding, 2 chest pain)*
Pouw	PS	MC	24	8 (median)	96%	95%	88%	0%	12.50%	8% (1 bleeding, 1 stricture)*
Van Vilsteren	RCT	MC	22	4 (median)	82%	96%	96%	0%	0%	31.8% (3 bleeding, 3 stenosis, 1 acute nontransmural laceration)
Lyday	RS	MC	10	3 (median)	10%	100%×	80%×	NR	NR	3.9% (9 stricture, 3 bradycardia, 4 bleeding, 1 superficial mucosal injury, 1 fever)*
Shaheen	RCT	MC	54	5.2 (mean)	8%	92.60%	89%	7.40%	11%	10.9% (1 bleeding, 3 chest pain, 9 esophageal stricture)*
Okoro	RS	SC	39(ER+RFA) 8(RFA)	6.9 (mean) 4.5 (mean)	100% 0%	74.4%× 87.5%×	41%× 87.5×	NR	NR	16.6% (10 stricture, 5 chest pain)*
Bulsiewicz	RS	SC	166	4 (mean)	39.20%	84.90%	78.30%	NR	NR	8.2% (18(stricture, 2 bleeding)
Dulia	RS	SC	ULSBE:25 LSBE:26	10.8(median) 4.7(median)	38%* 24%*	88% 84%	77%* 82%*	0% 0%	23% 16%	21% (7% postablative mucosal tears, 14% stricture)*
Haidry	RS	MC	335	5.8 (median)	49%	81%	62%	6%	9%	9.3% (30 stricture, 1 perforation)
Strauss	RS	MC	36	3.5 (mean)	86%	89%	75%	9%	27%	22% (7 stricture, 1 bleeding)
Perry	RS	SC	17	5 (median)	53%	88%	65%	17.6%	46%	0%
Lada	RS	SC	57	5.1 (mean)	49%	79%	49%	21%	7.60%	3.8% (2 stricture, 2 chest pain)
La Page	RS	SC	36	5 (median)	47.80%	97%	61%	6%	NR	16% (6 chest pain, 1 stricture, 1 bleeding)

data.

's Esophagus; ER: endoscopic mucosal resection; RFA: radiofrequency ablation; RCT: randomized controlled trial; PS: prospective study; RS: retrospective study; SC: single center; MC: multicenter; ULSBE: ultra-long segment ophagus, NR: not reported; CE-D: complete eradication of dysplasia; CE-IM: complete eradication of intestinal metaplasia; D: dysplasia; IM: intestinal metaplasia. × : efficacy at end of follow up.

ano C, Iabichino G, Eusebi LH, Arena M, *et al*. Outcomes of radiofrequency ablation for dysplastic barrett's esophagus: A comprehensive review. Gastroenterol Res Pract 2016: 4249510, 2016.

1.2.3. Surgery

It can be thought that surgical treatment approaches to removing Barrett's epithelium alleviate GERD symptoms and prevent cancerous tissue progression. Anti-reflux surgery is an effective and permanent solution to prevent permanent damage to the esophageal mucosa in patients who have problems with long-term high-dose acid suppression therapy or who complain of recurrence of symptoms after drug discontinuation [10].

Although esophagectomy was formerly the primary option for patients with high-grade dysplasia and esophageal adenocarcinoma, advances in endoscopic resection and ablation techniques offer alternative treatments, particularly for BE with focal dysplastic mucosa and early adenocarcinoma. However, removing the lesion is required to treat BE with multifocal high-grade dysplasia. In addition, esophagectomy can eliminate occult carcinomas [22, 33, 34].

1.3. Limitations of Current Treatment Approaches

The availability of various treatment strategies indicates both advances in BE therapies and the ineffectiveness of current treatments. Due to the lack of randomized, head-to-head comparative studies, selecting available techniques is mainly empirical and primarily dependent on patient characteristics, institution availability, and user preference. Therefore, the results may also depend on the experience level of the endoscopist.

Given the ideal treatment prospects - cessation of reflux, onset of healing or regression of intestinal metaplasia, suppression of progression to dysplasia - the drug only offers a solution for cessation of reflux, while other requirements are not reliably met. Like medication, anti-reflux surgery has not effectively prevented BE from progressing to dysplasia and, ultimately, cancer, but it has more control over reflux. Esophagectomy, another surgical treatment technique, is the primary choice before the developments in endoscopic intervention techniques. However, it is mainly associated with post-surgical morbidity and mortality. Besides, long-term surveillance of BE progression to qualify for esophagectomy is time-consuming and costly. [60].

As non-ablative methods, endoscopic mucosal resection and endoscopic submucosal dissection have an advantage over ablative strategies by retrieving tissue for histopathological analysis. However, they are complex procedures that must be performed by experienced endoscopists and are associated with significant complication rates due to short-term side effects

such as bleeding or perforation. In addition, stricture formation is the most common complication in approximately 40-50% of patients after circumferential resection procedures.

Although ablative modalities provide reliable treatment, the main disadvantage is the destruction of pathological specimens that could potentially be used for histological examination. One of the foremost ablation techniques used for BE treatment is multipolar electrocoagulation. The fact that multipolar electrocoagulation is simple without needing any agent, or a particular catheter has made it more accessible and familiar than other ablation techniques. However, the need for tissue contact with a relatively small size probe prolongs the processing time, especially for large areas. In addition, the operating settings and pressure applied during tissue contact affect the ablation depth, resulting in inconsistent energy distribution. Although few studies have shown a reversal of Barrett's epithelium after multipolar electrocoagulation therapy, it has yielded modest results against side effects such as odynophagia, dysphagia, and chest pain. Therefore, multipolar electrocoagulation is not preferred today [42, 43].

Besides multipolar electrocoagulation, argon plasma coagulation is one of the earliest ablation techniques used in BE treatment. However, the point-and-shoot nature increases operator dependency, and the number of treatment sessions to achieve complete eradication makes it potentially dangerous. Besides, placing the argon plasma coagulation probe is challenging; It should be neither too close nor too far from the tissue surface. Theoretically, the electrical conductivity of the tissue decreases due to drying as the result of increased temperature. For this reason, it is expected that the progress of the electric current toward the deep layers of the tissue will slow down or even stop. However, unexpected occurrence of complete necrosis or even tissue perforation caused death. In a pilot study, argon plasma coagulation applied after saline injection reduces side effects but prolongs the treatment process and administration time [18, 30].

As another alternative, lasers have started to be preferred in medical applications. Despite the reputation earned in hemostasis studies, lasers have not been used on a larger scale in BE. The cost and sophisticated use of lasers and the need for a fixed room limit the number of randomized trials evaluating the effectiveness of laser ablation. Although diode lasers have gained the advantage of being compact and portable, proper delivery of laser energy to target tissue is still challenging, causing under- or over-treatment, and the laser wavelengths available are limited. Other complications associated with laser ablation are bleeding, perforation, and stenosis [45, 48, 57, 61].

On the other hand, significant post-treatment disadvantages of photodynamic therapy are prolonged photosensitivity and esophageal strictures. In addition, the cost of the photosensitizer and the 2-day waiting time are critical limitations of the intervention. Although photodynamic

therapy reduces progression to malignancy, as does photosensitivity, buried metaplasia has been reported in one-third of patients receiving therapy. Therefore, ablative methods with less risk of procedural complications than photodynamic therapy were preferred [22, 33, 51].

Among the ablation modalities, cryoablation is considered the safest, most efficient, and most durable technique due to its low rate of stricture formation and less discomfort after the procedure. While causing thermal injury, its cold-based character ensures the preservation of tissue architecture. In addition, the cooling effect may tend to induce an anesthetic response. Although it has advantages over other ablation methods, the main disadvantages of cryoablation are distention, dysphagia, and chest pain. However, sufficient data are required for further studies and further evaluation of safety and efficacy [22, 51, 52].

RFA is the most used ablation technique compared to others due to its high histological complete response rate, safety profile, affordability and good tolerability, and availability of delivery catheters. Although the procedure time is between 20-50 minutes, more than one placement of the RFA device and endoscope imaging and repeated treatment sessions, depending on the BE segment length, are required to achieve the desired result. Commonly reported complications of RFA include chest pain, stricture formation, gastrointestinal bleeding, and perforation [18, 33, 51, 55].

A review study summarizes adverse effects after using standard ablation techniques and their incidence rates (Table 3). It is generally difficult to completely eradicate Barrett's Esophagus using a single ablation method. The stage of Barrett's Esophagus - Non-Dysplastic Barrett's Esophagus, Low-Grade Dysplasia, High-Grade Dysplasia - and its extent across the esophageal surface are essential for choosing the optimal approach. Therefore, many patients were subjected to hybrid treatment strategies, potentially combining EMR and RFA even with a proton pump inhibitor. Also, many ablation techniques require multiple therapy sessions to achieve a complete cure. Specifically for peripheral and significant BE lesions, most ablation methods are insufficient to control the depth of injury fully. In addition, when all of them are applied to extensive areas, they show high stenosis formation.

Table 3: Adverse effects of standard ablation techniques with incidence rates [51].

	Common adverse effects	**Uncommon adverse effects**
Radiofrequency ablation	Pain (3-9%), dysphagia (3-9%), stricture (5-12%)	Gastrointestinal bleeding
Photodynamic therapy	Strictures (20-37%), photosensitivity (10-69%)	Arrhythmias, pleural effusion

Cryoablation	Chest pain (14-25%), dysphagia (13-19%), odynophagia (12%), sore throat (10%)	Gastrointestinal perforation, abdominal pain

From Kallam A, Alsop BR, Sharma P. Limitations of endoscopic ablation in barrett's esophagus. Expert Rev Gastroenterol Hepatol 9: 487-96, 2015.

In particular, the incidence of specific complications is associated with other pre-existing health conditions of patients with BE. Anticoagulant therapy, prior radiotherapy therapy, and persistent reflux esophagitis are associated with an increased risk of bleeding, poor healing and increased risk of strictures, and poor response to BE treatment, respectively [39].

Overall, the limitations of current treatment strategies can be summarized as follows;

- use of hand-held, hand-aimed devices to arrange position and dose of treatment,
- short term adverse events like bleeding, perforation, stricture formation, chest pain, and nausea,
- post-ablation residual/buried Barrett’s metaplasia/glands,
- necessity of multiple therapy sessions, - recurrence.

1.4. Laser-Induced Thermal Therapy

The interaction between laser and tissue can be grouped into three parts: optical, thermal, and biological. The optical part includes reflection, absorption, scattering, and transmission of photons. Absorption and scattering are critical and interdependent mechanisms that determine the distribution of laser light energy in a tissue area. The combination of laser wavelength and a chromophore (i.e., absorber) causes vibrational changes, called absorption, in molecules that receive some energy from the light. Different molecules have separate threshold energy levels; for example, most organic molecules absorb UV light, melanin and hemoglobin absorb visible light, while water is the primary chromophore in soft tissue for the mid and far infrared. On the contrary, tissues slightly absorb red and near-infrared; therefore, laser beams have high penetration only limited by scattering. Thus, different laser wavelengths lead to various tissue effects related to absorption events. The absorbed light energy is converted into heat, and the scattering defines the distribution of the absorbed light. As a result, light serves as the primary heat source where it is absorbed.

In the thermal step, heat transfer from the primary source is achieved by conduction. Both optical and thermal properties differ the primary and the secondary heat sources. Then, the biological step defines the tissue's response to heat. The amount and duration of heat alter the responses of the tissue. Changes include hyperthermia, coagulation necrosis, and evaporation as a

function of temperature rise. Hyperthermia occurs when the tissue temperature is above 40°C. However, it alters cell membrane permeability but does not produce an immediate gross or histological effect. Coagulation necrosis usually begins after 60 °C and leads to loss of membrane and metabolic function of cell, and denaturation of proteins. In addition, hemoglobin oxidation occurs at 80°C, causing vasoconstriction and collagen denaturation. After 100 °C, water evaporation begins causing tissue ablation, followed by charring, carbonization, and smoking along with rising temperature [45, 62-64]. Tissue modulation capability forms the basis of laser-induced thermal treatments.

Lasers used for medical purposes include excimer lasers, metal vapor lasers, dye lasers, and most commonly, argon lasers, CO_2 lasers, and Nd:YAG lasers. The development of flexible laser waveguides, such as optical fibers, led to using lasers in medicine, particularly in endoscopic interventions, in the mid-1970s. Argon, Nd:YAG and KTP:YAG lasers have been preferred in gastrointestinal system trials, especially in the treatment of BE, due to their widespread availability, endoscopic compatibility, and ability to test many conditions such as acute upper gastrointestinal bleeding, arteriovenous malformations (angiodysplasia), adenomatous colon polyps, and palliation of gastrointestinal cancer. However, the use of CO2 was limited by the lack of a viable tool. On the other hand, diode lasers have been recently used in various BE studies [62-64].

The wavelength of an argon laser is between 488 and 514 nm (the blue-green part of the electromagnetic spectrum), which is highly absorbed by red chromophores such as hemoglobin. Therefore, it only causes a superficial thermal effect of about 1 mm in soft tissues. Conversely, Nd:YAG operates at 1064 nm in the near-infrared, which is poorly absorbed and highly penetrating soft tissues, causing thermal injury at a 3 to 6 mm depth. KTP:YAG, a frequency doubled (second harmonic) Nd:YAG (1064 nm) laser, resulting in relatively shallower penetration. Diode lasers developed at 805 and 940 nm cause thermal damage above 1 mm. Therefore, the thermal damage depths produced can be compared using these lasers; argon < KTP:YAG << 940 nm diode < 805 nm diode < Nd:YAG [49, 50, 65, 66].

Table 4 lists the laser ablation trials chronologically for different stages of BE with their histology results. The first use of lasers in gastroenterology was in 1977 for hemostasis by coagulation of acute/chronic hemorrhages [67]. Studies on the effect of laser on hemostasis continued in the 1990s. Meanwhile, in a report by Fleischer and Kessler 1983, the palliative effect of laser ablation (photoablation) in esophageal cancer was confirmed for the first time by considering improvements in 14 patients with unresectable lesions [68]. Similarly, in cases where surgical treatment was no longer possible, photoablation therapy was preferred to relieve pain and

reduce congestion but not for cure. However, this endoscopic approach provides local laser therapy, eliminating necessity for general anesthesia and potential risks. In addition, visual inspection with the endoscope aids in the precise localization of laser therapy toward abnormal tissue. Also, laser therapy does not have a cumulative dosage effect, unlike radiotherapy, which must be limited. Thus, it can be repeated until the desired effect is achieved [62, 63, 67]. The power of the laser (Nd:YAG) to destroy columnar mucosa in BE with a suitable reflux-free medium was suggested by medical doctors Brant and Kauvar in 1992 with a case study report; however, in this report, the elimination of BE was temporary [69]. Subsequently, the first study demonstrating the ability of a laser (argon) to destroy BE was published by Berenson in 1993 [70]. Nevertheless, laser ablation has not been widely accepted as a strategy for treating BE due to the lack of long-term results. In 1996, Dix published a study to compare the thermal damage effect of Nd:YAG laser (1064 nm), KTP laser (532 nm), and diode laser (805 nm) on fresh samples from the human esophagus [71]. This study treated ex vivo tissue samples separately with lasers using different power and time settings. The study suggested that the KTP laser is the most suitable option for BE. In 2011 Polese and colleagues conducted a study on patients with BE using a diode laser at 940 nm with promising results [50].

Table 4: Laser ablation trials for different stages of BE with their histology results.

					Results		
Year	**Author**	**Patient(s), n**	**Histology (n)**	**Type of Laser**	**Histology**	**Buried BE**	**Ref.**
1992	Brandt	1	BE (1)	Nd:YAG free beam	Squamous 1/1	no	[69]
1993	Berenson	10	BE (8) LGD (2)	Argon Free beam	Squamous 38/40 (target areas)	_	[70]
1993	Sampliner	1	BE (1)	Nd:YAG contact/free beam	Squamous 1/1	_	[41]
1995	Ertan	1	Cancer	Nd:YAG	LGD 1/1	_	[72]
1996	Luman	4	BE (4)	Nd:YAG	0/4	_	[73]
1997	Barham	16	BE (16)	KTP:YAG free beam	Squamous 13/16	11/16	[46]
1998	Biddleston	10	BE (10)	KTP:YAG free beam	Squamous 9/10	8/10	[74]
1998	Salo	11	BE (11)	Nd:YAG contact	Squamous 11/11	0/11	[47]

1999	Gossner	10	LGD (4) HGD (4) Cancer (2)	KTP:YAG free beam	Squamous 4/4 Squamous 4/4 Squamous 2/2	1/4 1/4 0/2	[75]
1999	Sharma	6	Cancer	Nd:YAG free beam	Squamous 2/6 BE 2/6 LGD 1/6 T2N1 1/6	–	[76]
2000	Sharma	8	HGD	Nd:YAG free beam	Squamous 4/8 LGD 3/8 HGD 1/8	–	[77]
2002	Weston	14	HGD (11) Cancer (3)	Nd:YAG contact	Squamous 10/11 LGD 1/11 Squamous 1/3 BE 2/3	–	[78]
2011	Polese	20	BE (16) LGD (4)	940 nm Diode free beam	Squamous 9/16 Squamous 7/16 (incomplete) Squamous 4/4	no	[50]

Besides the advantages of lasers, they also introduce some challenges in practical use. The high cost and advanced technical requirements of commercially available lasers hinder endoscopic ablation therapy's widespread and frequent use. Lasers for gastrointestinal diseases can be used by other specialists and subspecialists, such as urologists and bronchoscopists, making lasers less financially burdensome. However, the necessity of a fixed operating room, such as an endoscopy room, has prevented the widespread use of lasers in other clinical settings. Lasers must be powered by conventional electricity and carry independent cooling systems to run such a cumbersome operating system. In addition, technical readjustment and calibration requirements should be minimal when transporting the laser to bedside, radiology, and intensive care units. Apart from these, some problems are encountered in applying the laser to the lesion area. The first applications of lasers were with bare fiber via the free-space mode. However, keeping up with esophageal motility, heartbeat, lumen curvature, and other external factors that changed the relative positions of the laser fiber tip and target lesion was difficult. In addition, the heat was a potential stimulus for secondary contraction of the esophagus, making the procedure more complex and timeconsuming. In addition, the bare fiber end tended to deteriorate from operation to operation, so it had to be maintained by cutting and sometimes polishing. With the development of sapphire contact tips, this difficulty has been overcome. Another development was the development of lateral spreading probes to facilitate access to lesions. However, the limited number of studies (Table 4) and the lack of randomized control studies for prospective comparison with other endoscopic modalities rendered the use of laser temporary. Indeed, laser ablation was not viable regarding the economic impact of BE compared to the available options. In addition, although experts under optimal conditions have made some successful attempts, the inability to transfer these studies to daily practice is due to the lack of coordination to establish a standard protocol for laser

treatments in multicenter studies and to perform this with a sufficient number of patients. Therefore, no data were available on the daily use of laser therapy worldwide. Also, unpublished laser trials are a bottleneck for evaluating laser treatments [45, 49, 62, 67, 79].

Considering all these pros and cons, initial enthusiasm for laser use in gastrointestinal endoscopic treatments is waning due to the lack of optimal devices and instruments that are affordable, small, portable, and versatile. Laser therapy for BE has been tried briefly with available resources, mainly suitable for other clinical situations. Despite promising results, the intended results have not been consistently achieved. Today advances in diode laser technologies, optical components, and optical imaging make it possible to use much more wavelengths that allow for case-specific approaches. These developments could potentially deliver laser energy to the target area more safely and effectively with new probe designs.

1.5. Aim and Hypothesis of the Study

The ideal endoscopic treatment strategy for Barrett's Esophagus is expected to provide complete eradication in a single session in an automated, reliable, cost-effective, and depthcontrolled manner, also, by being suitable for re-treatment without leading adverse effects, and avoiding the need for surveillance of buried glands.

This thesis aims to develop an endoscopic capsule providing a well-confined and anglecontrolled photothermal effect on the esophageal mucosa to treat superficial abnormal tissues such as Barrett's Esophagus potentially.

2. MATERIALS AND METHODS

The specific objectives that are planned to be completed to achieve the aim of the proposed thesis can be grouped under three main headings:

Objective-1: Creating a guiding map based on a computer simulation study,

Objective-2: Construction and quantitative evaluation of a prototype-level endoscopy system for well-confined photothermal mucosal ablation,

Objective-3: Development of a novel design endoscopy capsule for well-confined and anglecontrolled photothermal mucosal ablation.

2.1. Computer Simulation Study

A four-module computer modeling approach, shown in Figure 12, was developed to simulate laser-induced thermal effects. This computer simulation study combined mathematical models to mimic mucosal tissue's thermal dynamics/responses to characterize the total heat energy required for well-confined treatment depth.

The laser-induced thermal effect is mainly based on the laser-tissue interaction related to the wavelength-dependent optical properties of the tissue. In this context, Monte Carlo simulation has become a standard approach for studying light propagation in biological tissues based on statistical random sampling of a physical property. The heat transfer equation calculates the temperature by modeling the conduction of the physical property considered as the heat source according to the thermal properties of the tissue. The effect of increasing tissue temperature is estimated by the Arrhenius integral for tissue damage modeling based on the thermal kinetic properties of the tissue.

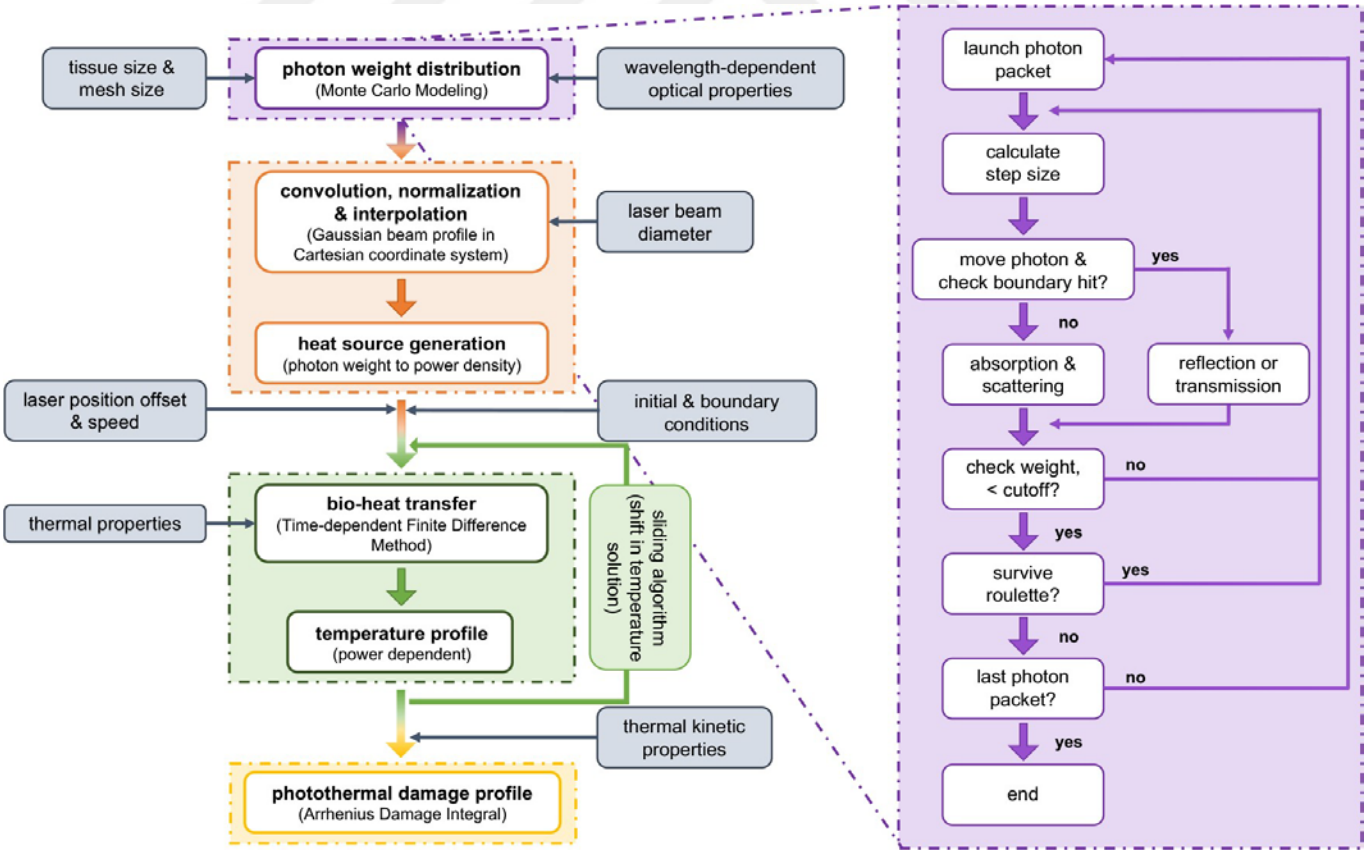


Figure 12: Flow diagram of four-module computer simulation study approach.

Table 5: Optical, thermal, and thermal kinetic properties used in simulation.

	Tissue	
Optical properties at 1505 nm	**Mucosa**	**Air**
Absorption coefficient, cm^{-1}	12[80]	0.001[81]
Reduced scattering coefficient, cm^{-1}	9.5 [80]	1[81]
Anisotropy factor	0.6 [80]	1[81]
Refractive index	1.33	1
Thermal properties	**Esophagus**	**Air**
Thermal conductivity, W/m°C	0.527 [82]	0.026[82]
Specific heat, J/kg°C	3720 [82]	1.006[82]
Density, kg/m^3	1126 [82]	1.3[82]
Kinetic coefficients	**Skin**	
Frequency factor, s^{-1}	$1.3e95$ [83]	
Activation energy, J/mol	$6.04e5$ [83]	
Universal gas constant, J/Kmol	8.32	

2.1.1. Monte-Carlo Based Modeling

The first module, Monte-Carlo modeling, is based on a stochastic approach to simulate physical processes and can be used for diagnostic and therapeutic applications of lasers in medicine. The method was first used by Adam and Wilson in 1983 for photon transport in biological tissues considering isotropic scattering [84]. Later, Keijzer *et al*. integrated anisotropic scattering into a simulation program that propagates photons using cylindrical coordinates [85]. In 1989 Prahl *et al*. restructured this program according to Cartesian coordinates [86] and finally, Wang and Jacques developed this work by writing a Monte Carlo Multi-Layered program [87].

The Monte-Carlo Multilayer (MCML) program identifies light propagation in a multilayer (turbid) tissue based on the particle – photon – nature to predict radiant energy transfer while ignoring light's phase and polarization properties. It simulates the propagation of an infinitely narrow photon beam perpendicular to infinitely large tissue layers, characterized by optical properties based on thickness (d, mm) and wavelength, including absorption coefficient (μ_a, cm^{-1}), scattering coefficient (μ_s, cm^{-1}), refractive index (n) and anisotropy factor (g). The absorption and scattering coefficients describe the probability of absorption and scattering events in one step. The anisotropy factor, which is the mean cosine of the scattering angle, determines the first-order probability distribution of the divergence angles. The simulation uses Cartesian, cylindrical, and spherical coordinate systems to track photon packets, score physical quantities, and sample the propagation direction change of a photon packet, respectively. Photon propagation in biological tissue modeled by the Monte-Carlo method follows the local rules described in the flowchart shown

with a purple rectangle in Figure 12. A unit-weighted packet of photons is initiated and transported to a distance where it can be absorbed, scattered, transmitted, internally reflected, or directly propagated. The motion of a photon is determined by a randomly sampled variable, which can be its step size or scattering angle. With each step, the unit weight of the photon decreases in proportion to its absorption probability. Photon propagation through scattering events continues until they are absorbed by the tissue or escape from the tissue boundary. If absorbed, the coordinate of the absorption event and the weight of the absorbed photon are recorded. If the photon hits a boundary, the reflection or transmission defined by another random selection is recorded. A threedimensional probability distribution of the accumulated laser energy is obtained by repeating this procedure for the desired number of photon packets. Increasing the number of photon packets improves the accuracy of recorded physical quantities and spatial resolution [88].

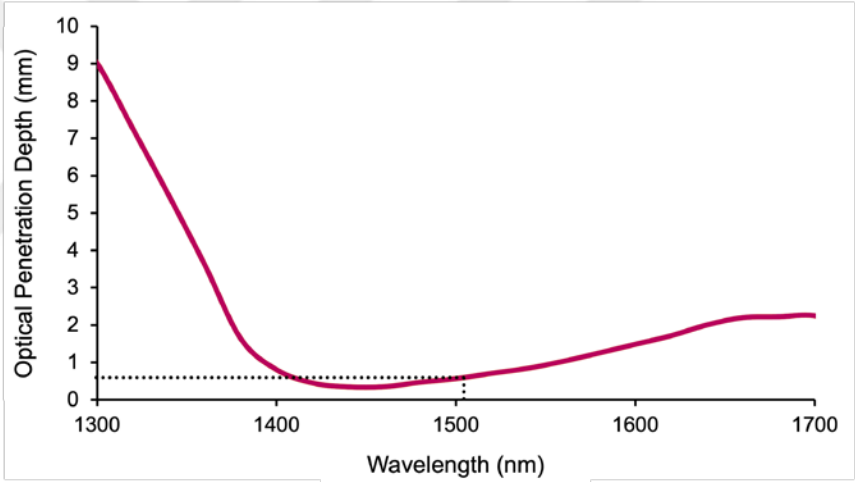


Figure 13: A plot of optical penetration depth of water as a function of wavelength [89].

Critically, the energy accumulation in the tissue may differ depending on the tissue type, laser wavelength, and even the operating mode of the laser. In other words, the optical penetration depth (OPD), defined as a measure of the depth at which light can pass through tissue, is affected by wavelength-dependent optical properties. As a general assumption, water is the primary absorbent in soft tissues, which makes up 70-80% of its content. Figure 13 shows the OPD plot of water as a function of wavelength; this indicates that 1505 nm has a penetration depth of 0.57 mm, which matches the thickness of the mucosa layer ranging from 0.4 mm to 1.00 mm [90-93].

For Monte-Carlo based modeling, the size of the mucosal tissue model was defined as 4 mm in all axes corresponding to the total thickness of the esophageal layers; mucosa, submucosa, muscularis propria, and serosa. The tissue model was built on a 100 × 100 × 100 uniform 3D grid system with a grid size of 40 μm. The optical properties of the mucosa tissue at 1500 nm were

compiled from the literature [80] (Table 5). An additional layer of air with same dimensions was defined over the tissue to position the laser beam at a certain distance. In the simulation, the total number of photons was 1 million to obtain an accurate propagation path and increase the spatial resolution. The MCML program was run with an input file with the extension ".mci" containing the specified variables (Figure 14a) and provided an output file with the extension ".mco" containing scored physical quantities such as absorption, reflectivity, and transmittance (Figure 14b).

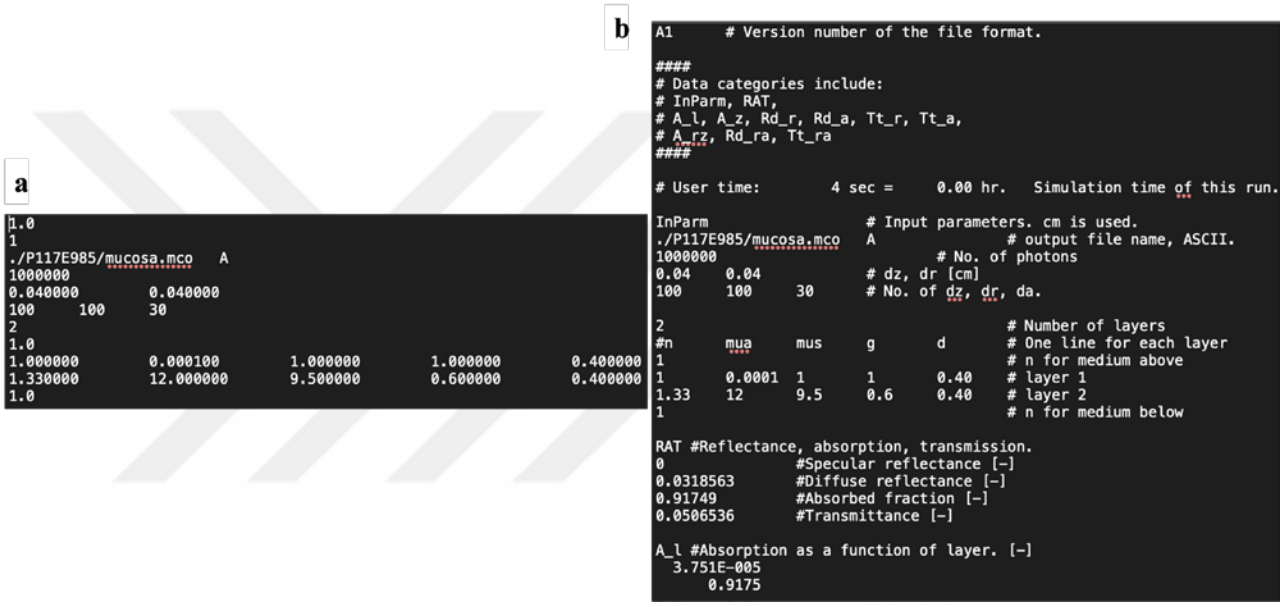


Figure 14: (a) Input and **(b)** output file of defined tissue model in Monte Carlo Multi-Layered (MCML) program.

In the simulation, the photon target on the tissue surface was determined as the origin of Cartesian (x,y,z) and cylindrical (r,z) coordinate systems, where the z-axis is the common axis and always perpendicular to the surface. Although photons were tracked in a Cartesian coordinate system, due to computational concerns such as time and storage, photon absorption was scored in a two-dimensional homogeneous grid system in the cylindrical coordinates shown in Figure 15a. With this, the simulation provides the numerical results for an infinitely narrow photon beam creating an impulse response. Nevertheless, this response is linear and invariant, allowing it to scale and shift horizontally.

Therefore, in the second module in orange, the fraction of photons absorbed per unit weight recorded in each grid element of a cylindrical coordinate system was normalized to 1 in power and convoluted with a Gaussian profile to respond to photon beams of finite size—0.9 mm. The

convolutional numerical results were then interpolated in a 3D grid in the Cartesian coordinate system and repositioned as a fractional heat source in the tissue (J/s/mm^3 or W/mm^3) based on the absorbed photon weight distribution, laser power per unit volume, and unit time, as shown in Figure 15b. The calculations of the second module were done on MATLAB (Mathworks, Inc).

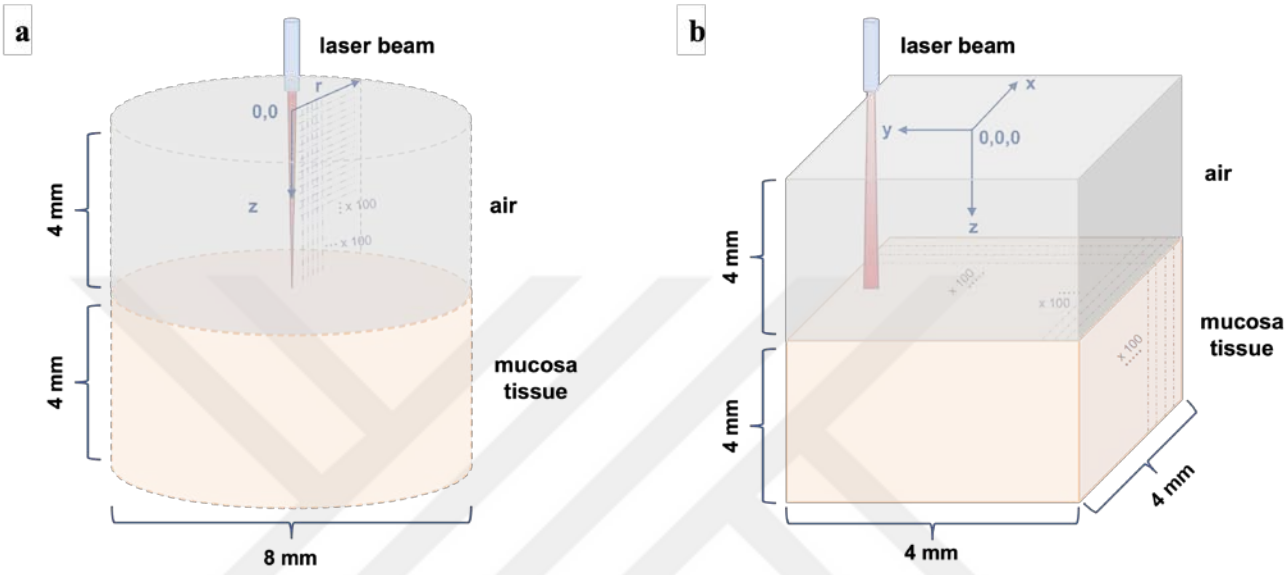


Figure 15: (a) Schematic representation of tissue model defined by cylindrical coordinate system at which physical quantities recorded in Monte Carlo Multi-Layered (MCML) program. **(b)** Schematic representation of the tissue model at which the convolved and repositioned numerical results interpolated in 3D Cartesian coordinate system.

2.1.2. Heat Transfer Modeling

The first law of thermodynamics states that energy is conserved between the system and the environment, although it varies in forms such as heat and mechanical work. In this context, the absorption of laser energy can induce different levels of biological tissues (i.e., tissue, cell, and organelle) through photothermal, photochemical, or photomechanical interaction mechanisms that cause immediate, delayed, or long-term responses displayed in Figure 16a, as the laser-tissue interaction cube. For the near-infrared spectrum, photothermal interactions are believed to be the primary mechanism leading to the conversion of laser energy into heat. Besides wavelength, the laser irradiation, the laser's mode of operation (i.e., quasi-continuous-wave or continuous-wave), and exposure time define the type of interaction and the corresponding tissue response. The distribution of light within the tissue, the initial tissue temperature, the temperature duration, and the tissue's thermal properties affect the form and extent of photothermal effects. For example, hyperthermia results from prolonged exposure to moderate temperatures and causes a delayed cell death response (Figure 16b), while photocoagulation results from brief exposure to high

temperatures. It causes sudden and significant changes in cells and tissues, followed by delayed and prolonged responses (Figure 16c) [94-96].

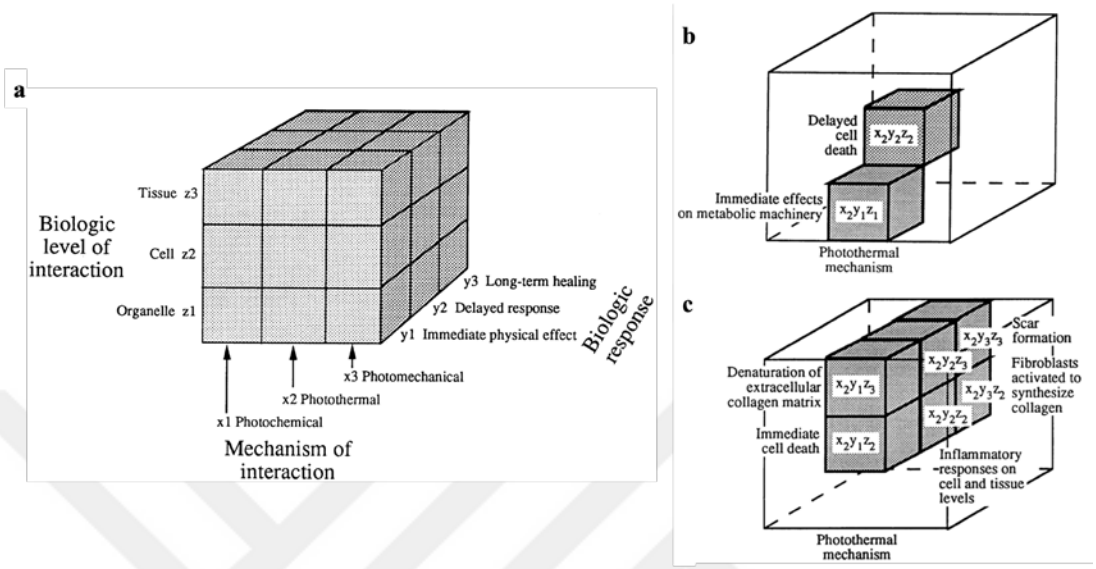


Figure 16: (a) Laser-tissue interaction cube having three axes: x – mechanism of interaction, y – biological response, z – biologic level of interaction. Exemplary demonstration of **(b)** hyperthermia and **(c)** photocoagulation with cube [95].

In this context, the third module, colored in green, simulated the heat diffusion produced by the laser energy accumulated in the tissue and obtained instantaneous temporary temperature results. The fractional heat source Q (W/mm^3) per unit volume per unit time calculated using modules 1 and 2 was used by a numerical model that governs the heat transfer equation (1) for an isotropic material,

$$\rho C \frac{\partial T}{\partial t} = \nabla (k \nabla T) + Q \quad (1)$$

where ρ is the density (kg/m^3), C is the specific heat capacity (J/kg ^{o}C), and k is the thermal conductivity (W/m ^{o}C), t is the time, and T (^{o}C) is the simulated tissue temperature. The equation was solved based on a partial differential equation using the finite time difference method (FDM) performed on Objective-C++ code written by Xcode. This method used the differential equation at a finite number of points in the conduction region. Spatial derivatives at a point were approximated using formulas for finite temperature differences, which led to algebraic equations (2),

$$\frac{}{\$\&} = \frac{}{2\#}\left(\left(\quad \%+\frac{}{(}\right)_{\$\%} \qquad 1 \qquad \nabla_{!}$$

$$+$$

$$\frac{\%"\&,\$',\%(-\%"\&,\$,\%}{\Delta t} = \frac{(}{pC}\ \nabla_{!}\ T+\frac{+",\$,\%}{2\#}$$

$$\%"\&,\$',\%(-\%"\&,\$,\%= \frac{\Delta t\ k}{}\ \nabla^{2}\ T+\frac{\Delta t\ Q}{}2\#\qquad 2\#",\$,\%$$

$$\%"\&,\$',\%(=\%"\&,\$,\%+\frac{\Delta t}{2\#}\left(\Delta\&+\right)7)8+\frac{}{2\#",\$,\%}$$

$$7)8=\frac{9:)}{}+\frac{9)8}{\$;!}+\frac{\$!\%}{\$<!}\qquad \$!\%$$

$$99):8=\%_{"'(,\$,\%}+2\%_{",\$!,\%}+\%_{"*(,\$,\%}$$

$$\ldots \qquad 2$$

$$)\qquad \Delta>$$

that are solved simultaneously for each grid point [97]. T^{n} represents the initial temperature of the tissue layer set to 37°C to mimic body temperature and 22°C for the air layer to mimic room temperature. Figure 17 shows a three-dimensional conduction region with evenly distributed grid points (a) of various configurations (inner, surface, and corner (b)) used differently according to the boundary conditions. In this way, a time-dependent temperature distribution (*i*, *j*, *k*) in space is obtained according to the conduction of the heat source and the initial temperature distribution.

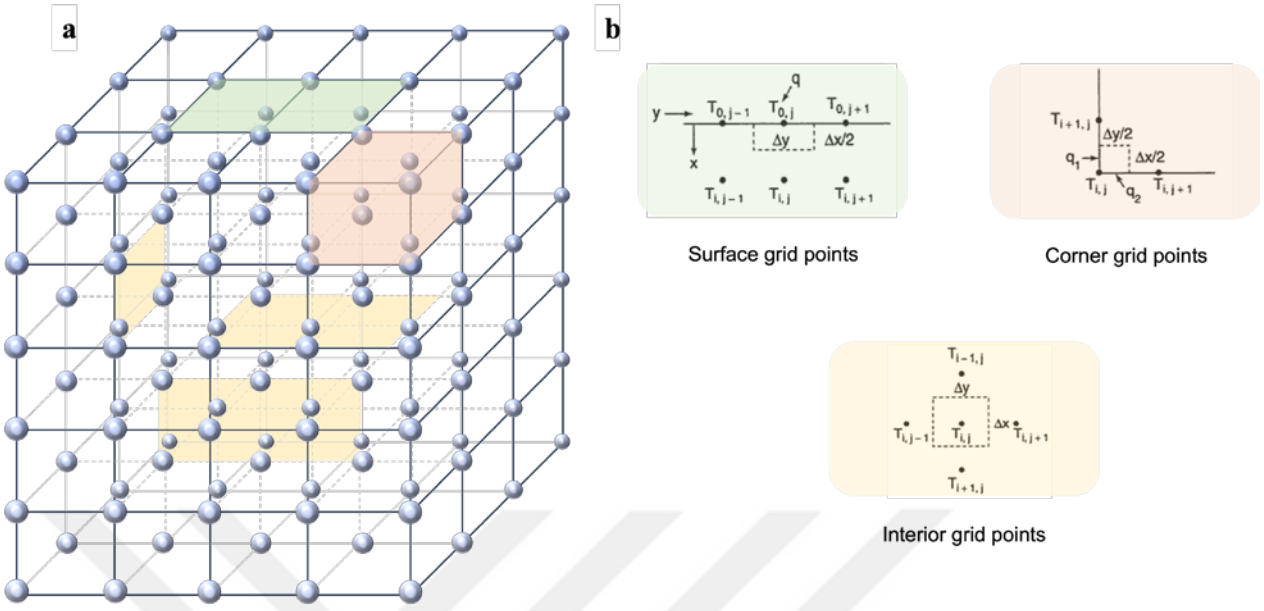


Figure 17: (a) Three-dimensional grid system showing a number of evenly distributed finite points in conduction region. **(b)** Conduction between the grid points is governed differently for surface, corner and interior regions regarding boundary conditions [97].

In the simulation, the grid system was defined to have 100 × 100 × 200 meshes of 40 µm size, the same as in Module 2. Esophageal and air thermal properties were compiled from the literature ([82], Table 5) and assigned to grids in the corresponding system layers. Although these layers were homogenous individually with the same thermal properties, the entire system had anisotropic properties. Therefore, the thermal conductivity (k) was considered position-dependent, ignoring the temperature dependence. Regarding this, k was interpolated in three axes (*x*,*y*,*z*) according to an average thermal resistance (1/k). In addition to conductivity, convective heat transfer was also considered for the air-intersecting surface of the tissue; therefore, the convection term (h) was integrated into k at this interface.

In addition to the heat transfer calculations, a shift algorithm was integrated into the third module to mimic the uniaxial sliding of the laser at a constant speed on the tissue surface. To do this, the initial position of the heat source in the grid system was shifted to the x-axis by interpolating the initial calculations with surface scanning speed and using the time-step solution as the initial condition for the next solution. Unit time is critical to obtain a stable finite difference approximation. According to matrix stability analysis (3), the numerical scheme can be conditionally stable if the system is three-dimensional,

$$1 (\Delta>)^{!}$$

$$\Delta\& < \frac{_}{6} \quad \frac{\quad}{C} \qquad 3$$

where C is thermal diffusivity (4),

$$C = \frac{(}{2\#} \qquad 4$$

[97, 98]. Therefore, the time step of the simulation was set to 10 microseconds to avoid discrete computations while maintaining stability. As a result, the transient temperature results of the equations solved simultaneously were saved as 1000 solutions evenly spaced from the high number of iterations due to limited memory usage.

Heat transfer simulation was repeated over 2.5 mm for scanning speeds of 0.5, 1, 1.5, 2, 2.5, 3, 5, 6, and 8 mm/s, and the laser power ranged from 60 to 500 mW at 20 mW intervals.

2.1.3. Thermal Damage Modeling

Due to photothermal interaction, temperature rise can lead to irreversible changes in tissue, known as thermal damage. The severity of thermal damage is primarily defined by the relative change in temperature, exposure time to high temperature, and reputation. Along with this thermal history, the tissue's intrinsic thermal properties and kinetic parameters define the degree of thermal damage. In 1990, Pearce [99] categorized the thermodynamic principles of laser-tissue interaction by three conditions: 1) low-temperature phenomena, 2) water evaporation, and 3) high-temperature events. Thomsen [100] then summarized the relationship between temperature, thermodynamic state, and associated histopathological outcomes as shown in Table 6. Observed histopathological effects indicate that thermal damage and related cell death result from irreversible protein changes with structural and functional roles in cells. In this context, thermal tissue damage can be explained by the kinetic protein denaturation/coagulation process that accumulates as a function of time for low-temperature events where metabolic heat and water evaporation are ignored. Henriques and Moritz [101-104] introduced the application of this process approach to thermal damage in 1947, based on the first-order approximation of the Arrhenius equation

(5)

$$\Omega = G \int_{,+} I_{!\$\%"\#} J\& \qquad 5$$

where ξ is the frequency factor of molecular collisions, τ is the total heating time, E_a is the activation energy of transformation, R is the universal gas constant, and T is the absolute temperature of the tissue in Kelvin, to generate a dimensionless thermal damage parameter – Ω – for each grid in time. Meanwhile, Ω can be expressed as the natural logarithm of the ratio of the original concentration of native/undamaged proteins (C_0) to those of remaining (C_τ) at time τ (6),

$$\Omega = \mathrm{OP}\,\frac{\#'}{\#_+}\mathrm{R} \qquad 6$$

Thus, the probability of denatured/damaged proteins (i.e., damaged/dead/necrotic cells) can be estimated at a given time by (7) [83]

$$(\%) = 100\,(1 - \#_+) = 100\,\frac{\mathrm{P}}{(1 - \mathrm{I}^{*})} \qquad 7$$

Using the Arrhenius damage integral, laser-induced thermal damage was estimated in the last module (yellow). The simulated temperature distributions for the different laser irradiance sets and surface scanning rates in Module 3 were calculated with the kinetic coefficients of the skin, where the critical temperature was close to 60°C, to predict thermal damage ([83], Table 5). The damage index, the probability of damage, which represents the proportion of coagulated proteins in a given volume, was produced by normalizing the thermal damage parameter to 1. Regarding protein denaturation/coagulation per unit volume of biological constructs, Ω corresponded to a concentration of 63% to 99% necrotic cells between 1 and 4.6. Unit volumes with an index greater than or equal to 98% (Ω=3.9) were considered thermally damaged tissue for damage estimates.

Table 6: Laser-tissue interactions: pathological photothermal effects [100].

Photothermal interaction	Temperature at onset (°C)	Uncommon adverse effects

Low temperature damage accumulation process	40-45 43-45+	? Deactivation of enzymes: reversible cell injury Deactivation of enzymes: cell death
	?	Cell shrinkage and hyperchromasia
	43+	Birefringence loss in frozen and thawed myocardium
	?	Thermal denaturization of structural proteins
	?	Membrane rupture
	58+	Hyalinization of collagen
	69-72	Birefringence loss in fresh myocardium
	70-75	Birefringence changes in collogen
	140+	Thermal denaturization of elastin
Water-dominated processes	100+	Extracellular vacuole formation
	Over 100	Rupture of vacuoles: “popcorn” effect
	?	Tissue ablation by explosive fragmentation
High temperature ablation	300-1000	Tissue ablation
	3550	Vaporization of carbon

From Thomsen S. Pathologic analysis of photothermal and photomechanical effects of laser-tissue interactions. Photochem Photobiol 53: 825-35, 1991.

As a result, a four-module computer simulation study generated a guide map of thermally damaged areas as a function of laser scanning speed and irradiance. While mapping, the peak temperature was monitored from the surface transient temperature calculations for each pair of surface scanning rate and laser power, sampled for 1mm/s speed and 309 mW power in Figure 18a. Next, cross-sectional results of the temporal temperature distribution in the xz plane at a lateral position on the y-axis, where the peak temperature used to calculate the thermal damaged area, are shown in the dashed dark red line in Figure 18b. The corresponding laser irradiance was calculated based on the surface area scanned by the laser beam at a diameter distance. This area was estimated as the square of the beam diameter, assuming >99% overlap of the laser beam. Therefore, 60 to 500 mW laser power corresponded to a radiation range of 7.4 to 61.7 W/cm^2 for a diameter of 0.9 mm.

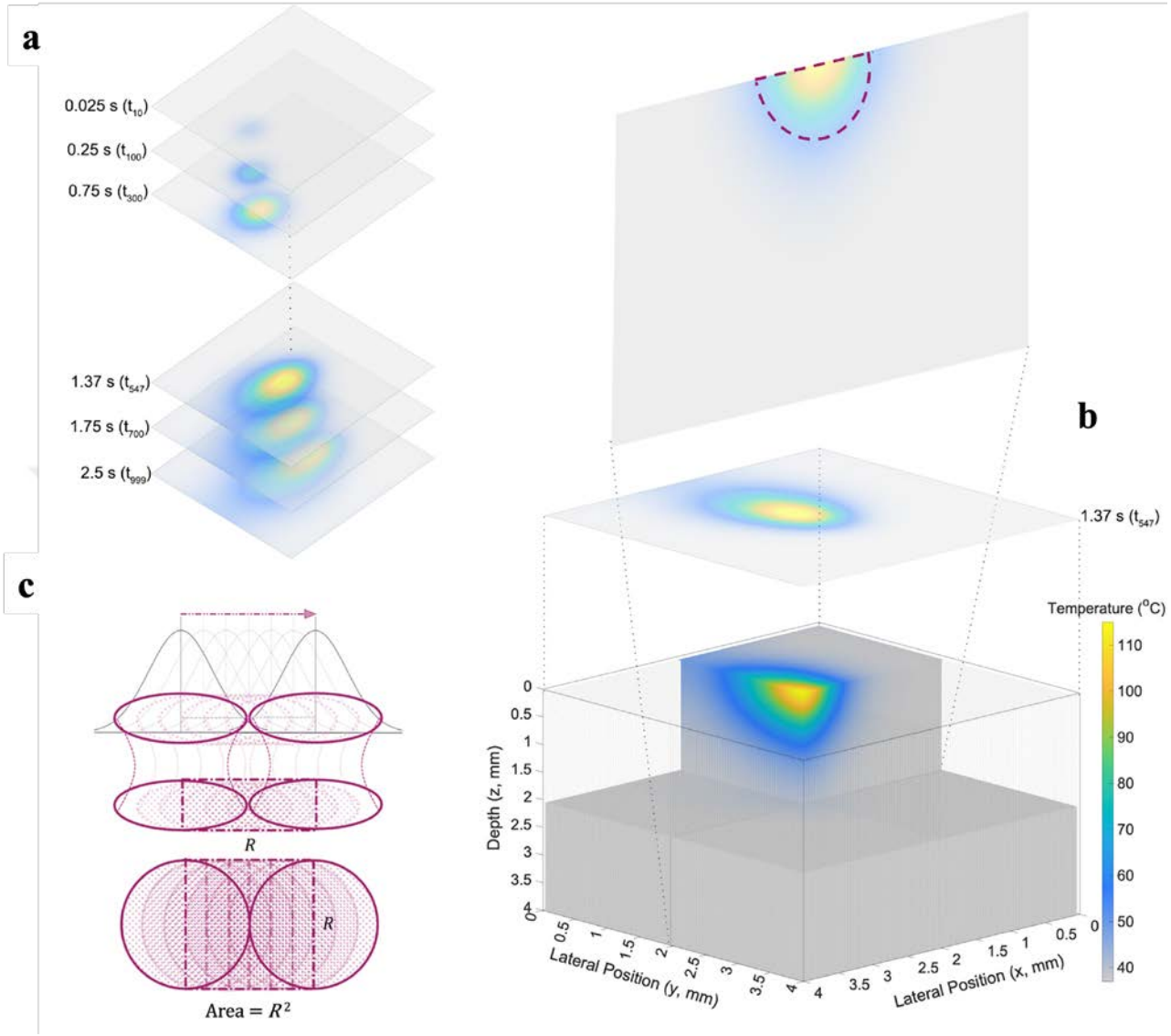


Figure 18: (a) Temporal temperature estimates from the surface at selected time points ranging from t_0 to t_{999}, which range from 25 ms to 2.5 s. **(b)** 3D transient temperature distribution at which the highest temperature is attained in the tissue model. The thermal damaged area (dashed dark red line) is calculated regarding the cross-sectional temperature results for a pair of parameters. Laser power = 309 mW (48.6 W/cm^2), beam diameter = 0.9 mm, scanning speed = 1 mm/s. **(c)** Given that the laser beam overlaps by >99%, the surface area perpendicular to the propagation of the beam is considered to be square and roughly equals to square of the beam diameter for computing laser irradiance (Surface area = R^2).

2.2. Experimental Setup for An Ex vivo Tissue Model

An experimental study was performed with an ex vivo tissue model for a specific laser wavelength (1505 nm) and narrowed parameter pair range to validate the simulation results.

2.2.1. Characterization of Optical Components

In the experimental study, a single-mode diode laser (BrightLock; QPC Lasers Inc.) coupled with a pigtailed gradient index (GRIN) collimator (Go4Fiber, Figure 19d) placed in a glass tube was used to deliver laser energy to the tissue. In this context, the laser beam transmitted through the GRIN lens was first profiled using the knife edge method [105] shown in Figures 19a and 19b. In this method, the knife edge (i.e., a razor blade) is positioned perpendicular to the emitted laser beam and moved to cut the laser power as a function of blade position at x. A photodetector measures the transmitted power. Figure 19c shows a close-up photograph of the GRIN lens and razor blade in a beam profiling setup. The position of the razor blade was adjusted with a step size of 50 µm along the x-direction with the translation stage connected to motorized micrometer actuators (Z825B; Thorlabs). The photodetector (PM122D; Thorlabs) measured the power of the clipped beam for each step.

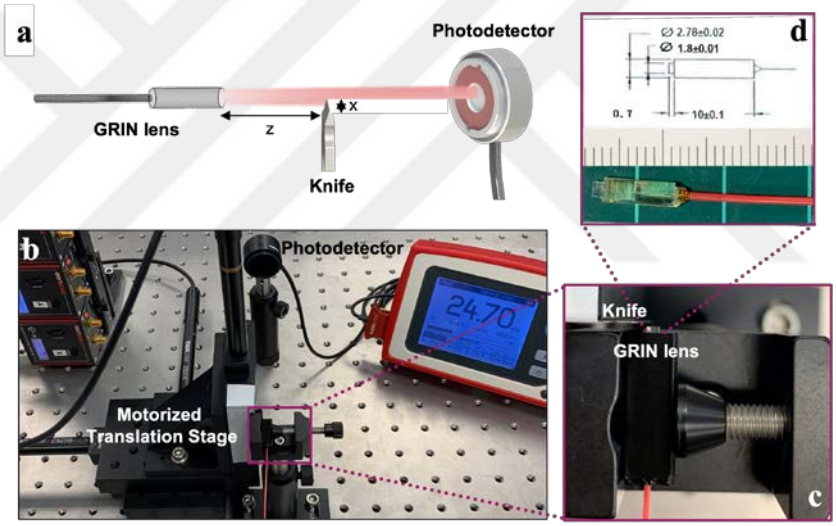


Figure 19: (a) Schematic representation of the knife-edge method for beam profiling. **(b)** Photograph of the setup used to profile laser beam transmitted through gradient index (GRIN) lens. **(c)** Closeup image of GRIN lens in setup and **(d)** its dimensional specifications.

Two steps were followed to determine the beam waist: The measured laser power was normalized to 1. Next, the distance between the positions of the laser power transmission at 16% and 84% was noted. The distance corresponding to $1/\sqrt{e}$ in the radial intensity distribution calculated by the Gaussian first derivatives gives the beam radius (w). Thus, using the knife edge method, the $1/e^2$ diameter of the laser beam produced by the GRIN lens was estimated to be ~0.9 mm at a distance in the z direction (~ 70 mm). The distance corresponds to the free space between the GRIN lens and tissue in the experimental study (Figure 20a).

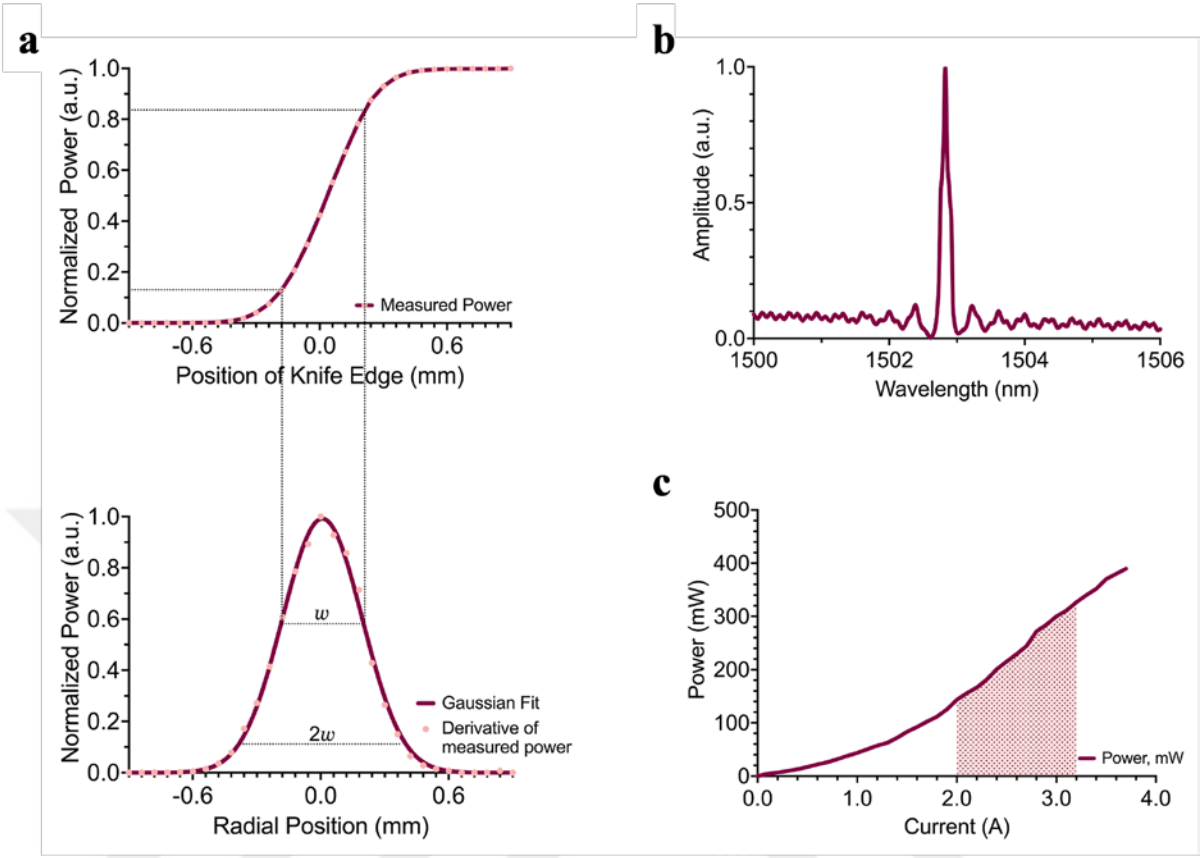


Figure 20: (a) The normalized powers of the laser obtained at the knife-edge position and Gaussian-fitted first derivatives at the radial position. The laser beam produced by the GRIN collimator lens had an estimated beam diameter of ~0.9 mm ($1/e^2$). **(b)** The measured wavelength of the laser was 1502.83 nm according to the emission spectrum. **(c)** A plot of the output laser power provided through the lens as a function of electric current. The faded pink area demonstrates the employed power range from 133 to 309 mW.

Figure 20b shows the emission spectrum of the diode laser measured with a spectrum analyzer (AQ6370D; Yokogawa Electric). The measured wavelength is 1502.83 nm, close to the wavelength defined in the simulation studies. The output power transmitted through the GRIN lens was also measured as a function of the applied electric current. The pink area indicates the power range (133–309 mW) used during ex vivo studies (Figure 20c).

2.2.2. Experiment with An Ex vivo Model

Figure 21a shows the schematic drawing of the experimental setup used in the ex vivo tissue study for photothermal coagulation. The setup includes a single-mode fiber-coupled diode laser as the near-infrared laser source and a pigtailed GRIN collimator. The GRIN lens was a probe that moved over the tissue surface using identical motorized micrometer actuators (Z825B; Thorlabs). The actuator provides a maximum travel distance of 25 mm with a step size of 0.029 µm and a

speed of up to 2.3 mm/s. The ex vivo sheep esophagus was obtained from a slaughterhouse and handled according to the protocol (see Appendix 7.1) before and after experimentation. We dissected ex vivo tissue lengthwise to fit evenly on the inner surface to get a rectangular form. The tissue surface was gently flattened using a small metal spatula. The tissue was then placed in a tray in contact with a hot plate (Thermo Fisher Scientific) set to 45°C to bring it to body temperature (37°C). A thermocouple monitored the surface temperature during the experiment. Besides, we used a digital microscope (AM4815ZTL; Dino-Lite) to align the probe and record the physical changes of the photothermal coagulation process in the invisible wavelength range.

The protocol followed in the ex vivo study is illustrated in Figure 21b. While the laser power was increased for each line, the surface scanning rate was kept constant for each pattern. This model used seven output power ratings (133, 150, 188, 220, 258, 284, 309 mW) for surface scanning speeds of 0.5, 1.0, 1.5, and 2.0 mm/s. After photothermal coagulation, gross images of tissue surfaces were taken, and tissues were fixed in 10% neutral formalin to preserve their current state. Fixed samples were then embedded in paraffin to prepare for sectioning. 5-μm thick longitudinal sections were cut from paraffin blocks and processed for standard histology analysis by hematoxylin-eosin (H&E) staining. H&E-stained samples were examined at 4X magnification under a light microscope (IX71S1F-3; Olympus Corporation) to quantify the extent of thermal damage. The samples' brightfield and darkfield images were obtained simultaneously in this context. We mathematically subtracted darkfield microscopy images from brightfield microscopy images (Figures 22a, 22b) using ImageJ to obtain a high-contrast image with morphological details. This approach provided an image enhancement with minimal digital process load. The resulting image (Figure 22c) helped to easily distinguish between coagulated and non-coagulated regions for measurements of thermally damaged areas. Some unstained tissue sample pieces were coated with 5 nm thick gold using a rotary pump coating system for electron microscopy examination.

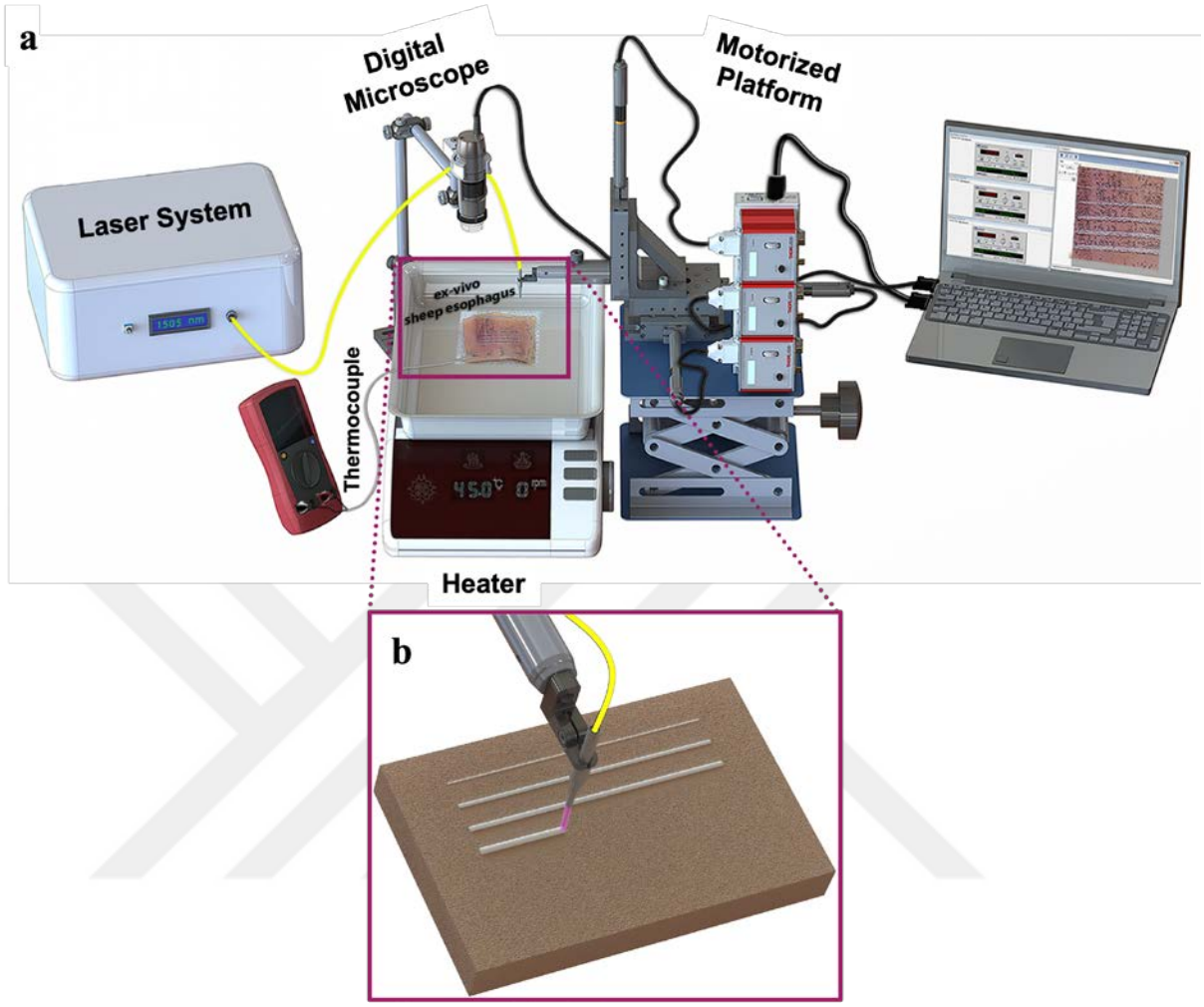


Figure 21: (a) Schematic illustration of the experimental setup employed for the ex vivo sheep esophagus study. A single-mode diode laser engaged with a pigtailed GRIN lens, a linear translation stage, a thermocouple, a digital microscope, and a hot plate are all included in the experimental setup. **(b)** Schematic diagram of the procedure followed in experiments.

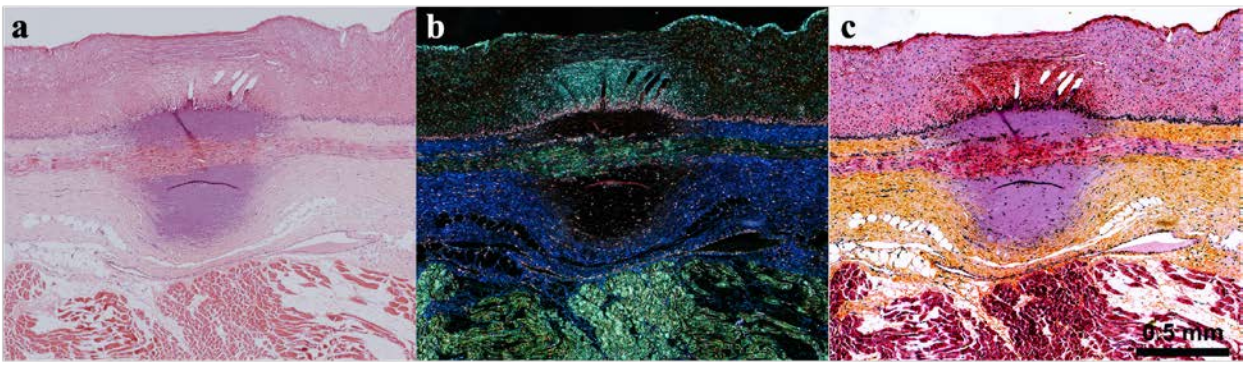


Figure 22: An exemplification of emphasizing morphological information and contrast in a thermally affected region with color subtraction approach. **(a)** Brightfield microscopy image and **(b)** darkfield microscopy image of e hematoxylin-and-eosin-stained ex vivo sheep esophagus and **(c)** the color subtraction result at ×4 magnification. Scale bar = 0.5 mm.

2.3. Capsule Design #1

After simulation and ex vivo validation studies, the convenience of the laser wavelength and the GRIN lens was verified. Later, construction and quantitative evaluation of a prototype-level endoscopy system for well-confined photothermal mucosal ablation were carried out.

2.3.1. Design

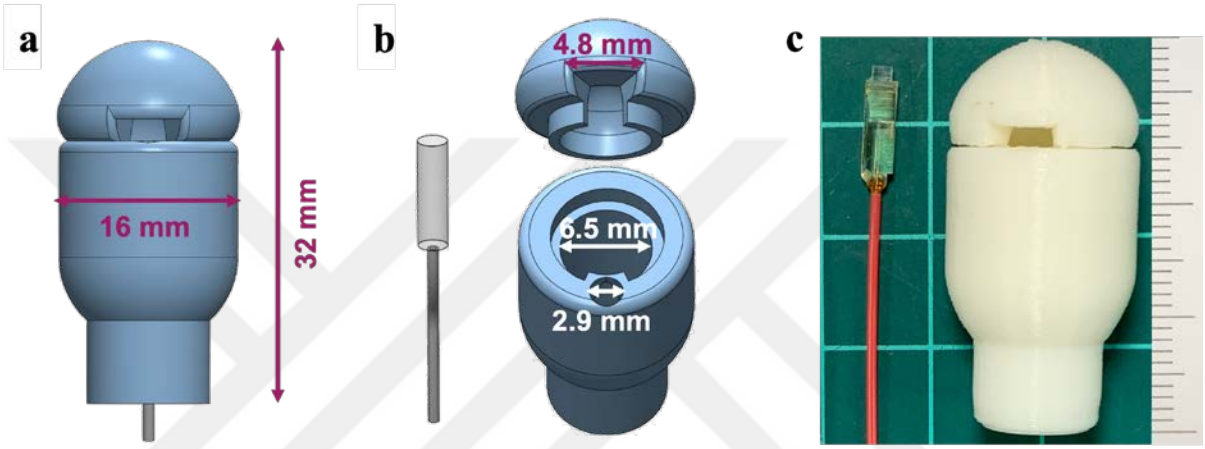


Figure 23: (a) Schematic illustration of endoscopy capsule #1. **(b)** The capsule consists of two parts: the cover, and the body including a large and a small hole for transmission of negative pressure and delivery of laser beam, respectively. **(c)** A photograph of the capsule printed by a 3D from biocompatible polylactic acid.

Figure 23a shows a schematic illustration of the 3.2 cm long and 1.6 cm wide endoscopy capsule #1 (SOLIDWORKS; education version). The capsule consisted of two parts: a cover and a body. The body part had a large hole (⌀ 6.5 mm) to transmit the negative pressure to the recessed area and a small hole (⌀ 2.9 mm) to fix the GRIN lens, collimating the laser beam (Figure 23b). Figure 23c shows a photograph of the endoscopy capsule printed with a 3D printer (CR-10S Pro V2; Creality) from biocompatible polylactic acid (PLA).

While creating the tissue model, firstly, the capsule design approach was simulated. For this simulation, the mcxyz.c program and the support programs written in MATLAB defined the complex layer structures in the tissue [106]. The same optical and thermal properties of the tissue were used in Modules 1, 2, and 3 as in the previous simulation study. The grid size of the model was set to 20 µm to achieve higher spatial resolution.

In the simulation, the beam diameter was defined as 0.5 mm based on the knife-edge method measurements in which the razor blade was positioned next to the surface of the GRIN lens, corresponding to ~ 1mm in the z-direction. Considering the highest power obtained from the laser

source, the laser power was determined as 400 mW. Associated graphs are shown in the following section.

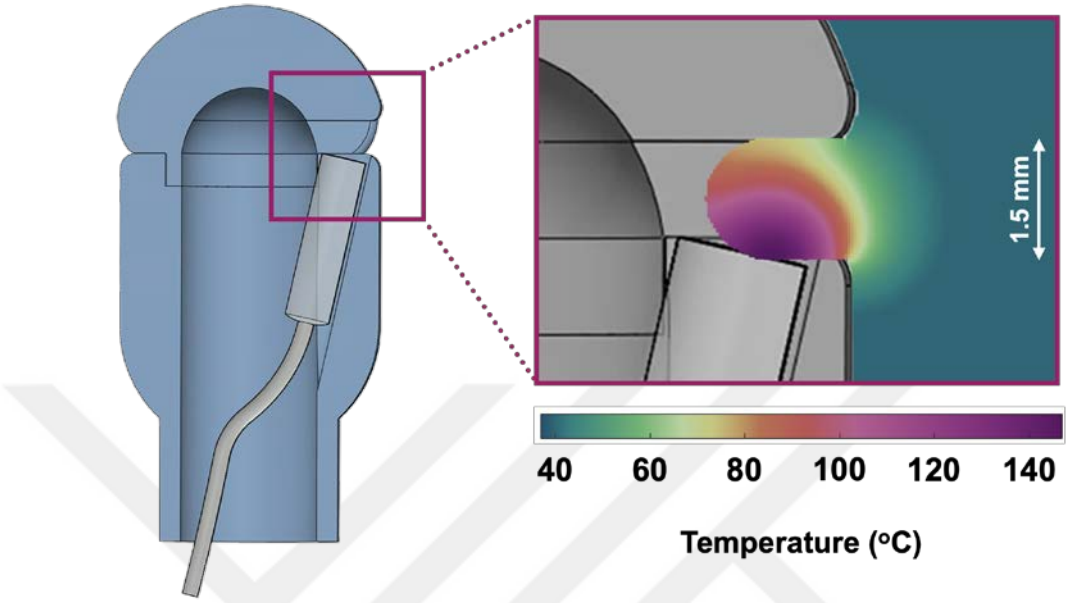


Figure 24: A simulation result of transient temperature to verify that the approach results in the confinement of the therapeutic effect to the recessed area. Beam diameter = 0.5 mm, grid size = 20 µm, laser power = 400 mW for 1 second.

Figure 24 demonstrates the transient temperature results after a 1-second simulation confirming that the tissue in the recessed area has reached a sufficient temperature (>65°C) for thermal damage. Additionally, the simulation suggested that the approach traps heat rather than heat flux to surrounding and deep tissues. Because this simulation was performed only to understand the feasibility of the proposed approach, it was not repeated for any other parameters. Also, the last module was skipped.

2.3.2. Characterization of Optical Components

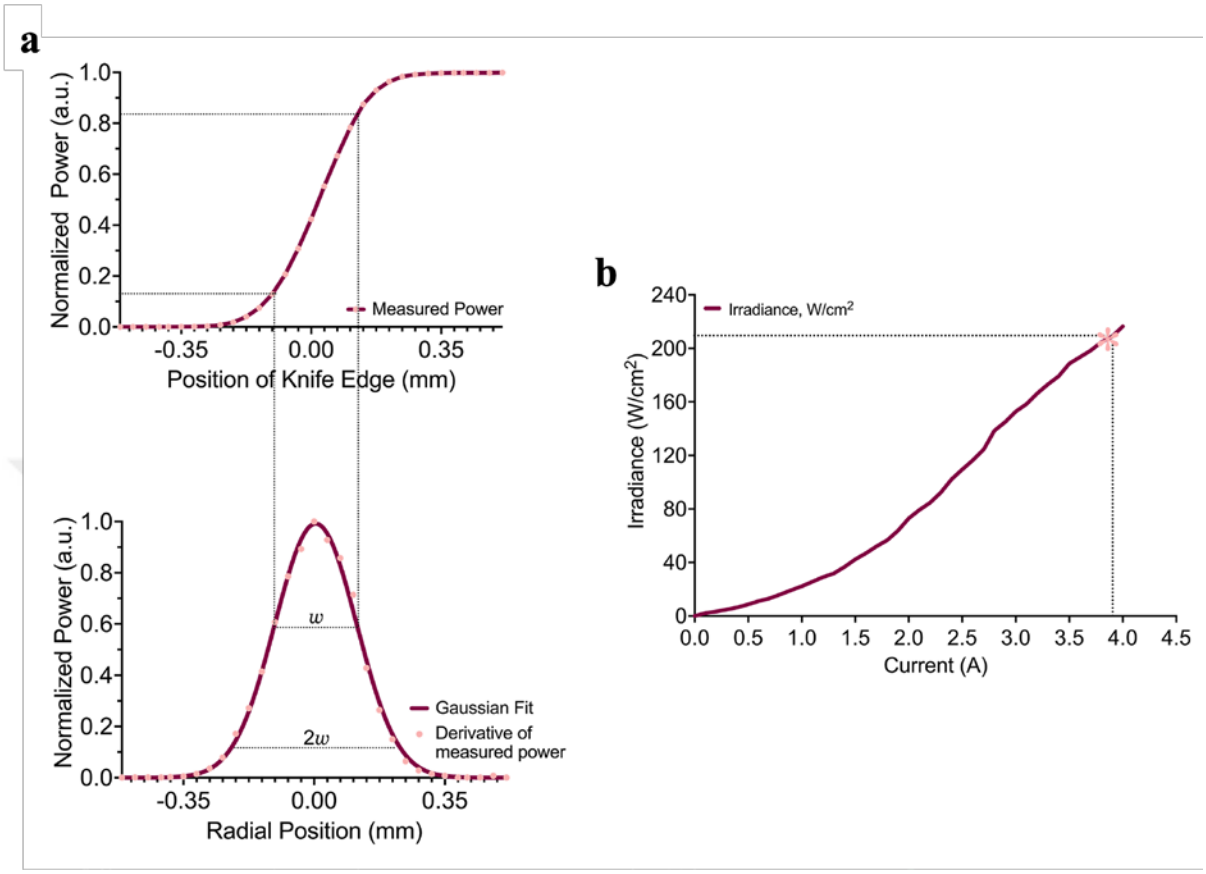


Figure 25: (a) The normalized powers of laser obtained at the knife-edge position and radial position and Gaussian-fitted first derivatives at the radial position for endoscopy capsule #1. The predicted laser beam diameter was ~0.5 mm ($1/e^2$). **(b)** Estimated laser irradiance as a function of electric current applied to the diode. The asterisk marks 208.8 W/cm^2 used in this study.

Figure 25a shows the normalized laser powers as a function of the knife-edge position and corresponding Gaussian-fitted first derivatives, respectively. The estimated diameter of the laser beam was ~0.5 mm. Regarding the measured beam diameter, Figure 25b shows the estimated laser irradiance as a function of the electric current applied to the diode, and an asterisk marks the irradiance (208.8 W/cm^2) used in this study.

2.3.3. Characterization of Electrical Components

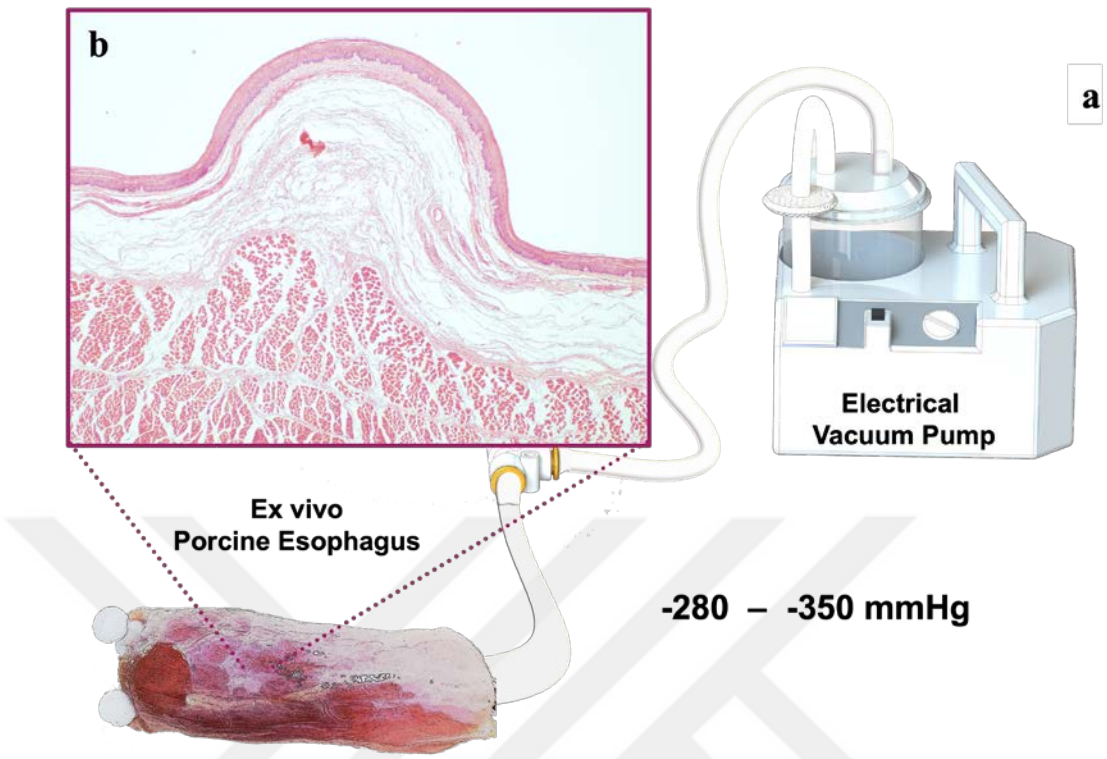


Figure 26: (a) Schematic drawing of the setup for preliminary study performed to determine optimal negative pressure. **(b)** A cross-sectional image of a hematoxylin-and-eosin-stained porcine esophagus tissue sample to confirm the delimitation of mucosal and superficial submucosal layers from deeper layers via the negative pressure (×4 magnification).

In this section, the concept of limiting the superficial esophageal tissue to a specific volume with vacuum aspiration is tried to be explained. An electric vacuum pump (pM-7E A; Plusmed) created negative pressure to stretch the superficial tissue layers into the recessed area of endoscopy capsule #1. Before the experiment, a preliminary study was conducted with the setup shown in Figure 26a to determine the optimal negative pressure to lift the mucosal and superficial submucosal layers. The endoscopy capsule #1 was connected to the electric vacuum pump with silicone tubing, and the joint points were closed with Teflon tape. Ex vivo porcine esophagus specimens were subjected to negative pressure through the capsule, inserted for 5 minutes, and immediately fixed with a 10% neutral formalin solution. The applied negative pressure varied between -280 mmHg and -700 mmHg. Histology results confirmed that negative pressure of -280 to -350 mmHg was valid for proper stretching without tearing, and other studies also confirmed this finding [107, 108]. Example H&E-stained sample (Figure 26b) represents the effect of -350 mmHg pressure on ex vivo porcine esophagus.

2.3.4. Assembly of the Endoscopy System

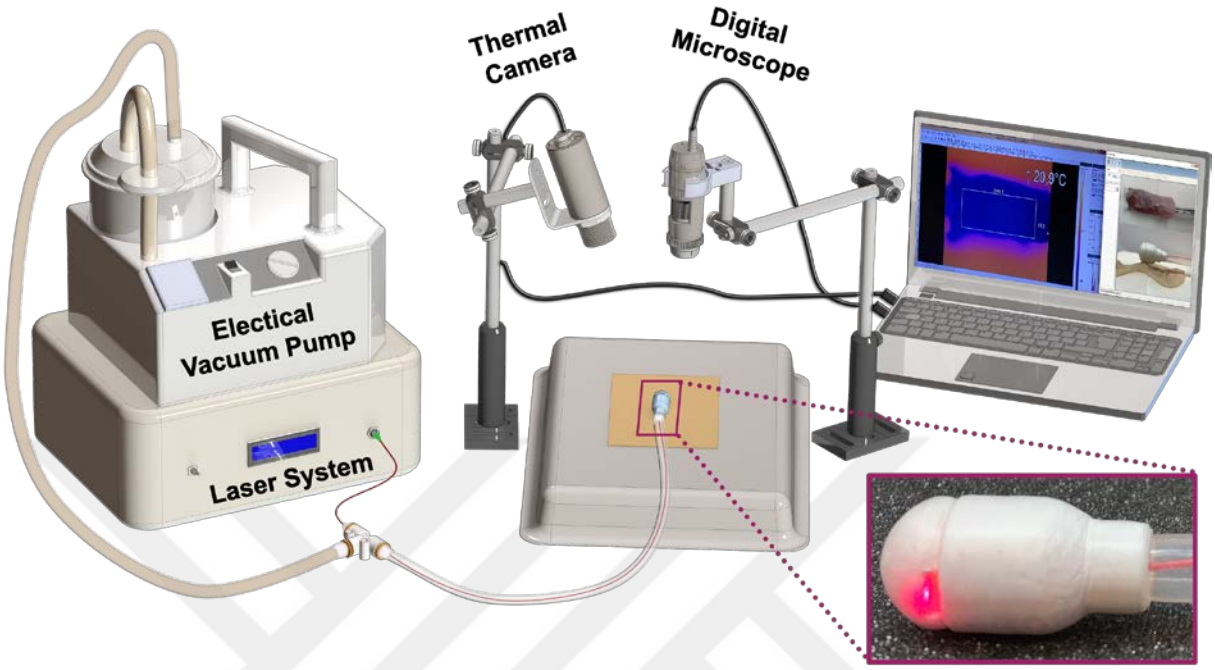


Figure 27: Schematic drawing of the experimental setup with an enlarged view of the capsule #1 presenting that the 660 nm aiming beam aligns the infrared laser toward the recessed area for photothermal coagulation.

The prototype-level endoscopy system was built with a single-mode diode laser and an electric vacuum pump connected to the capsule #1. Figure 27 presents a schematic drawing of the experimental setup, including the endoscopy system for examining the capsule's performance in a porcine esophagus model with an enlarged view of capsule #1 showing a 660 nm aiming beam aligning the infrared laser towards the recessed area.

The tissue was locally exposed to -300 mmHg negative pressure and 208.8 W/cm^2 laser beam for 5, 8, 10, 13, 15, 18, 20 and 25 seconds. A thermal camera (Xi400; Optris) with an emissivity of 0.93 and a thermal sensitivity of 80 mK measured the temperature change of the tissue from the muscle surface, while a digital microscope facilitated the visual monitoring of the tissue. Thus, the thermal effect in the deep tissues was observed from the outer surface.

A control study was performed to confirm that stretching the mucosal layer towards the recessed therapy area limits the depth of the thermal effect. For the control group shown in Figures 28a and 28b, the laser irradiation was collimated at the target esophageal tissue, and temperature changes were monitored across the muscle layer for direct comparison.

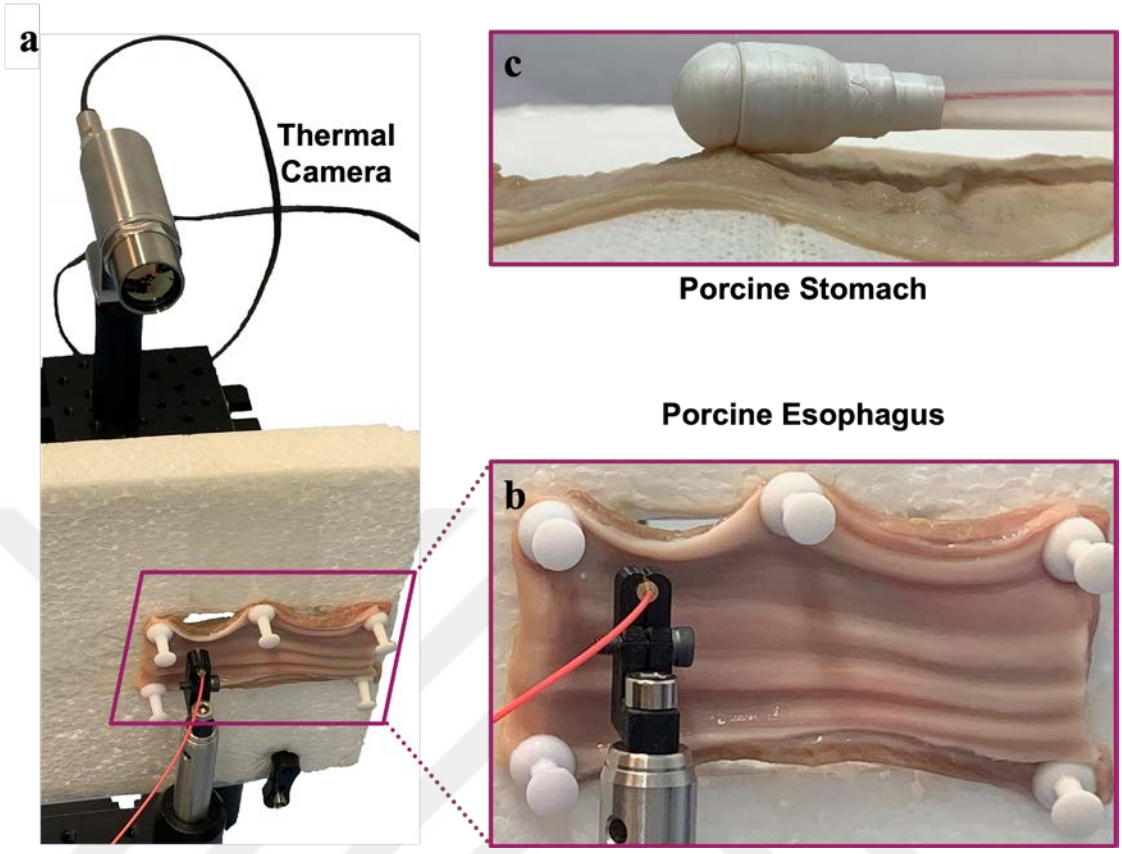


Figure 28: (a) A photograph showing the control study without using the capsule #1 with **(b)** the closeup view of tissue during laser irradiation. **(c)** A photograph showing the other control study of capsule #1 with the fundus region of the porcine stomach that mimics the abnormal esophageal tissue type (e.g., Barrett's Esophagus), albeit limited.

To understand the performance of capsule #1 on the ultimate target tissue, another control study was performed in a porcine stomach (Figure 28c) that mimicked the abnormal esophageal tissue type (e.g., Barrett's Esophagus) due to cell types and structural organization [109-111].

Tissue samples were treated according to the protocol (see Appendix 7.1) before and after laser irradiation.

2.4. Capsule Design #2

After building a prototype-level endoscopy system and validating the negative pressure approach to limit the depth of thermal damage, the final design of the new endoscopy capsule for angle-controlled photothermal mucosal ablation/coagulation was carried out.

2.4.1. Design

Figure 29a shows the outline of endoscopy capsule #2, which is 4.4 cm long and 2 cm wide. The capsule #2 consists of three parts: cap, body, and base. The cap and base parts were 3D printed from biocompatible polylactic acid (PLA), while the perforated body was fabricated from Optically transparent and biocompatible polymethyl methacrylate (PMMA) by Computer Numerical Control – CNC – machining (Figure 29b).

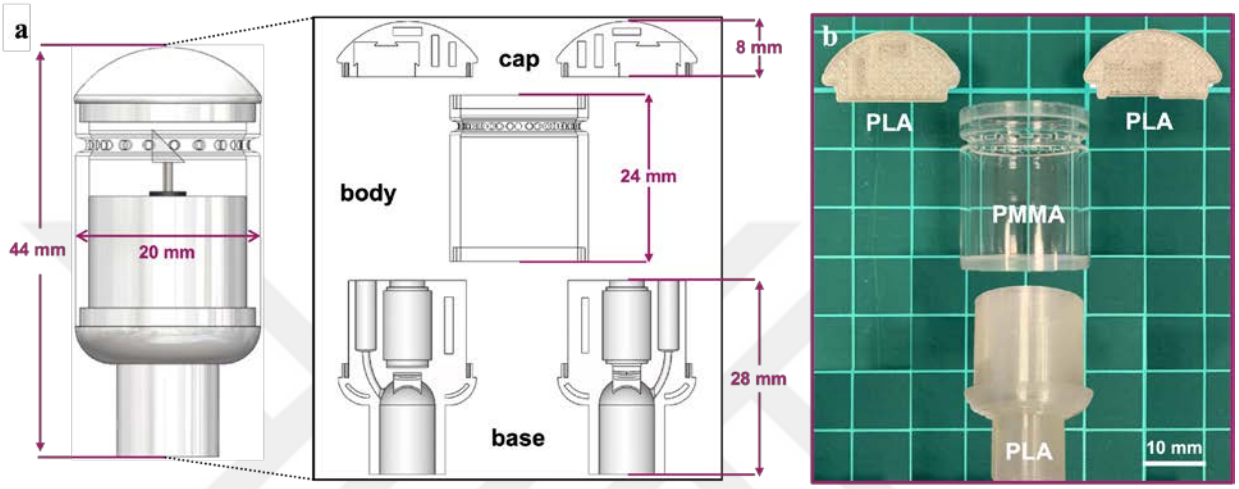


Figure 29: (a) An overall outline of endoscopy capsule #2 containing three parts: cap, body, and base. **(b)** A photograph of 3D printed (cap and base) and CNC machined (body) parts of the capsule #2.

Figure 30 demonstrates the cross-sectional view of capsule #2 with embedded optical and electrical components. The base contains a GRIN lens (1) to transfer a laser beam to the capsule and a stepper motor (2) (DM06202R004011, Faulhaber) with an attached gold-coated right-angle prism mirror (3) (MRA03-M01, Thorlabs) for the rotational motion of the laser beam. The optically transparent and perforated body part unites the base and cap. The cap includes two gold-coated, right-angle prism mirrors (3) to direct the laser beam through the mirror fixed to the stepper motor.

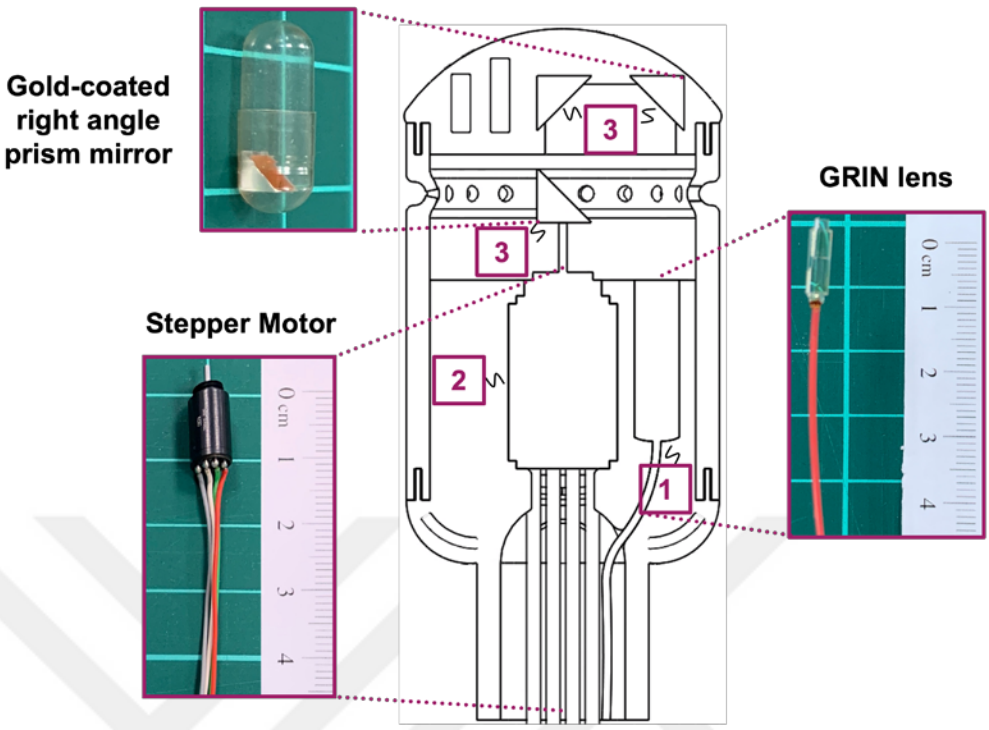


Figure 30: Cross-sectional view of the capsule #2 with the embedded optical and electrical components: (1) GRIN lens, (2) stepper motor, (3) gold coated right angle prism mirror.

Figure 31 indicates the steps of the assembly process of capsule #2. Initially, the stepper motor was placed in the middle of the base, and the GRIN lens was placed vertically next to the stepper motor (Figure 31b). One of the mirrors was then attached to the top of the motor shaft in the middle of the capsule (Figure 31c). Figure 31d shows the partially assembled endoscopy capsule. After ensuring the integrity and strength of the mirror placed on the shaft, the mirrors on the cover were aligned with the laser beam on the middle mirror and fixed on the cover (Figures 31e, 31f). Figure 31g shows the assembled capsule #2.

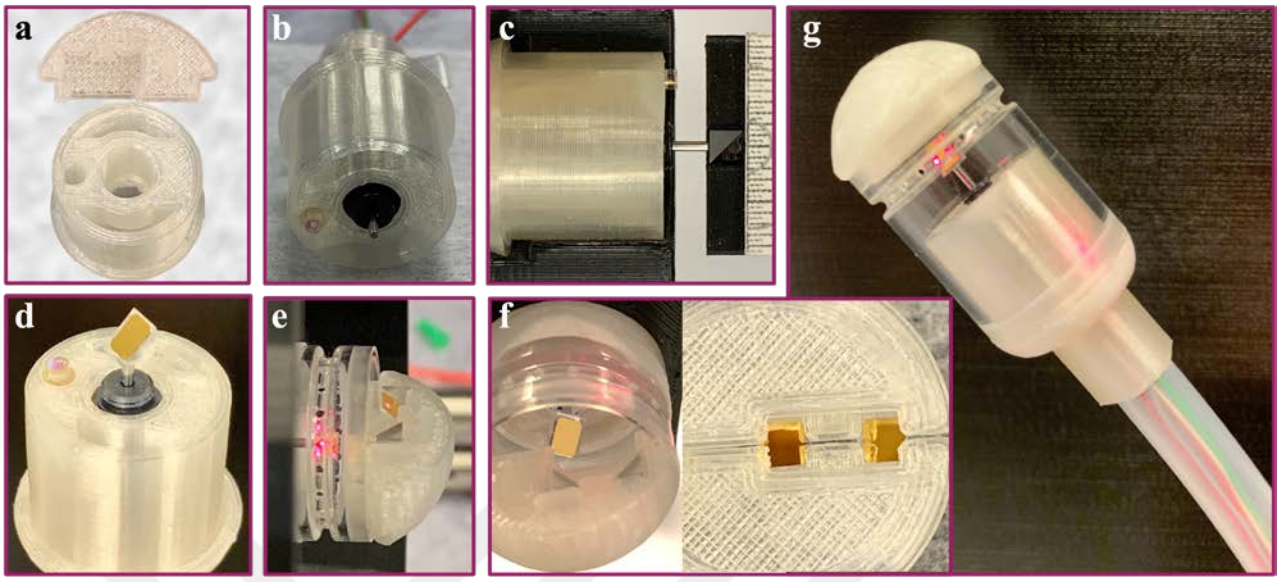


Figure 31: (a-g) Stages of assembly process of capsule #2.

2.4.2. Characterization of Optical Components

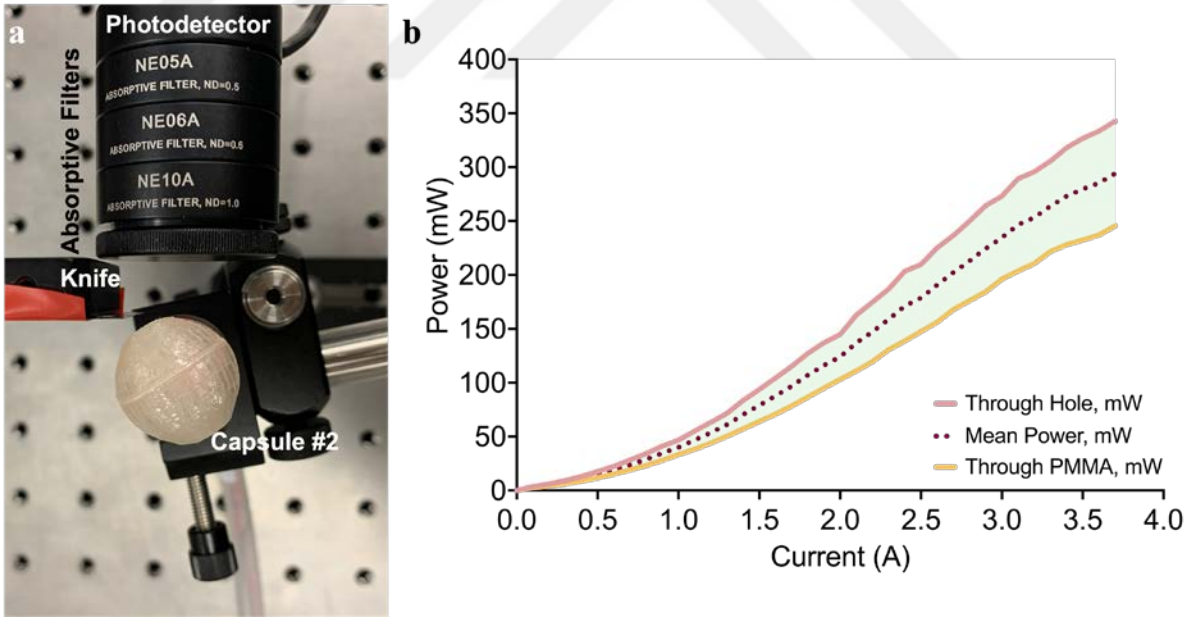


Figure 32: (a) A photograph of the setup used for measurements of capsule #2. **(b)** A plot of the output laser power transmitted through the hole and the PMMA surface of capsule #2 as a function of electric current. The dashed dark red line shows the mean power, and the green area indicates the power range provided by capsule #2.

As described in the previous section, the single-mode diode laser and GRIN lens were characterized by output power and beam diameter parameters. These parameters were then accurately measured when using the PMMA body of capsule #2. Measurements were made from the PMMA surface and a 1-mm hole to provide vacuum suction in the slot. Figure 32a shows a

photograph of the setup used for the measurements. The beam diameter was estimated to be ~0.4 mm from the PMMA surface and through the hole based on repeated measurements. Figure 32b shows the graph of measured output power from PMMA surface (yellow line) and from the hole (pink line) with the calculated mean power (dashed dark red line) as a function of applied electrical current.

2.4.3. Characterization of Electrical Components

The electric vacuum pump was connected to capsule #2. Its air tightness was checked by wrapping Teflon tape around the capsule's slot, and then the negative pressure approach to stretch mucosal and superficial submucosal tissue was applied to the ex vivo tissue at a negative pressure of -300 mmHg (Figure 33).

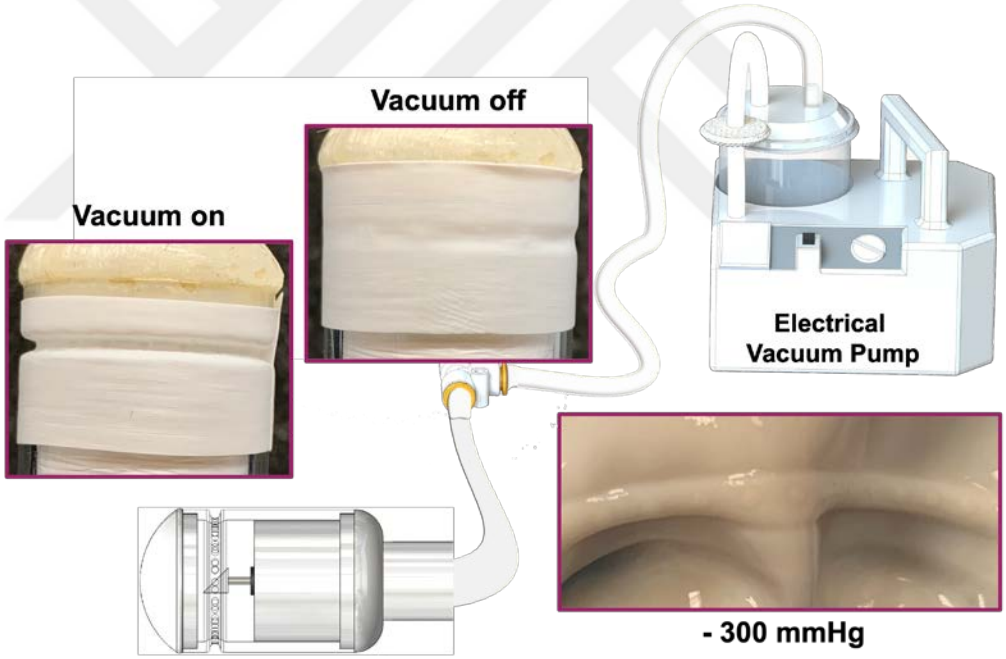


Figure 33: Schematic drawing of the setup for controlling the transmission of negative pressure through the capsule #2 implemented on teflon tape and ex vivo tissue.

Table 7 shows the technical specifications of the stepper motor, which is the other electrical component of the system.

Table 7: Technical specifications of the stepper motor.

Faulhaber DM06202R004011 Stepper Motor Technical Specifications		
Nominal current	0.04	A

Nominal voltage	6	V DC
Phase resistance (20°C)	120	Ω
Phase inductance (1kHz)	18.5	mH
Back-EMF amplitude	1.6	V/k step/s
Torque (at nominal current)	0.25	mNm
Torque (at twice nominal current)	0,39	mNm
Step angle (full step)	18	degree
Steps per revolution	20	
Rotor inertia	$0.5*10^{-9}$	kgm^2
Mass	1.1	g
Diameter	6	mm
Length	9.5	mm
Total Length	14.7	mm

Figure 34 shows a schematic diagram of a system for driving a stepper motor in the capsule for angle-controlled laser irradiation, including a flowchart of the algorithm. The stepper motor was powered by a DC power supply (GPE-3323; GW Instek) and controlled by the motor driver (AMIS-30543; Pololu) via a microcontroller (STM32F0DISCOVERY; STMicroelectronics) connected to UART bridge of a computer (CP210x; Silicon Labs). The driving algorithm was developed using the Keil MDK (ARM) development toolchain powered by the microcontroller. Visual Studio (Microsoft) has created a graphical user interface to set the duration, speed, and scan angle. The motor driver increased the angular resolution from 18° to 0.07° by dividing the step angle into 256 substeps.

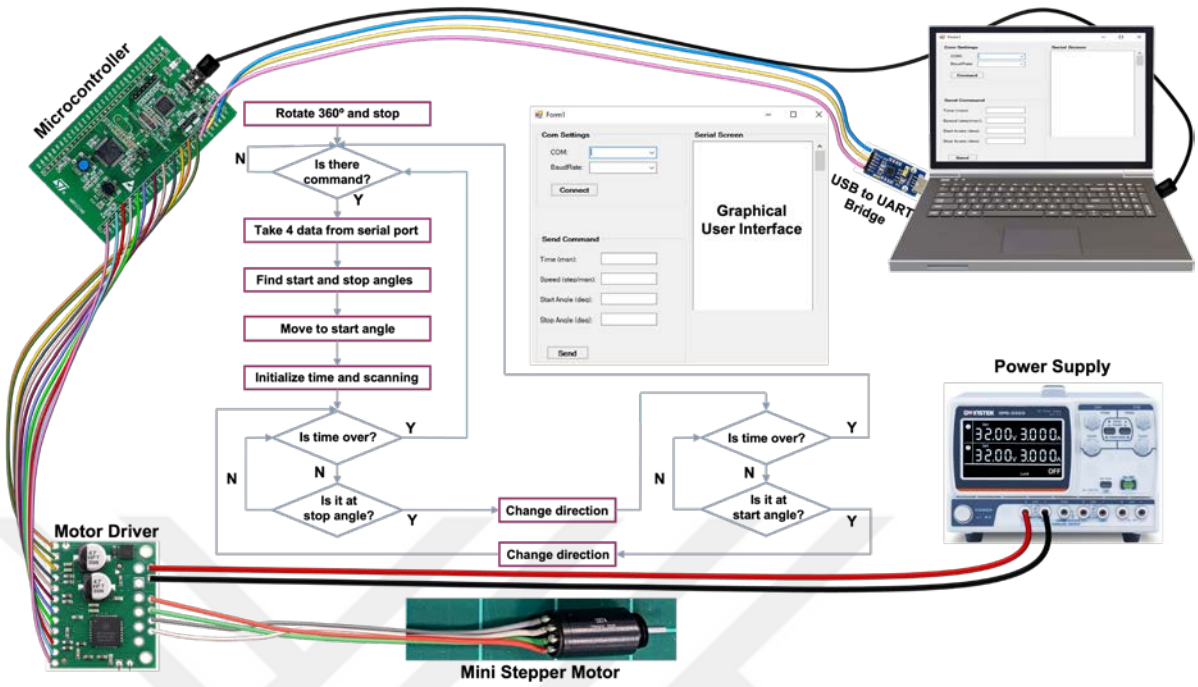


Figure 34: Schematic diagram of stepper motor driving system, including a power supply, a motor driver, a microcontroller, and an USB to UART bridge, with the flowchart of the driving algorithm. The graphical user interface facilitates to define time, speed and scanning angle.

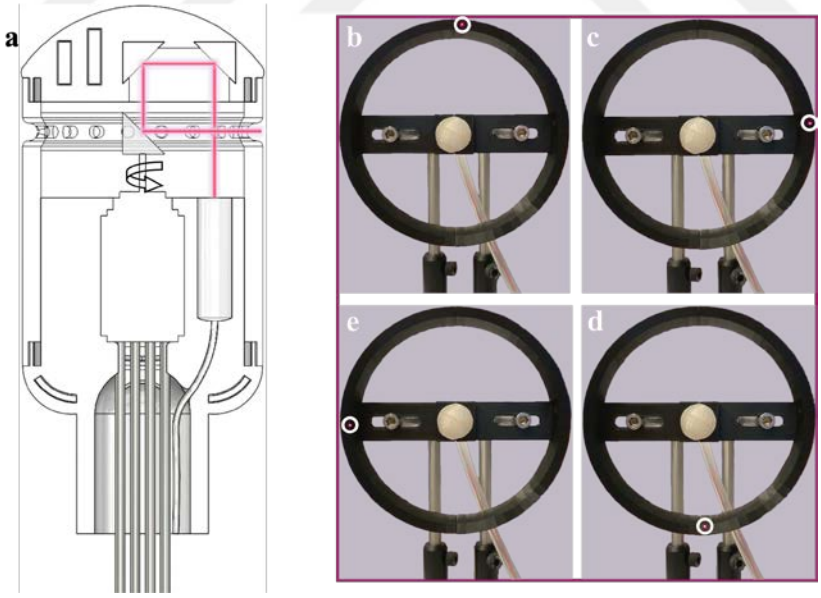


Figure 35: (a) Schematic drawing of the aligned and directed laser beam to the slot of the capsule #2. A sequence of frames representing the circumferential laser beam motion at which the visible diode laser at 660 nm (seen as red dot on the black ring) was used as an aiming beam to track the stepper motor's rotation. **(b)**, **(c)**, **(d)**, and **(e)** show the laser beam position at 0°, 90°, 180°, and 270°, respectively.

Figure 35a shows a schematic drawing of the laser beam aligned and directed into the slot of capsule #2. The rotational motion of the stepper motor in the capsule was monitored on the black

ring with a visible diode laser at 660 nm used as the aiming beam. Figures 35b, 35c, 35d and 35e show the laser beam position at 0°, 90°, 180° and 270°, respectively.

2.4.4. Assembly of the Endoscopy System

Figure 36 shows a schematic photograph of the experimental setup containing the endoscopy system using capsule #2. The ex vivo sheep esophagus was used to evaluate the capsule's performance in the experiment. In this context, laser beam scanning was performed at 65°, 150°, and 360° angles with multiple scans (1, 2, 3, and 5 times) for each of the 0.5, 1.0, and 2.0 mm/s laser scanning speeds. In addition, different multiple scans were applied in a circumferential (360°) scanning at 120° intervals.

Tissue samples were treated according to the protocol (see Appendix 7.1) before and after laser irradiation except for histology process.

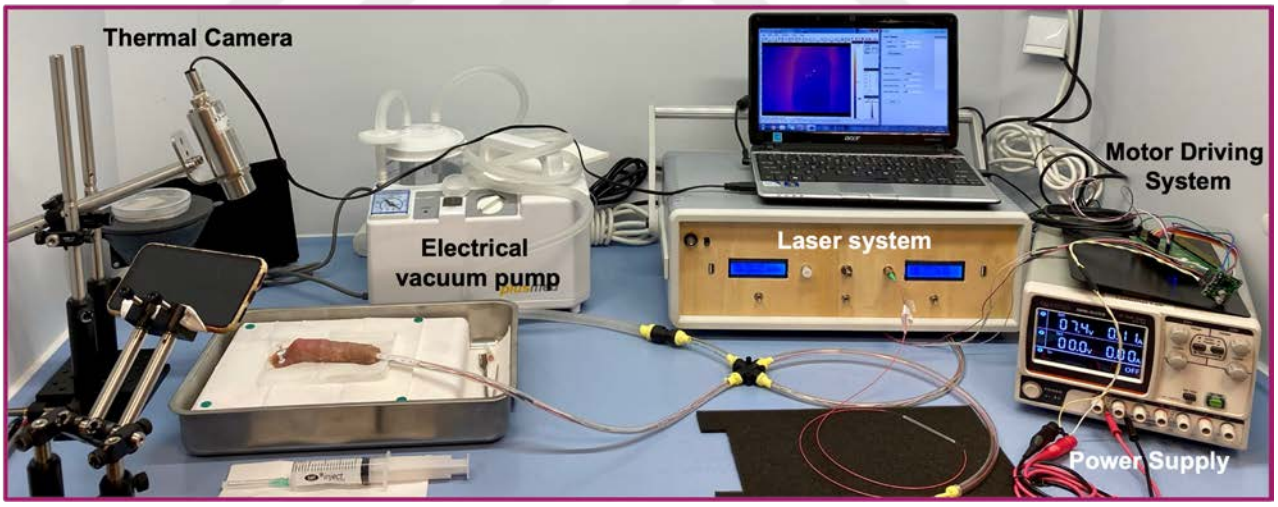


Figure 36: A photograph of the endoscopy system involved in the experimental setup for ex vivo sheep esophagus model.

Table 8 shows the specifications of developed endoscopy system with capsule #2.

Table 8: Specification of endoscopy system with capsule #2.

System Specifications	
Visible Laser Wavelength	660 nm

IR Laser Wavelength	1502.83 nm
IR Laser Beam Diameter	~0.4 mm
IR Laser Maximum Output Power	410 mW
Optical Insertion Loss (through the hole)	16%
Optical Insertion Loss (through the PMMA)	40%
Step Angle of Motor	0.07 ^{o}
Speed Range of Motor	0.1 mm/s – 200 mm/s
Vacuum Range of Capsule	-280 mmHg to -700 mmHg

3. RESULTS

3.1.Guiding Map and Validation

The guiding map of the estimated damaged area (indicated by a colored bar) as a function of surface scanning speed and laser irradiance, Figure 37, provides easier reading for the four-module computer simulation algorithm results. The thermally damaged area was calculated for different scanning speeds from 0.5 mm/s to 8 mm/s and various laser irradiances from 7.4 7 W/cm^2 to 61.7 W/cm^2 (calculated based on a fixed beam diameter of 0.9 mm for laser powers between 60 to 500 mW). The findings showed that laser irradiance between 16.4 W/cm^2 and 31.8 W/cm^2 at the slowest scanning speed (i.e., 0.5 mm/s) is optimal for efficient photothermal effect at sufficient depth. The required laser irradiance for 1 mm/s was between 23.2 W/cm^2 and 38.1 W/cm^2. On the other hand, for scan rates greater than 1 mm/s, the estimated thermally damaged area was less than 0.9 mm^2. According to the map, the threshold laser irradiance for effective thermal damage was 7.7 W/cm^2 at 1505 nm, and the maximum damaged area was estimated as 2.514 mm^2 for 61.7 W/cm^2 at 0.5 mm/s.

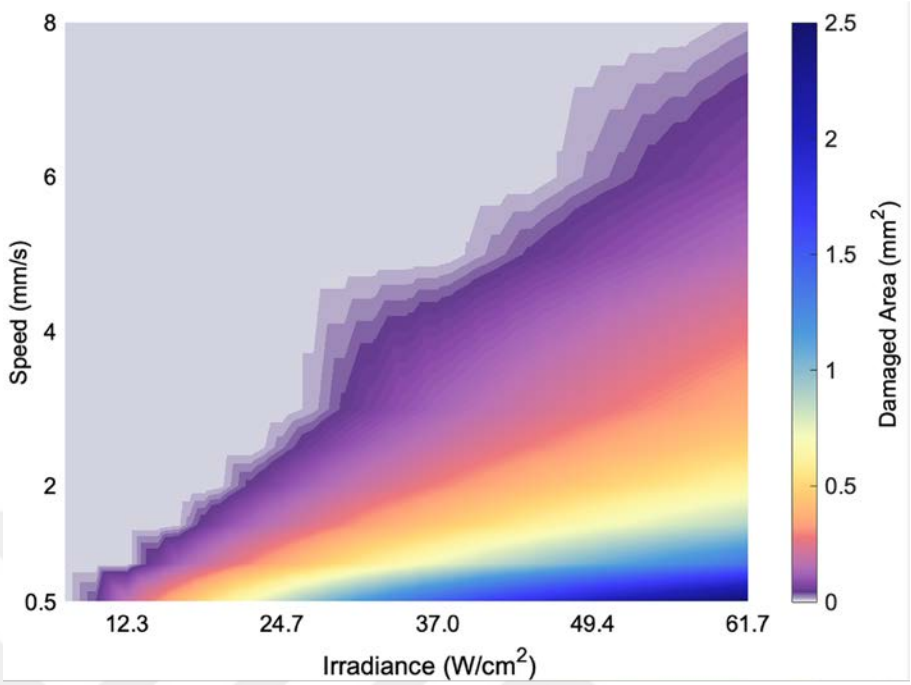


Figure 37: Guiding map as an illustration of the estimated damaged area, by the four-module computer simulation study, as a function of surface scanning speed and laser irradiance.

Figure 38a shows a photograph of the large ex vivo sheep esophagus taken immediately after laser irradiation at seven different laser power settings: 133, 150, 188, 220, 258, 284, and 309 mW at 1 mm/s surface scan. The corresponding laser irradiance is 16.4, 18.5, 23.2, 27.2, 31.9, 35.1 and 38.1 W/cm^2, respectively. Whitening was observed as a thermally induced visual change in the mucosal surface with increasing thickness as a function of applied laser irradiance at a constant surface scanning rate. Conversely, increased scanning rates at fixed laser irradiance followed the relative decrease in whitening thickness. Figures 38b and 38c show brightfield and darkfield microscopy images of the H&E-stained ex vivo sample acquired from the region of interest. The dashed pink line indicates the section side for histology analysis. The images were created by combining 27 consecutive images taken at 4X magnification for each. In brightfield microscopy images, the main difference between the coagulated and non-coagulated tissue regions was the hue expressed separately by the esophageal layers. The epithelial layer has gained a light pink color with a transparent-blurry appearance due to the loss of cell contours, disruption of intercellular connection integrity, and formation of intracellular spaces. Epithelium dissociation from the basal lamina was observed from 188 mW. Protein degradation in the lamina propria and submucosa layers, which consists predominantly of connective tissue, caused a dark color and homogeneous and opaque appearance due to the high affinity of free amino groups to eosin. Changes observed

in-depth, as is the thickness of the mucosal whitening, were associated with increased laser irradiance at a constant beam diameter and proportionally decreased surface scanning speed.

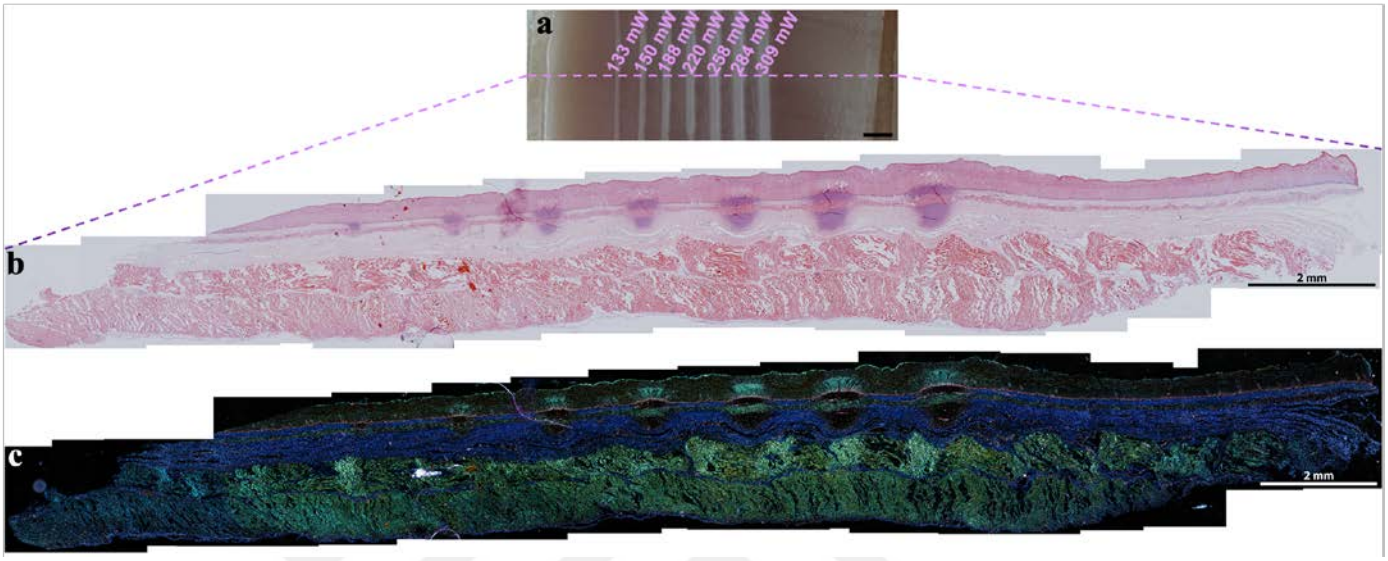


Figure 38: (a) Gross picture of the laser irradiated ex vivo sheep esophagus indicating the mucosal whitening as a visible effect of thermal damage. Scanning speed = 1 mm/s, laser powers = 133, 150, 188, 220, 258, 284, and 309 mW. Scale bar = 2 mm. Images of hematoxylin-and-eosin-stained ex vivo sheep esophagus from the region denoted by the dashed pink line in **(b)** brightfield and **(c)** darkfield microscopy. Consecutively acquired 27 images at ×4 magnification were merged to generate whole sample image.

On the other hand, darkfield microscopy images of the same H&E-stained sample provided more distinctive colors that represent separate tissue layers. These perceived colors were influenced by the stain's original hue and the tissue sample's thickness and density. In this context, the colors observed for different cell structures are red for the cell nucleus, shades of green for the cell membrane and muscle, and blue for the connective tissue. Specifically, areas of coagulated tissue in the lamina propria and submucosa layers appeared black, which could be explained by the tissue's relatively homogeneous and opaque formation. Both brightfield and darkfield microscopy images provided distinctive features for coagulated and non-coagulated tissue regions; however, the boundary between them was not sufficiently defined. For this reason, after the mathematical subtraction of the darkfield microscope images from the brightfield microscope images as shown in Figure 22c, thermally damaged area measurements on the images were successfully obtained.

Figure 39 presents a reconstructed version of the guide map with experimental validation results on an ex vivo sheep esophagus model for an acceptable laser irradiance range of 16.4 to 38.1 W/cm^2 and surface scanning speeds of 0.5, 1.0, 1.5, and 2.0 mm/s. We compared the results of the simulation study and the experimental study from the reconstructed map in terms of structural

similarity index measure (SSIM) [112] and mean squared error (MSE) [113]. As shown in Figure 40, the results indicate significant agreement; 0.94 for SSIM and 153.18 for MSE.

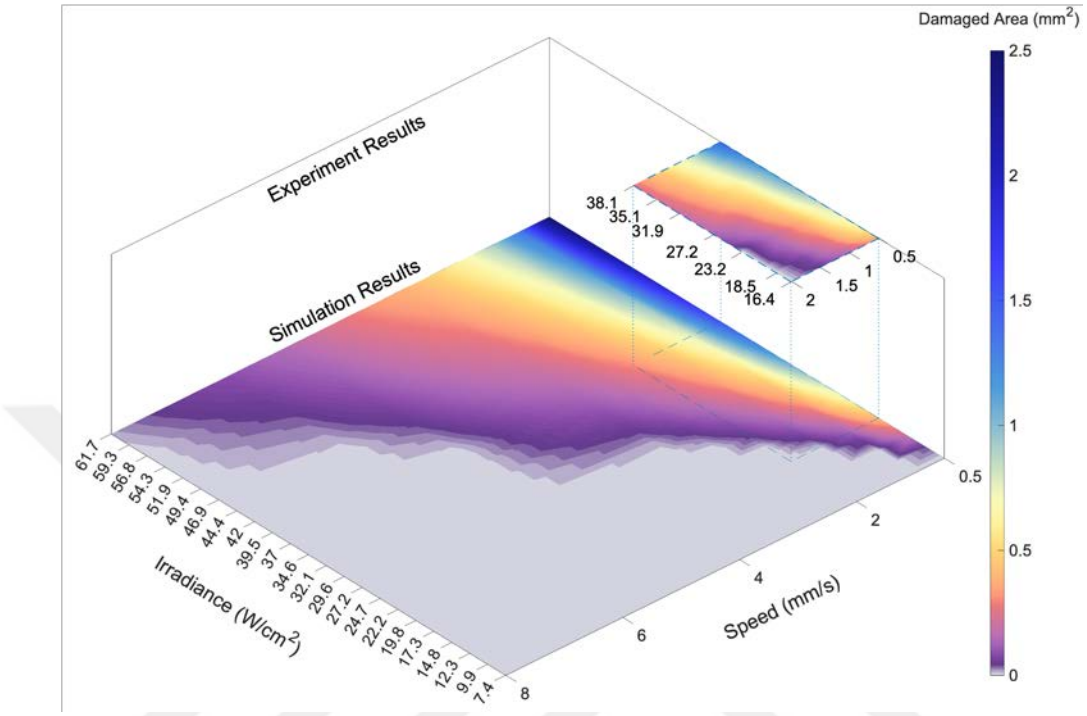


Figure 39: Reconstructed guiding map, including the results of the validation study on ex vivo sheep esophagus for an appropriate irradiance and scanning speed range provided by the restricted resources in experimental studies. Interpolation was used to create a non-discrete appearance.



Figure 40: Comparison of the results of simulation and experimental studies in terms of structural similarity index measure (SSIM) = 0.94, mean squared error (MSE) = 153.18.

In addition, we validated the map by directly comparing simulation and experimental results on fluence (i.e., energy density, J/cm^2). Figure 41a shows the logic of calculating the laser fluence to which the tissue is exposed during laser scanning. In this context, energy density is directly proportional to laser power (P) and inversely proportional to beam diameter (R) and surface scanning speed (ϑ). The plot of the damaged area as a function of laser fluence in Figure 41b shows a consistent correlation between simulation (green dashed line) and experimental results (solid red line), although fluctuation ranges from 25 to 40 J/cm^2. According to the graph, the onset of thermal injury was confirmed as 10 J/cm^2. In addition, there is an increase in the relative standard deviation (pink region) due to mechanical damage caused by high laser energy at an energy density of 60 J/cm^2 and above. This tear-like mechanical separation (I, SM) at the intersection of the submucosa

and muscle layers is exemplified by block-face scanning electron microscopy (Sigma 500l Zeiss) images obtained at 1500X magnification from thermally-effected (coagulated) (I) and control (II) regions (Figure 42) to characterize the photothermal effect.

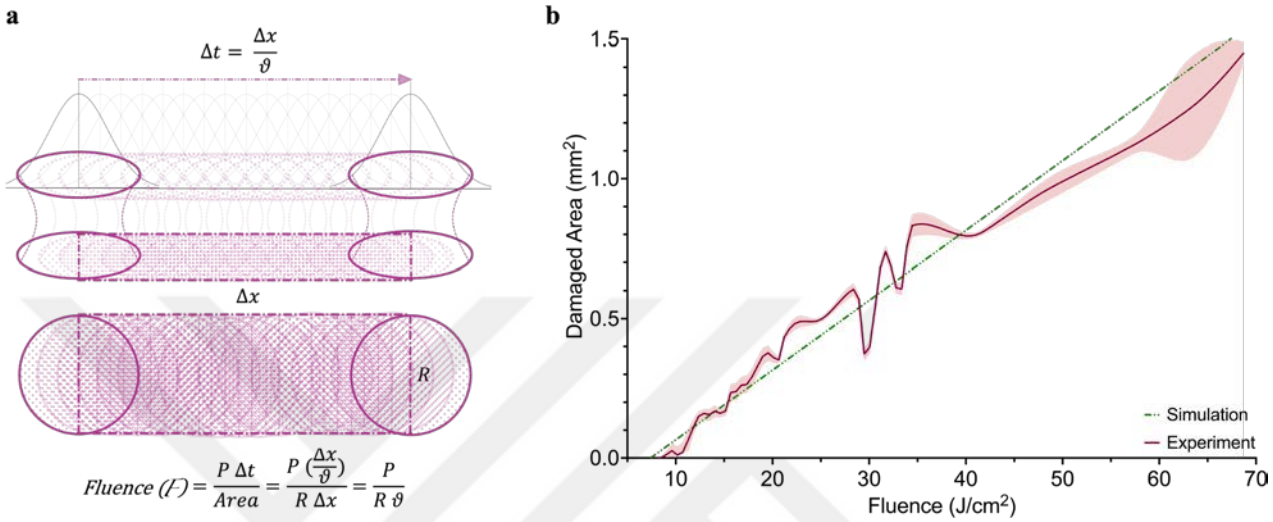


Figure 41: (a) The logic behind the calculation of fluence (i.e., energy density) to which the tissue is subjected during the laser surface scanning. Fluence exposed for a distance is inversely proportional to surface scanning speed (!) and beam diameter (*R*) directly proportional to laser power (*P*). **(b)** A graph of the damaged area as a function of fluence that compares the simulation (green dashed line) and experiment findings (dark red line) with the standard deviation (pink region) directly.

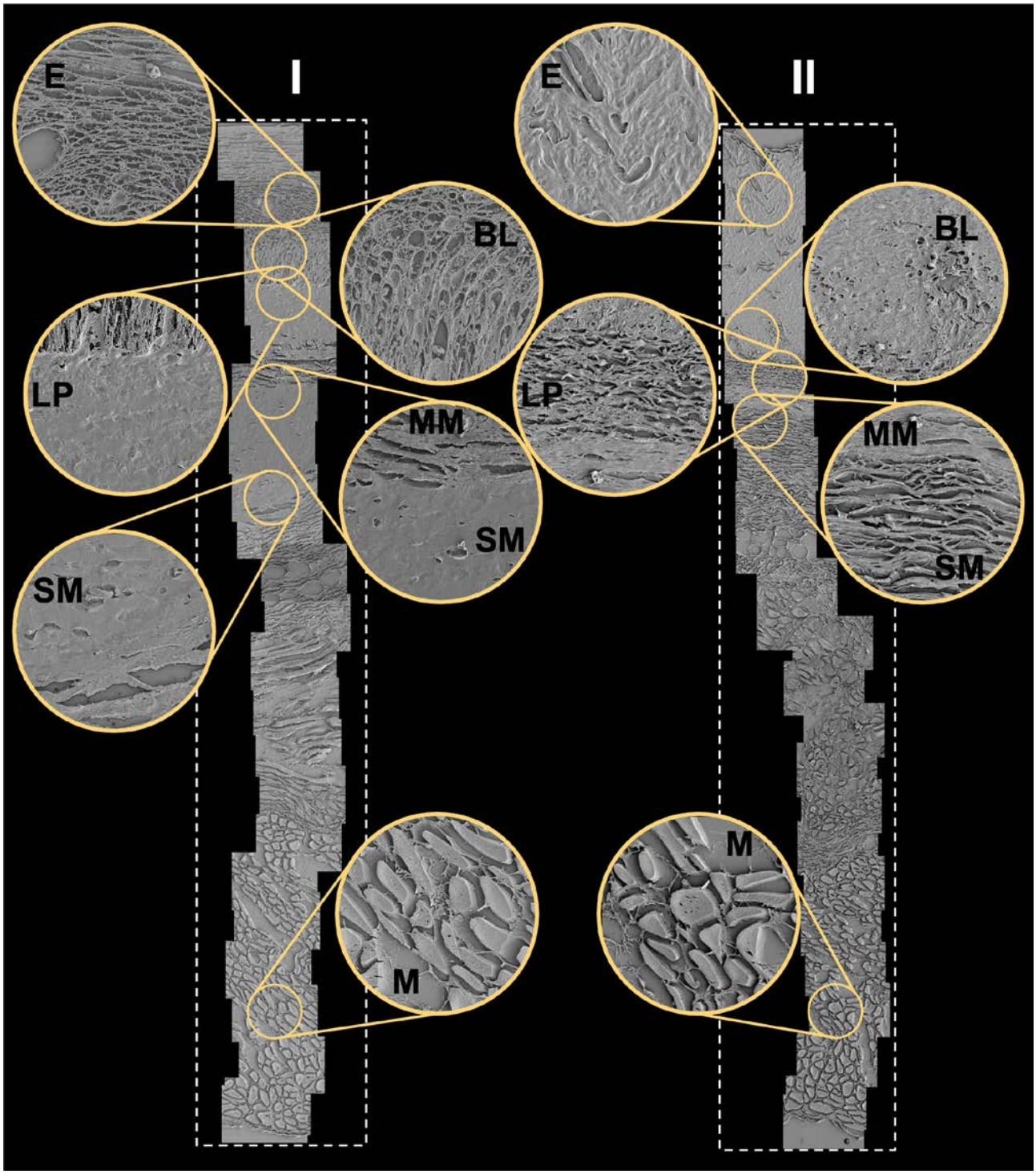


Figure 42: Images of block-face scanning electron microscopy from thermally affected (I) and control (nonaffected) (II) tissue sections at ×1500 magnification. E: epithelium, BL: basal lamina, LP: lamina propria, MM: muscularis mucosa, SM: submucosa, and M: muscle.

Enlarged images in circles highlight epithelial (E), basal lamina (BL), lamina propria (LP), muscularis mucosa (MM), submucosa (SM), and muscle (M) layers and indicate changes in coagulated sections compared to the control tissue at the cellular level. In the epithelial layer, the

laser-induced thermal effect disrupted cell integrity and loss of chromatin structure or cell nucleus, resulting in a filamentous structure. Similar changes were observed in the basal lamina but milder than in the epithelium. Despite this, a noticeable difference was noticed in the shape of the cells, which transformed from a cubic appearance to a vertically elongated one. The lamina propria and submucosa also showed drastic changes from fibrillar, less dense, and viscous structures to homogeneous, dense, and opaque structures. Separating muscle fibers creates internal cavities in the muscular mucosa, resulting in thickening post-coagulation. In addition, heat-induced mechanical damage was observed at the intersection of the submucosa and muscle layers.

3.2. Capsule #1: Well-Confined Photo-Thermal Esophageal Mucosa Ablation

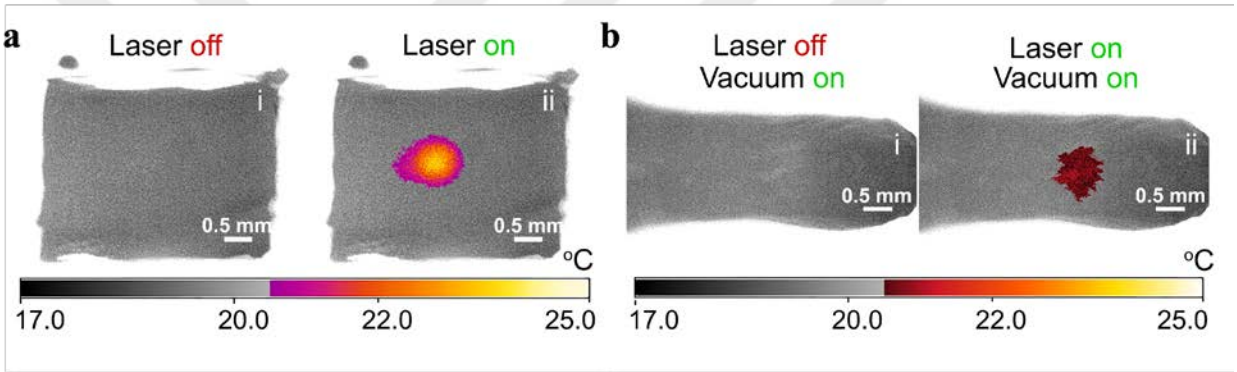


Figure 43: Representative thermal images of the esophagus acquired from the muscle surface of **(a)** the control group and **(b)** the capsule #1- treated group before (i) and during (ii) laser irradiation to quantify the laser-induced thermal effect in deep tissue layers.

Figure 43 shows representative thermal images of the esophagus taken from the muscle surface of ex vivo porcine esophagus before (i) and during (ii) laser irradiation to quantify the laserinduced thermal effect in deep tissue layers. Direct collimation of laser irradiation caused a temperature change of >7°C in the muscle layer (Figure 43a). Conversely, capsule #1 produced only half of this temperature change in deep tissue at the same laser energy with the vacuum turned on (Figure 43b), demonstrating the effectiveness of the negative pressure approach to limit the depth of thermal effect through stretching the mucosal layer into the recessed area.

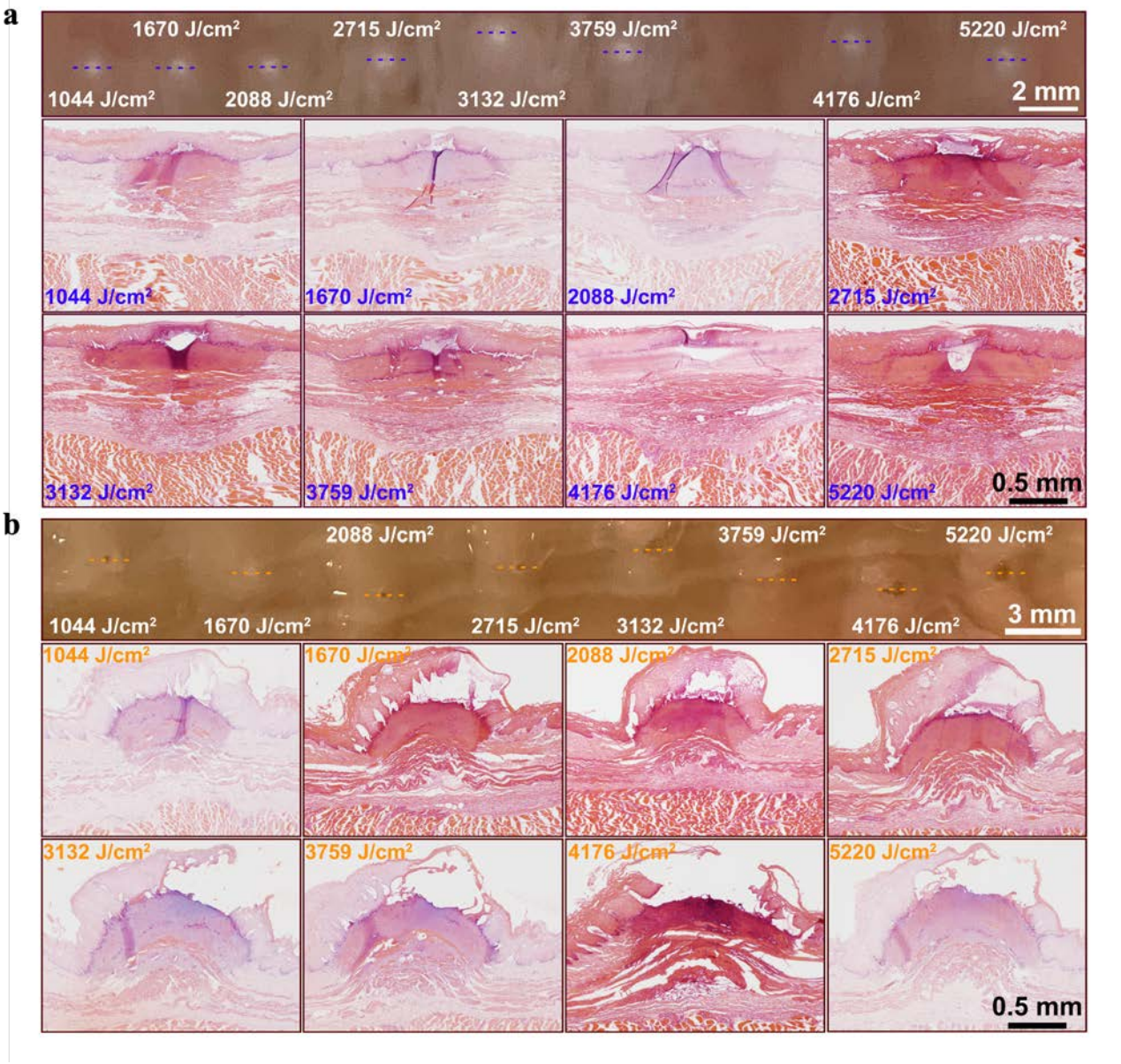


Figure 44: The photographs of ex vivo porcine esophagus representing gross anatomy after laser irradiation of **(a)** the control and the **(b)** capsule #1-treated group. Corresponding cross-sectional hematoxylin-andeosin-stained tissue sections with increasing energy densities from 1044 to 5220 J/cm^2 at 208.8 W/ cm^2 laser irradiance for a duration of 5-25 s.

Figure 44 shows gross anatomy images and corresponding cross-sectional H&E stained tissue sections after 5-25 s laser irradiation in the control (a) and capsule #1 (b) groups. The energy density (fluence) increased from 1044 to 5220 J/cm^2 at 208.8 W/cm^2 laser irradiance. Histology samples exhibited condensed or absent cell nuclei and intercellular voids in the epithelium layer with a subepithelial cleft in the basal lamina. As expected, homogenization of collagen was observed due to protein denaturation in the lamina propria (LP), an indicator of thermal damage. Even though similar alterations were noticed in the histology analysis of both groups, the extent and the severity of laser-induced thermal effect differed. The graphs in Figure 45 summarize all data from the

comparison study. Figures 45a and 45b show that changes in depth and width of laser-induced thermal damage are not statistically significant (ANOVA: Single factor) regardless of energy density, as the slot of capsule #1 defines the volume of stretched tissue.

On the other hand, when the laser beam was collimated to the esophageal tissue, the area of thermally injured tissue increased as a function of energy density. The graph in Figure 45c compares laser-induced thermal damage area at the layer level. Direct laser irradiation in the control group caused thermal damage to the submucosa layer (SM) by penetrating the lamina propria (LP) and muscularis mucosa (MM) layers at all energy densities. The increased laser fluence (energy density) expanded the submucosa's damaged area, affecting the esophagus's total damaged area. Conversely, capsule #1 produced the thermal effect independent of laser fluence, limiting the thermal effect to the mucosa (LP & MM) and superficial submucosa.

Figure 46 shows an example of histology results from another comparison study performed on the porcine stomach's fundus region that mimics the esophagus's unhealthy state (e.g., Barrett's Esophagus). Although similar laser energy densities were reproduced using precisely the same irradiation times, the resulting histology samples could not be thoroughly analyzed due to the excess fat layer that prevents residual damage from the laser-induced thermal effect. However, several measurements from samples with relatively fewer fat layers matched the total damaged area in the case of a healthy esophageal sample (i.e., the control group).

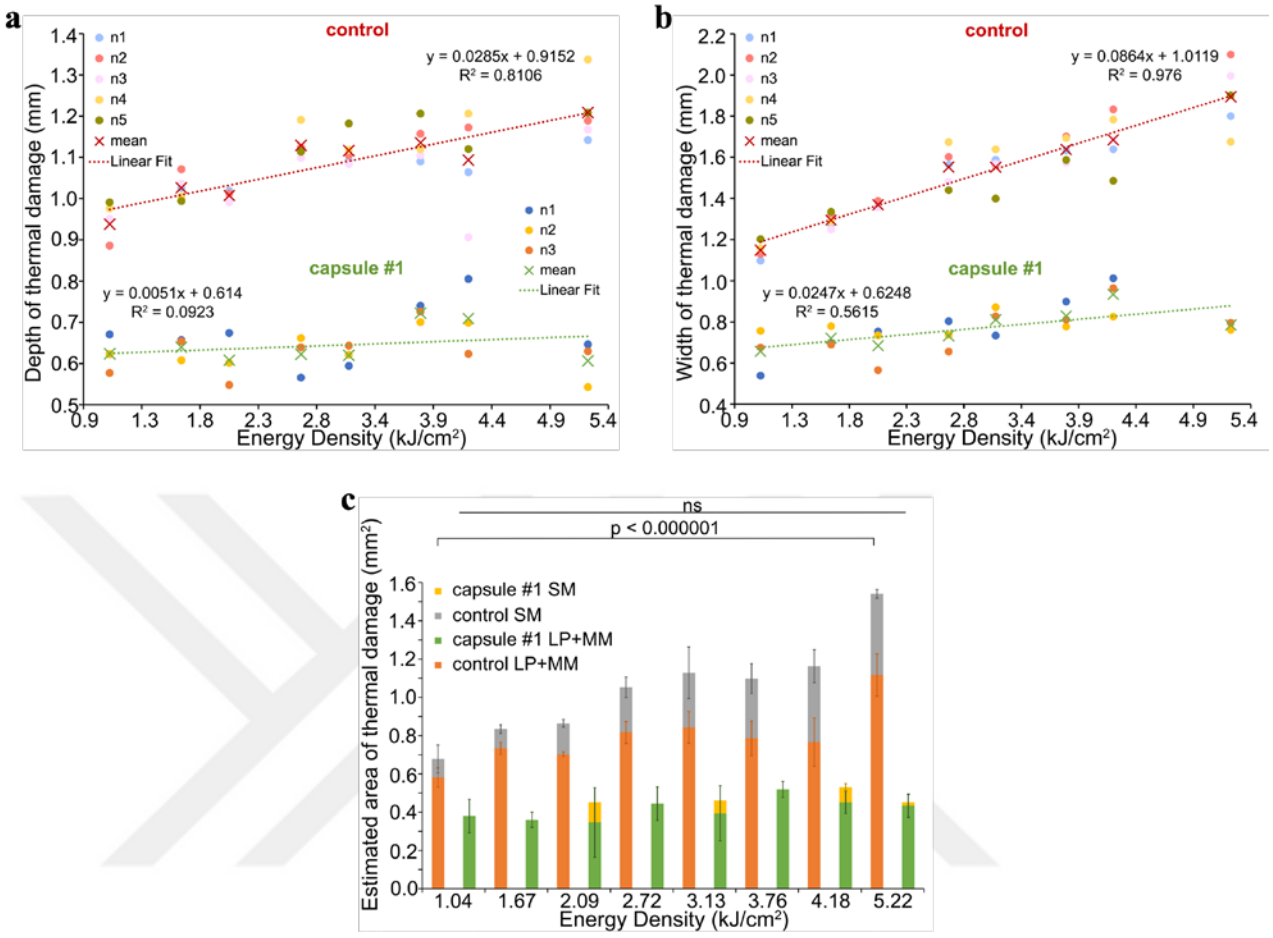


Figure 45: Summary of the comparison study with the plots of **(a)** depth and **(b)** width of thermal damage, and a chart of estimated damaged area in the layers: lamina propria (LM), muscularis mucosa (MM), and submucosa (SM).

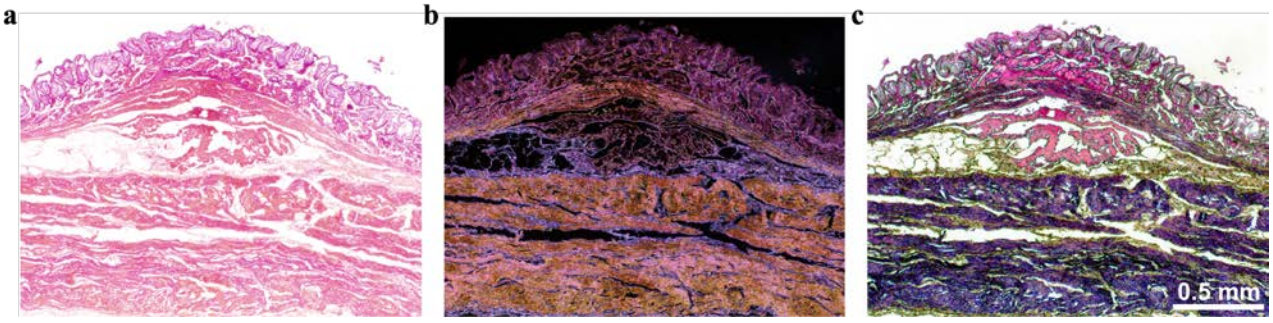


Figure 46: An example of histology results obtained from fundus region of the porcine stomach after laser irradiation employed by capsule #1. **(a)** Brightfield, **(b)** darkfield and **(c)** subtracted microscopy images.

3.3. Capsule 2: Angle-Controlled Photo-Thermal Esophageal Mucosa Ablation

The last experimental study evaluating the performance of capsule #2 at different scan rates and scan angles was performed in an ex vivo sheep esophagus model. In this context, the rotational motion of the laser beam was defined at 65°, 150°, and 360° angles with multiple scan numbers (1,

2, 3, 5 times, as shown in Figure 47) for each laser scanning speed. 0.5, 1.0, and 2.0 mm/s at an average laser power of 295 mW.

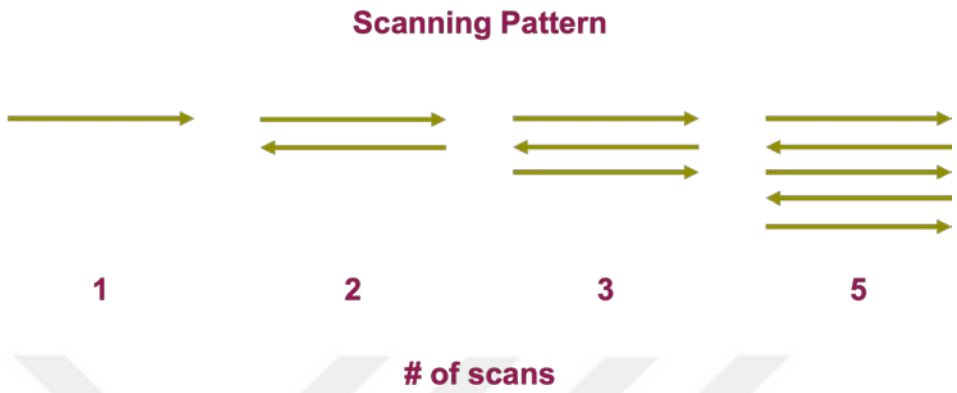


Figure 47: A representative drawing defining the scanning pattern with multiple number of scans.

Figure 48 shows photographs of the ex vivo sheep esophagus representing the gross anatomy after laser scanning with capsule #2 at scanning speeds of 0.5, 1.0, and 2.0 mm/s, respectively. Colored dashed lines highlight the angles provided by the rotational motion of the stepper motor in the developed capsule #2: yellow for 65°, green for 150°, and pink for 360°. Different laser scan repetitions – 1, 2, 3, 5 – were used for each angle and each scan speed. Mucosal whitening was followed as a visual change of thermal injury. Although the whitening thickness was proportional to the decreased scan rate and increased scan number (scan repetitions), it was unrelated to the scan angles applied.

In order to test the control capability of the motor driver system via the created graphical user interface (GUI), a different scanning model than the one shown in Figure 47 was executed. This model included three different scan numbers (1, 3, 5) in a single circumferential (360°) motion at 120° intervals. This pattern was repeated for scanning speeds of 0.5, 1.0, and 2.0 mm/s (Figure 49).

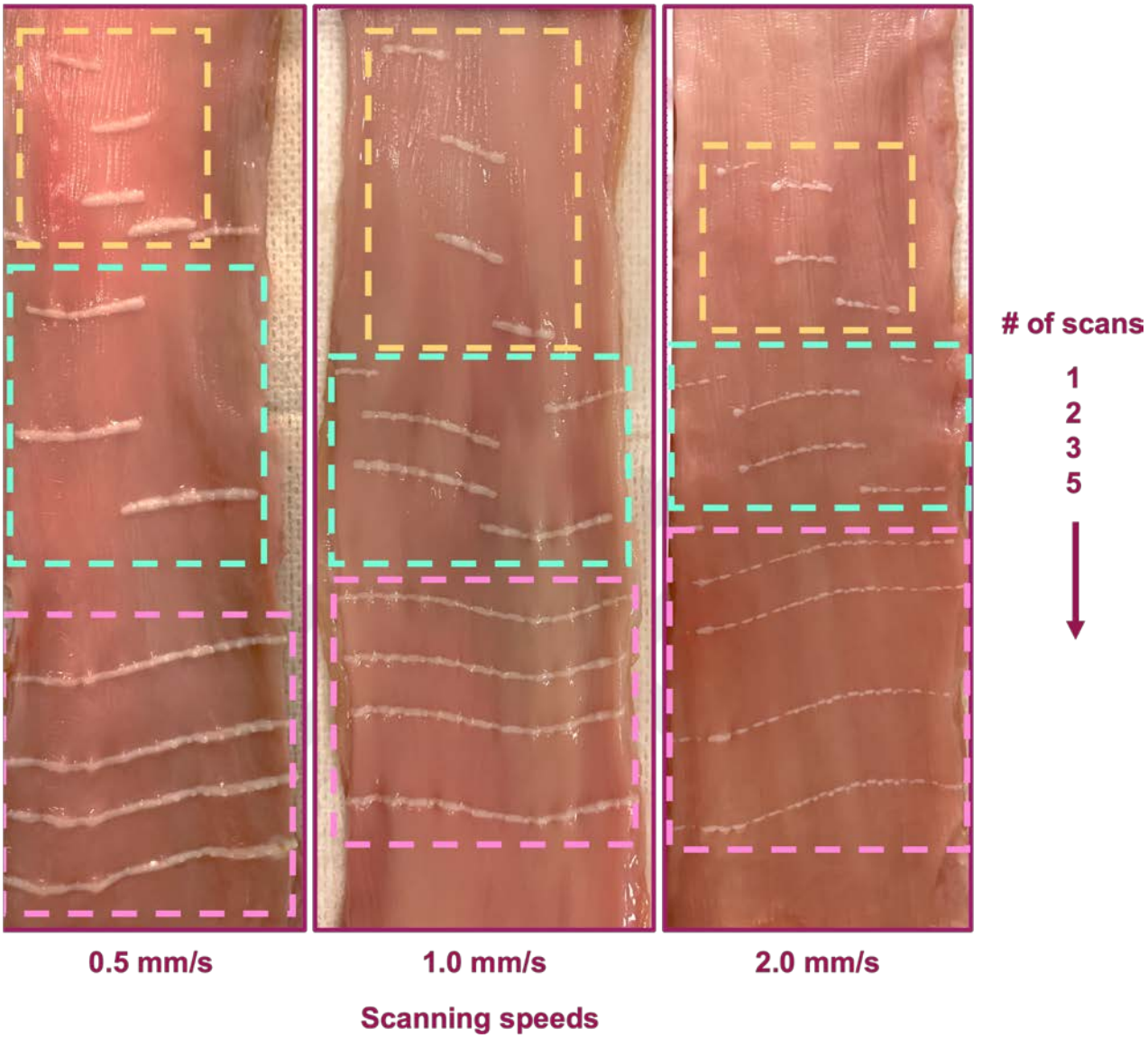


Figure 48: The photographs of ex vivo sheep esophagus representing gross anatomy after laser scanning with capsule #2 at scanning speeds of 0.5, 1.0 and 2.0 mm/s, respectively. Dashed rectangles indicate the angles of rotational movement: 65^{o} (yellow), 150^{o} (green) and 360^{o} (pink), with multiple number of scans (1, 2, 3, 5) for each angle.

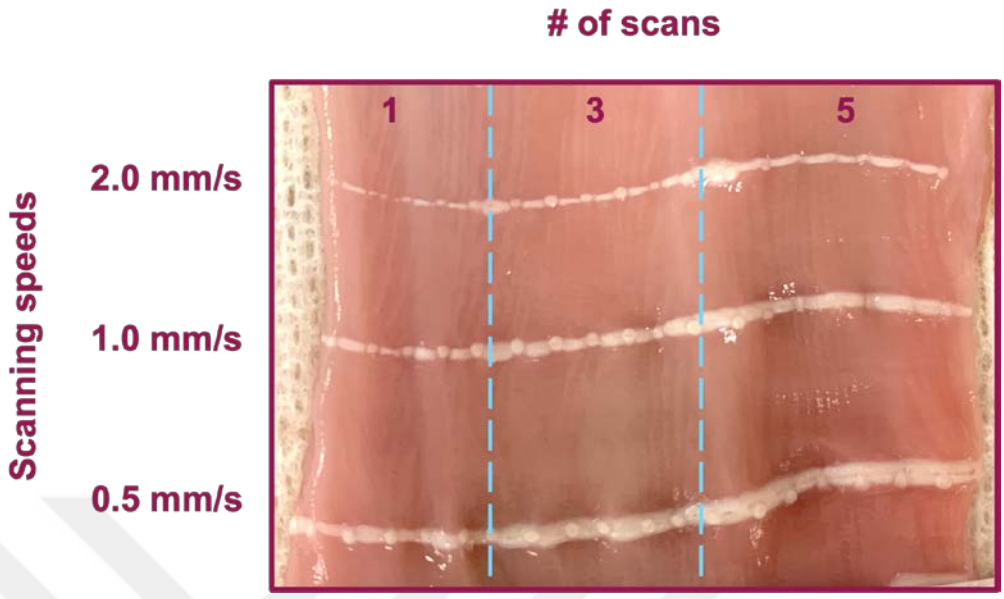


Figure 49: A photograph of ex vivo sheep esophagus representing gross anatomy after implementation of a specific laser scanning pattern including different number of scans (1, 3, 5) in a single circumferential laser irradiation with intervals of 120^{o} at scanning speeds of 0.5, 1.0, 2.0 mm/s.

4. DISCUSSION

Laser-induced thermal therapy has been employed in gastroenterology interventions since the late 1970s. Initially, endoscopic implementation of the laser-induced thermal method mainly focused on hemostasis, management of arteriovenous malformations, and palliation of advanced, inoperable gastrointestinal malignancies. Various lasers have been used primarily for these purposes, including argon laser at 488 nm – 514 nm, Nd:YAG lasers at 1064 nm and 1320 nm, and KTP laser at 532 nm. The therapy model also critically affects applications of superficial abnormal tissue, such as Barrett's Esophagus treatment. In addition to existing lasers, diode lasers at 805 nm and 940 nm have also been investigated to manage Barrett's Esophagus. Despite its reputation in hemostasis studies, the use of laser-induced thermal therapy in treating superficial abnormal tissue has declined significantly due to the lack of ideal tools and apparatus. Therefore, despite endoscopic laser-induced thermal therapy efforts, other thermal ablation methods, such as argon plasma coagulation and radiofrequency ablation, have been chosen mainly for this purpose. However, multiple procedures and the need for RFA contact preclude control of therapy depth. On the other hand, non-contact argon plasma coagulation requires an experienced operator to adjust the distance between the probe and the target tissue with sufficient application time. As a result, the uncontrollable treatment depth caused by thermal treatment techniques is the biggest obstacle to

the complete removal of the Barrett's Esophagus without causing adverse conditions such as perforation, stenosis, and bleeding. Therefore, this thesis addresses this challenge in the endoscopic treatment of Barrett's Esophagus.

Laser-induced thermal therapy, although abandoned, has the potential for safe and effective treatment with fewer side effects. Recent advances in optical and laser technologies allow the use of more wavelengths and new apparatus designs to deliver laser energy to the target area. Optimizing therapy parameters such as laser irradiance, laser energy density, and surface scanning rates is particularly critical. Empirical and relative approaches in laser applications may be one of the reasons why they are not preferred to complicate the process. In this context, we developed a four-module numerical model simulating the laser-induced photothermal effect on mucosal tissue to generate a guide map of the damaged area by simplifying the matrix of relevant parameters. This model predicted laser-induced thermal damage as a function of the absorbed energy of photons in the mucosal tissue. For direct comparison with experimental validation studies performed on ex vivo sheep esophagus, estimates are made for the continuous wave laser operated in 1505 nm.

The results showed that the experimental and theoretical data overlap significantly in energy density. However, some essential points regarding the numerical model should be considered for further research. In the simulation model, the tissue's optical, thermal, and kinetic properties were assumed constant, and the effect of increasing temperature was neglected. While this assumption is acceptable in our case, it will limit accurate results in studies with large thermal gradients that cause a phase change in tissue. In addition, heat convection through blood vessels was not included in the heat transfer calculations, as ex vivo tissue did not have a dynamic blood flow. However, heat dissipation by vessels will be critical for more complex tissues in in vivo applications. The effect of the surrounding undamaged tissue on the healing process, such as postmortem degeneration in ex vivo tissue, was also ignored in this study. Furthermore, this model assumed that the entire esophagus is a mucous tissue due to the lack of literature regarding all layers' optical and thermal properties. Besides, the surface temperature results obtained from simulation and experimental studies during laser irradiation could be compared as well as the damaged area.
However, the requirement to position the thermal camera perpendicular to the tissue surface for accurate measurements limited this comparison. The holder on which the GRIN lens was fixed prevented direct viewing of the irradiated area from the thermal camera.

The validation study with ex vivo sheep esophagus showed promising results for controlling the damaged area with appropriate therapy parameter pairs. Nevertheless, a physical delimitation can provide a confined laser-induced thermal effect. In this regard, we have developed an

endoscopy apparatus, capsule #1, apply negative pressure to stretch the mucosal tissue in a recessed area and to deliver laser energy to the target tissue site. As a unique mechanical property, the esophageal mucosa's elasticity allows for stretching. Applying capsule #1 in ex vivo porcine esophagus in this context revealed that the negative pressure approach offers potential for laser energy-independent thermal effect depth. Injury depth, width, area obtained from histological analysis, and temperatures measured from the outer surface of the esophagus (e.g., muscle layer) confirmed the limited thermal effect without affecting deeper tissue layers such as the submucosa and muscularis propria. However, elasticity in Barrett's Esophagus condition may differ due to abnormal tissue composition, which alter from stratified squamous epithelium to metaplastic columnar epithelium. Therefore, another objective in the experimental studies with capsule #1 was to understand the effect of the proposed approach on the fundus region of the pig stomach, which can closely mimic Barrett's Esophagus due to its cellular organization, and to compare the thermally damaged area results with those of the porcine esophagus studies. Although the effectiveness of the negative pressure approach to stretch the gastric mucosal layer towards the recessed region of capsule #1 was confirmed, the extent of the damage could not be fully defined due to the excess fat layer below the muscularis mucosa layer.

After building the endoscopy system at a prototype level for pre-clinical trials and confirming the negative pressure approach with a designed apparatus, we refined the design of the apparatus as a new endoscopy capsule #2 for well-confined photothermal mucosal ablation/coagulation with angle control. Capsule #2 comprises three parts: cap, body, and base, which includes a GRIN lens to transmit the laser beam, a stepper motor for angular control of the rotating laser beam, and three gold-coated right-angle prism mirrors for directing the laser beam. Laser energy meets the target tissue non-contact through the optically transparent body part that connects the head and base parts. Negative pressure was transmitted through the perforated cavity of the body to limit the depth of tissue exposed to the laser to a specific volume. The stepper motor quickly defined the rotation angle at a constant speed. The results of the ex vivo sheep esophagus study successfully demonstrated the ability of capsule #2 to control the rotational motion of the laser beam for different angles, scan speeds, and number of scans. From a design standpoint, matching the capsule's dimensions to the esophagus's size was the main challenge, as its dimensions were determined by its skeleton's electrical and optical components. Although we chose these components as small as possible, the products available on the market limited the options. Therefore, the capsule #2 can be created in various sizes if the components are customized. In addition, the resolution of the 3D printer limited the correct execution of the design, affecting the positions of the components,

especially the prism mirrors. Although the laser beam could be aligned to the cavity, a slight deviation in circumferential rotation was observed. However, this deviation was restricted to the edges of the cavity without affecting the ablation/coagulation of the mucosal tissue. Additionally, a considerable power loss was measured from the surface of body due to the curvature of cavity. Research on ex vivo tissue samples also revealed the need for an appropriate cleaning and closure procedure for repeated capsule #2 use with maximum effectiveness.

Comparing current and preferred treatment techniques, Capsule #2 provides non-contact (i.e., mm scaled distance in the air) and angle-controlled thermal ablation/coagulation with homogeneous laser energy delivery to the tissue surface. In addition, during laser irradiation, negative pressure traps the mucosa layer into the recessed area (slot), helping to prevent unwanted movements caused by external factors. The capability of Capsule #2 sliding on the mucosal lining of the esophagus offers large treatment areas in a single session.

5. CONCLUSION AND FUTURE PERSPECTIVES

Laser-induced thermal therapy, an endoscopic thermal treatment method, can effectively meet the need for superficial treatment in the gastrointestinal tract with minimal side effects. The presented results of the simulation study showed that the guide map could be a valuable tool in optimizing parameters for adequate removal of superficial abnormal tissues such as Barrett's Esophagus. A validation study on ex vivo sheep esophagus at a laser wavelength of 1505 nm confirmed this assumption. The simulation algorithm can be expanded and refined for further studies to become a complementary tool for laser-induced thermal therapy with in vivo models suitable for various laser wavelengths and pulsed operating modes.

Administration of Capsule #1 with ex vivo porcine esophagus proved that the negative pressure approach could confine thermal injury to the mucosa and superficial submucosa and protect the deeper layers of the esophagus. Stretching the target tissue into the recessed slot of the capsule facilitated the limitation of the laser-induced thermal effect independent of the laser energy. The new design of Capsule #2 provided angle-controlled laser mucosal ablation/coagulation. Defining the angle in the rotational motion and setting a constant speed for scanning provides better control of the laser beam. An additional slide mechanism can be placed in the endoscopy system for longitudinal movement of the capsule along the esophagus to achieve a large ablation/coagulation area in a single session. In addition, using the optical infrastructure of the capsule, an advanced imaging method such as optical coherence tomography can be combined with

capsule #2 for simultaneous monitoring. With further in vivo animal studies, including rigorous histological analysis of thermal damage to the esophagus, this design may hold promise for endoscopic laser-induced thermal treatments in clinics.

6. REFERENCES

1. Arnold M, Abnet CC, Neale RE, Vignat J, *et al.* Global Burden of 5 Major Types of Gastrointestinal Cancer. Gastroenterology 2020;159: 335-49.e15.

2. Sung H, Ferlay J, Siegel RL, Laversanne M, *et al.* Global Cancer Statistics 2020: Globocan Estimates of Incidence and Mortality Worldwide for 36 Cancers in 185 Countries. CA Cancer J Clin 2021;71: 209-49.

3. Lynch JP, Rustgi AK. Mechanisms of Gi Malignancies. In: Johnson LR, Ghishan FK, Kaunitz JD, *et al.*, editors. Physiology of the Gastrointestinal Tract. 5 th ed.: Academic Press; 2012. p. 2129-55.

4. Wild CP, Hardie LJ. Reflux, Barrett's Oesophagus and Adenocarcinoma: Burning Questions. Nature Reviews Cancer 2003;3: 676-84.

5. Odemiş B, Çiçek B, Zengin NI, Arhan M, *et al.* Barrett's Esophagus and Endoscopically Assessed Esophagogastric Junction Integrity in 1000 Consecutive Turkish Patients Undergoing Endoscopy: A Prospective Study. Dis Esophagus 2009;22: 649-55.

6. Sahin A, Artas G. Prevalence of Barrett's Esophagus in Eastern Turkey. Acta Medica Mediterranea 2022;38: 19-24.

7. Spechler SJ, Goyal RK. The Columnar-Lined Esophagus, Intestinal Metaplasia, and Norman Barrett. Gastroenterology 1996;110: 614-21.

8. Barrett NR. Chronic Peptic Ulcer of the Oesophagus and 'Oesophagitis'. Br J Surg 1950;38: 175-82.

9. Barrett NR. The Lower Esophagus Lined by Columnar Epithelium. Surgery 1957;41: 881-94.

10. DeMeester SR, DeMeester TR. Columnar Mucosa and Intestinal Metaplasia of the Esophagus: Fifty Years of Controversy. Annals of Surgery 2000;231: 303-21.

11. Tan WK, di Pietro M, Fitzgerald RC. Past, Present and Future of Barrett's Oesophagus. Eur J Surg Oncol 2017;43: 1148-60.

12. Paull A, Trier JS, Dalton MD, Camp RC, *et al.* The Histologic Spectrum of Barrett's Esophagus. N Engl J Med 1976;295: 476-80.

13. Haggitt RC, Tryzelaar J, Ellis FH, Colcher H. Adenocarcinoma Complicating Columnar Epithelium-Lined (Barrett's) Esophagus. Am J Clin Pathol 1978;70: 1-5.

14. Skinner DB, Walther BC, Riddell RH, Schmidt H, *et al.* Barrett's Esophagus. Comparison of Benign and Malignant Cases. Ann Surg 1983;198: 554-65.

15. Reid BJ, Weinstein WM. Barrett's Esophagus and Adenocarcinoma. Annu Rev Med 1987;38: 477-92.

16. Enzinger PC, Mayer RJ. Esophageal Cancer. N Engl J Med 2003;349: 2241-52.

17. Spechler SJ, Souza RF. Barrett's Esophagus. N Engl J Med 2014;371: 836-45.

18. Peters Y, Al-Kaabi A, Shaheen NJ, Chak A, *et al.* Barrett Oesophagus. Nature Reviews Disease Primers 2019;5: 35.

19. Que J, Garman KS, Souza RF, Spechler SJ. Pathogenesis and Cells of Origin of Barrett's Esophagus. Gastroenterology 2019;157: 349-64.e1.

20. Barbera M, Fitzgerald RC. Cellular Origin of Barrett's Metaplasia and Oesophageal Stem Cells. Biochem Soc Trans 2010;38: 370-3.

21. Ergun P, Kipcak S, Bor S. Epigenetic Alterations from Barrett&Rsquo;S Esophagus to Esophageal Adenocarcinoma. International Journal of Molecular Sciences 2023;24: 7817.

22. Garud SS, Keilin S, Cai Q, Willingham FF. Diagnosis and Management of Barrett's Esophagus for the Endoscopist. Therap Adv Gastroenterol 2010;3: 227-38.

23. Anaparthy R, Sharma P. Progression of Barrett Oesophagus: Role of Endoscopic and Histological Predictors. Nature Reviews Gastroenterology & Hepatology 2014;11: 525-34.

24. Singh T, Sanghi V, Thota PN. Current Management of Barrett Esophagus and Esophageal Adenocarcinoma. Cleve Clin J Med 2019;86: 724-32.

25. Spechler SJ, Zeroogian JM, Antonioli DA, Wang HH, *et al.* Prevalence of Metaplasia at the Gastro-Oesophageal Junction. The Lancet 1994;344: 1533-36.

26. Sharma P, Morales T, Sampliner R. Short Segment Barrett’s Esophagus—the Need for Standardization of the Definition and of Endoscopic Criteria. The American Journal of Gastroenterology 1998;93: 1033-36.

27. Sharma P, Dent J, Armstrong D, Bergman JJ, *et al.* The Development and Validation of an Endoscopic Grading System for Barrett's Esophagus: The Prague C & M Criteria. Gastroenterology 2006;131: 1392-9.

28. Conteduca V, Sansonno D, Ingravallo G, Marangi S, *et al.* Barrett's Esophagus and Esophageal Cancer: An Overview. Int J Oncol 2012;41: 414-24.

29. Fiocca R, Mastracci L, Milione M, Parente P, *et al.* Microscopic Esophagitis and Barrett's Esophagus: The Histology Report. Dig Liver Dis 2011;43 Suppl 4: S319-30.

30. Mannath J, Ragunath K. Role of Endoscopy in Early Oesophageal Cancer. Nat Rev Gastroenterol Hepatol 2016;13: 720-30.

31. Chung CS, Wang HP. Screening for Precancerous Lesions of Upper Gastrointestinal Tract: From the Endoscopists' Viewpoint. Gastroenterol Res Pract 2013;2013: 681439.

32. Steele D, Baig KKK, Peter S. Evolving Screening and Surveillance Techniques for Barrett's Esophagus. World J Gastroenterol 2019;25: 2045-57.

33. Martinucci I, de Bortoli N, Russo S, Bertani L, *et al.* Barrett's Esophagus in 2016: From Pathophysiology to Treatment. World J Gastrointest Pharmacol Ther 2016;7: 190-206.

34. De Palma GD. Management Strategies of Barrett's Esophagus. World J Gastroenterol 2012;18: 6216-25.

35. From https://www.telegraph.co.uk/science/2016/10/16/elderly-put-at-risk-by-needlessmedication-study-finds/, Retrieved 12 June 2023.

36. From https://www.mayoclinic.org/diseases-conditions/eosinophilicesophagitis/multimedia/eosinophilic-esophagitis/img-20007963, Retrieved 12 June 2023.

37. From https://ctsurgery.weillcornell.org/surgical-services/thoracic-surgery/surgeryesophageal-cancer, Retrieved 12 June 2023.

38. Kähler G. Endoscopic Resection Methods. In: Kähler G, Götz M, Senninger N, editors. Therapeutic Endoscopy in the Gastrointestinal Tract. 1th ed. Cham: Springer International Publishing; 2018. p. 1-24.

39. Rouphael C, Anil Kumar M, Sanaka MR, Thota PN. Indications, Contraindications and Limitations of Endoscopic Therapy for Barrett's Esophagus and Early Esophageal Adenocarcinoma. Therap Adv Gastroenterol 2020;13: 1756284820924209.

40. Ryu CB, Chen YK. Endoscopic Therapy for Gastric Neoplasms. Gastroenterology and Hepatology; 2015, 425-47. https://clinicalgate.com/endoscopic-therapy-for-gastricneoplasms/#s0170.

41. Sampliner RE, Hixson LJ, Fennerty MB, Garewal HS. Regression of Barrett's Esophagus by Laser Ablation in an Anacid Environment. Digestive Diseases and Sciences 1993;38: 365-68.

42. Muthusamy VR, Sharma P. Multipolar Electrocoagulation (Mpec): An Early, Widely Available Technique. In: Sampliner RE, editors. Endoscopic Therapy for Barrett's Esophagus. 1th ed. Totowa, NJ: Humana Press; 2009. p. 91-105.

43. Sampliner RE. Multipolar Electrocoagulation. Gastrointest Endosc Clin N Am 2003;13: 449-55, vi.

44. Krahn J, Eickhoff A. Endoscopic Recanalization Techniques. In: Kähler G, Götz M, Senninger N, editors. Therapeutic Endoscopy in the Gastrointestinal Tract. 1th ed. Cham: Springer International Publishing; 2018. p. 25-47.

45. Brunetaud JM, Maunoury V, Cochelard D. Lasers in Digestive Endoscopy. Journal of Biomedical Optics 1997;2: 42-52.

46. Barham CP, Jones RL, Biddlestone LR, Hardwick RH, *et al.* Photothermal Laser Ablation of Barrett's Oesophagus: Endoscopic and Histological Evidence of Squamous ReEpithelialisation. Gut 1997;41: 281-4.

47. Salo JA, Salminen JT, Kiviluoto TA, Nemlander AT, *et al.* Treatment of Barrett's Esophagus by Endoscopic Laser Ablation and Antireflux Surgery. Ann Surg 1998;227: 40-4.

48. Khulusi S, Krasner N. Laser Treatment in Gastroenterology. In: Berlien HP, Müller GJ, editors. Applied Laser Medicine. 1th ed. Germany: Springer Berlin Heidelberg; 2003. p. 42741.

49. Weston AP. Use of Lasers in Barrett's Esophagus. Gastrointest Endosc Clin N Am 2003;13: 467-81.

50. Polese L, Angriman I, Scarpa M, Pagano D, *et al.* Diode Laser Treatment of Barrett's Esophagus: Long-Term Results. Lasers Med Sci 2011;26: 223-8.

51. Kallam A, Alsop BR, Sharma P. Limitations of Endoscopic Ablation in Barrett's Esophagus. Expert Rev Gastroenterol Hepatol 2015;9: 487-96.

52. Watson TJ. Endoscopic Therapies for Barrett's Neoplasia. J Thorac Dis 2014;6 Suppl 3: S298-308.

53. Chang KJ. Endoscopic Foregut Surgery and Interventions: The Future Is Now. The State-ofthe-Art and My Personal Journey. World J Gastroenterol 2019;25: 1-41.

54. From https://www.hcmarbella.com/de/radiofrequency-ablation-technique-for-barrettsesophagus-or-halo/, Retrieved 12 June 2023.

55. Shaheen NJ, Sharma P, Overholt BF, Wolfsen HC, *et al.* Radiofrequency Ablation in Barrett's Esophagus with Dysplasia. N Engl J Med 2009;360: 2277-88.

56. Luigiano C, Iabichino G, Eusebi LH, Arena M, *et al.* Outcomes of Radiofrequency Ablation for Dysplastic Barrett's Esophagus: A Comprehensive Review. Gastroenterol Res Pract 2016;2016: 4249510.

57. Lovat LB, Bown SG. Lasers in Gastroenterology. World J Gastroenterol 2001;7: 317-23.

58. Barr H, Stone N, Rembacken B. Endoscopic Therapy for Barrett's Oesophagus. Gut 2005;54: 875-84.

59. Odze RD, Lauwers GY. Histopathology of Barrett's Esophagus after Ablation and Endoscopic Mucosal Resection Therapy. Endoscopy 2008;40: 1008-15.

60. Pennathur A, Gibson MK, Jobe BA, Luketich JD. Oesophageal Carcinoma. Lancet 2013;381: 400-12.

61. Bowers SP, Mattar SG, Waring PJ, Galloway K, *et al.* Ktp Laser Ablation of Barrett's Esophagus after Anti-Reflux Surgery Results in Long-Term Loss of Intestinal Metaplasia. Potassium-Titanyl-Phosphate. Surg Endosc 2003;17: 49-54.

62. Fleischer D. Endoscopic Laser Therapy for Gastrointestinal Disease. Arch Intern Med 1984;144: 1225-30.

63. Hunter JG. Endoscopic Laser Applications in the Gastrointestinal Tract. Surg Clin North Am 1989;69: 1147-66.

64. Swain CP. Laser Therapy for Gastrointestinal Bleeding. Gastrointest Endosc Clin N Am 1997;7: 611-39.

65. Yammine S, Jabbour E, El Toum S, Cassia A. Histological Study of Induced Incisions on Rabbits' Tongues with Three Diode Lasers with Different Wavelengths in Continuous Mode. Scientifica (Cairo) 2018;2018: 2691942.

66. Polese L, La Raja C, Fasolato S, Frigo AC, *et al.* Endoscopic Diode Laser Therapy for Gastric Hyperplastic Polyps in Cirrhotic Patients. Lasers Med Sci 2021;36: 975-79.

67. Schwesinger WH. Laser Treatment of Esophageal and Gastric Lesions. Surg Clin North Am 1992;72: 581-95.

68. Fleischer D, Kessler F. Endoscopic Nd:Yag Laser Therapy for Carcinoma of the Esophagus: A New Form of Palliative Treatment. Gastroenterology 1983;85: 600-6.

69. Brandt LJ, Kauvar DR. Laser-Induced Transient Regression of Barrett's Epithelium. Gastrointest Endosc 1992;38: 619-22.

70. Berenson MM, Johnson TD, Markowitz NR, Buchi KN, *et al.* Restoration of Squamous Mucosa after Ablation of Barrett's Esophageal Epithelium. Gastroenterology 1993;104: 168691.

71. Dix T, Barr H. Photothermal Ablation of Metaplastic Columnar-Lined (Barrett's) Esophagus, Experimental Studies for Safe Endoscopic Laser Therapy. SPIE, 1996; EBO.

72. Ertan A, Zimmerman M, Younes M. Esophageal Adenocarcinoma Associated with Barrett's Esophagus: Long-Term Management with Laser Ablation. Am J Gastroenterol 1995;90: 2201-
3.

73. Luman W, Lessels AM, Palmer KR. Failure of Nd-Yag Photocoagulation Therapy as Treatment for Barrett's Oesophagus--a Pilot Study. Eur J Gastroenterol Hepatol 1996;8: 62730.

74. Biddlestone LR, Barham CP, Wilkinson SP, Barr H, *et al.* The Histopathology of Treated Barrett's Esophagus: Squamous Reepithelialization after Acid Suppression and Laser and Photodynamic Therapy. Am J Surg Pathol 1998;22: 239-45.

75. Gossner L, May A, Stolte M, Seitz G, *et al.* Ktp Laser Destruction of Dysplasia and Early Cancer in Columnar-Lined Barrett's Esophagus. Gastrointest Endosc 1999;49: 8-12.

76. Sharma P, Jaffe PE, Bhattacharyya A, Sampliner RE. Laser and Multipolar Electrocoagulation Ablation of Early Barrett's Adenocarcinoma: Long-Term Follow-Up. Gastrointest Endosc 1999;49: 442-6.

77. Sharma P, Jaffe P, Bhattacharyya A, Sampliner RE. Fate of High Grade Dysplasia at 1 Year after Endoscopic Ablation with Nd:Yag Laser and Electrocautery: 79. Official journal of the American College of Gastroenterology | ACG 2000;95: 2433-34.

78. Weston AP, Sharma P. Neodymium:Yttrium-Aluminum Garnet Contact Laser Ablation of Barrett's High Grade Dysplasia and Early Adenocarcinoma. Am J Gastroenterol 2002;97: 2998-3006.

79. Gostout CJ. Gastrointestinal Laser Endoscopy--Future Horizons. Mayo Clin Proc 1990;65: 509-17.

80. Bashkatov AN, Genina EA, Kochubey VI, Gavrilova AA, *et al.* Optical Properties of Human Stomach Mucosa in the Spectral Range from 400 to 2000nm: Prognosis for Gastroenterology. Medical Laser Application 2007;22: 95-104.

81. Kokhanovsky AA. Light Scattering Reviews 10: Light Scattering and Radiative Transfer. Germany, Springer Berlin Heidelberg, 2015.

82. Collins CM, Smith MB, Turner R. Model of Local Temperature Changes in Brain Upon Functional Activation. J Appl Physiol (1985) 2004;97: 2051-5.

83. Pearce J. Relationship between Arrhenius Models of Thermal Damage and the Cem 43 Thermal Dose. SPIE BiOS. 2009, SPIE, San Francisco, CA, USA.

84. Wilson BC, Adam G. A Monte Carlo Model for the Absorption and Flux Distributions of Light in Tissue. Med Phys 1983;10: 824-30.

85. Keijzer M, Jacques SL, Prahl SA, Welch AJ. Light Distributions in Artery Tissue: Monte Carlo Simulations for Finite-Diameter Laser Beams. Lasers Surg Med 1989;9: 148-54.

86. Prahl S. A Monte Carlo Model of Light Propagation in Tissue. Dosimetry of Laser Radiation in Medicine and Biology, p102-11. 1989, SPIE, Berlin, Germany.

87. Wang L, Jacques SL, Zheng L. Mcml--Monte Carlo Modeling of Light Transport in MultiLayered Tissues. Comput Methods Programs Biomed 1995;47: 131-46.

88. Wang LV, Jacques SL. Monte Carlo Modeling of Light Transport in Multi-Layered Tissues in Standard C. Laser Biology Research Laboratory. 1992, M. D. Anderson Cancer Center, University of Texas.

89. Hale GM, Querry MR. Optical Constants of Water in the 200-Nm to 200-Microm Wavelength Region. Appl Opt 1973;12: 555-63.

90. Glanzmann TM, Zellweger MP, Borle F, Conde R, *et al.* Assessment of a Sheep Animal Model to Optimise Photodynamic Therapy in the Oesophagus. Lasers Surg Med 2009;41: 643-52.

91. Taniguchi DK, Martin RW, Trowers EA, Silverstein FE. Simultaneous M-Mode Echoesophagram and Manometry in the Sheep Esophagus. Gastrointest Endosc 1995;41: 582-6.

92. Radu A, Conde R, Fontolliet C, Wagnieres G, *et al.* Mucosal Ablation with Photodynamic Therapy in the Esophagus: Optimization of Light Dosimetry in the Sheep Model. Gastrointest Endosc 2003;57: 897-905.

93. Hohmann M, Lengenfelder B, Kanawade R, Klämpfl F, *et al.* Measurement of Optical Properties of Pig Esophagus by Using a Modified Spectrometer Set-Up. J Biophotonics 2018;11.

94. Kays WM, Crawford ME. Conservation Principles. In, editors. Convective Heat and Mass Transfer. 3 ed. New York: McGraw-Hill Higher Education; 1993. p.

95. Jacques SL. Laser-Tissue Interactions. Photochemical, Photothermal, and Photomechanical. Surg Clin North Am 1992;72: 531-58.

96. Welch AJ, van Gemert MJC. Optical-Thermal Response of Laser-Irradiated Tissue. 2, Springer Science & Business Media, 2011.

97. Jaluria Y, Kenneth ET. Computational Heat Transfer. 2. New York, Taylor & Francis, 2003.

98. Lowan AN. On Stability Criteria of Explicit Difference Schemes for Certain Heat Conduction Problems with Uncommon Boundary Conditions. Mathematics of Computation 1961;15: 179-85.

99. Pearce JA. Thermodynamic Principles of Laser - Tissue Interaction. Proceedings of the Twelfth Annual International Conference of the IEEE Engineering in Medicine and Biology Society, p1108-10. 1990, Philadelphia, PA, USA.

100. Thomsen S. Pathologic Analysis of Photothermal and Photomechanical Effects of LaserTissue Interactions. Photochem Photobiol 1991;53: 825-35.

101. Henriques FC, Moritz AR. Studies of Thermal Injury: I. The Conduction of Heat to and through Skin and the Temperatures Attained Therein. A Theoretical and an Experimental Investigation. Am J Pathol 1947;23: 530-49.

102. Moritz AR, Henriques FC. Studies of Thermal Injury: Ii. The Relative Importance of Time and Surface Temperature in the Causation of Cutaneous Burns. Am J Pathol 1947;23: 695720.

103. Moritz AR. Studies of Thermal Injury: Iii. The Pathology and Pathogenesis of Cutaneous Burns. An Experimental Study. Am J Pathol 1947;23: 915-41.

104. Henriques FC. Studies of Thermal Injury: V. The Predictability and the Significance of Thermally Induced Rate Processes Leading to Irreversible Epidermal Injury. Arch Pathol 1947;43: 489-502.

105. Eichler HJ, Eichler J, Lux O. Laser Beam Propagation in Free Space. In, editors. Lasers: Basics, Advances and Applications ed. Cham: Springer International Publishing; 2018. p. 207-29.

106. From https://omlc.org/software/mc/mcxyz/index.html, Retrieved May 2021.

107. Schölvinck DW, Belghazi K, Pouw RE, Curvers WL, *et al.* In Vitro Assessment of the Performance of a New Multiband Mucosectomy Device for Endoscopic Resection of Early Upper Gastrointestinal Neoplasia. Surg Endosc 2016;30: 471-79.

108. Houmsse M, Daoud EG, Joseph M, Weiss R, *et al.* Evaluation of a Novel Esophageal Retractor Utilizing Vacuum Suction and Mechanical Force for Deviating the Esophagus. J Cardiovasc Electrophysiol 2020;31: 1661-69.

109. Kararli TT. Comparison of the Gastrointestinal Anatomy, Physiology, and Biochemistry of Humans and Commonly Used Laboratory Animals. Biopharm Drug Dispos 1995;16: 351-80.

110. Odze RD. Barrett Esophagus: Histology and Pathology for the Clinician. Nature Reviews Gastroenterology & Hepatology 2009;6: 478-90.

111. Fothergill LJ, Galiazzo G, Hunne B, Stebbing MJ, *et al.* Distribution and Co-Expression Patterns of Specific Cell Markers of Enteroendocrine Cells in Pig Gastric Epithelium. Cell Tissue Res 2019;378: 457-69.

112. Wang Z, Simoncelli EP, Bovik AC. Multiscale Structural Similarity for Image Quality Assessment. The Thrity-Seventh Asilomar Conference on Signals, Systems & Computers, 2003, p1398-402 Vol.2. 2003, Pacific Grove, CA, USA.

113. Di Gesù V, Starovoitov V. Distance-Based Functions for Image Comparison. Pattern Recognition Letters 1999;20: 207-14.

7. APPENDIX

7.1. Ex vivo Tissue Handling Protocol

1. Obtain esophagus/stomach from slaughterhouse.
2. Keep ex vivo tissue samples at +4^{o}C.
3. Remove excessive fat accumulation and the adventitia from outer surface with bisturi.
4. Clean with isotonic saline solution five times.
5. Dissect longitudinally with bisturi before/after laser irradiation.
6. Moisturize with isotonic saline solution if necessary.
7. Take gross images after irradiation.
8. Fix with 10% neutral formalin for 1 week.
9. Perform tissue processing.
10. Embed the tissue into paraffin.
11. Section paraffin embedded tissue as 5 µm.
12. Stain sectioned samples with H&E.

7.2. Research Ethics Committee Approvals

İZMİR BİYOTIP VE GENOM MERKEZİ
HAYVAN DENEYLERİ YEREL ETİK KURULU

Prof. Dr. Şermin GENÇ

Biyofotonik ve Optik Görüntüleme Laboratuvarı'nda doktora öğrencisi olan Merve TÜRKER BURHAN tarafından gerçekleştirilen "Sınırları tanımlı ve açı kontrollü foto-ısısal özofagus mukozası ablasyonu sağlayan endoskopik bir kapsülün geliştirilmesi - Development of an endoscopic capsule that provides well-confined and angle-controlled photo-thermal esophageal mucosa ablation" başlıklı tez çalışması kapsamında yapılacak deneylerde mezbaha ve/veya kasaptan temin edilecek canlı dışı koyun yemek borusu dokusu kullanılacağından dolayı, Resmi Gazete'nin 15/02/2014 tarih ve 28914 sayılı Hayvan Deneyleri Etik Kurullarının Çalışma Usul ve Esaslarına Dair Yönetmeliğinin 8. maddesi (k) fıkrasında belirtilen "Ölü hayvan veya dokusu, mezbaha materyalleri, atık fetüsler ile yapılan prosedürler" kapsamında gerçekleştirilecek olan deneysel faaliyetler HADYEK iznine tabi değildir.

Bilgilerinizi arz ederim.

Doç. Dr. H. Güneş ÖZHAN BAYKAN
İBG-HADYEK Başkanı

Adres: Dokuz Eylül Üniversitesi Sağlık Yerleşkesi Mithatpaşa Cad. No:58/5 35340 Balçova-İZMİR
Telefon: +90 (232) 299 41 00

7.3. Curriculum Vitae

Merve Turker Burhan¨

Dokuz Eylul University &¨ ˙Izmir Biomedicine and Genom Center, ˙Izmir, Turkey +90(543)-523-3938
merveturkerburhan@gmail.com www.linkedin.com/in/merveturkerburhan¨

EDUCATION

Sep 2017 - Aug 2023	Dokuz Eylul University	*Izmir, Turkey*
(expected)	*Integrated Doctor of Philosophy in Molecular Biology and Genetics (cGPA 3.83/4.00)*	
Sep 2011 - June 2016	Izmir Institute of Technology	*Izmir, Turkey*
	Bachelor of Science in Molecular Biology and Genetics (GPA 3.03/4.00)	

EXPERIENCE

Sep 2016 - present	Izmir Biomedicine and Genom Center *Assistant Researcher in Biophotonics and Optical Imaging Laboratory* *Supervisor: Serhat Tozburun, Ph.D.* *Project: H2020 Marie Skłodowska-Curie Actions Grant #835907 (2017)* *Project: TUBITAK 117E985 (2017-2020)* *Project: TUBITAK 122E157 (2022-present)* *Project: TUSEB 16762 (2022-present)*	*Izmir, Turkey*
May 2013 - Aug 2016	Izmir Institute of Technology *Researcher in Controlled in vitro Microenvironments Laboratory* *Supervisor: Devrim Pesen Okvur, Ph.D.* *Project: FP7 Marie Curie Grant #PIRG08- GA-2010-276976 (2014-2016)*	*Izmir, Turkey*

HONORS AND AWARDS

- *2023* 2250-Graduate Scholarships Performance Program
- *2022* The Aegean Start-ups Programme Second Prize from IOM Turkey
- *2022* Fatos¸ Buy¨ ukkus¸o¨ glu Strong Women Award from Arya Women Investment Platformˇ
- *2022* 2224-A Grant Program for Participation in Scientific Meetings Abroad
- *2022* SPIE Student Travel Award
- *2021 - present* TUBITAK BIDEB 2211-A National PhD Scholarship
- *2020* SPIE Student Travel Award
- *2019* Onkolojide ˙Iz Bırakanlar Zirvesi Student Travel Award
- *2017 - 2022* YOK 100/2000 PhD Scholarship¨
- *2016* Izmir Institute of Technology Honor Student Graduation

PATENTS

- *2021* Tozburun, S., Turker-Burhan, M.¨ , and Ellidokuz, E.B., "Sınırları tanımlı anormal mukozal doku ablasyonu ic¸in negatif basınc¸ temelli gor¨ unt¨ uleme ve tedavi aparatı ve¨ sistemi ve sistemin c¸alıs¸ma yontemi / Negative pressure based imaging and therapeutic¨ apparatus and system for well-confined abnormal mucosal tissue ablation and working method of the system"

  PCT International Application - PCT/TR2022/050113 ePATs
  Patent Application - TR 2021/001949

COURSES & CERTIFICATES

- *2022* 2237-A Grant Program for Scientific Training - Article Writing Training
- *2022* Aegean Start-ups Programme Focused Entrepreneurship Training
- *2022* Aegean Start-ups Programme General Entrepreneurship Training
- *2021* Basic Clinical Research (Good Clinical Practice) Training Certificate
- *2019* MENTORING Experimental Animals Use Certificate

Aug 2022 - present	Seval Unal *An Endoscope Cap Producing Precise Photothermal Coagulation Depth and Allowing Positioning (i.e., navigation)*
Fep 2022 - present	Guldeniz G¨ulcan¨ *An Endoscopic Cap for Non-thermal Mucosal Ablation with Accurate Ablation Limits*
June 2021 - July 2021	Hilal Sak *Arbitrary Waveform Generator Manual*
Mar 2021 - June 2021	Nilda Saatli - Selinnur C¸ akmak *Bacterial Culture*

PUBLICATIONS

Peer Reviewed Publications:

- Turker-Burhan, M.¨ , and Tozburun, S., "Monte-Carlo method based simulations for photothermal mucosa coagulation with accurate depth limits," Turk J Electr Eng & Comp Sci. 30:2605-2616 (2022).
- Turker-Burhan, M.¨ , Ersoy, N., Bagriyanik, H. and Tozburun, S., "Guide mapping for effective superficial photothermal coagulation of the esophagus using computer simulations with ex vivo sheep model validation study," Lasers Surg Med. 54:1116-1129 (2022).
- Onal, S., Turker-Burhan, M.¨ , Batı-Ayaz, G., Yanık, H. and Pesen-Okvur, D., "Breast cancer cells and macrophages in a paracrine-juxtacrine loop," Biomaterials. 267:120412 (2021).

Conference Proceedings:

- Turker-Burhan, M.¨ , and Tozburun, S., “An endoscopic approach to limit the depth of laser-induced thermal injury,” European Conferences on Biomedical Optics (ECBO) 2023 (in press).

- Turker-Burhan, M.¨ , Ersoy, N., Bagriyanik, H. and Tozburun, S., “Optimization study of parameters for laserinduced thermal treatment of the esophageal mucosal layer,” European Conferences on Biomedical Optics (ECBO) 2023 (in press).
- Arlı, B., Dinc, O. F., Turker-Burhan, M.¨ , and Tozburun, S., “Predicting dark-field images of H&E-stained esophageal specimens,” European Conferences on Biomedical Optics (ECBO) 2023 (in press).
- Turker-Burhan, M.¨ , and Tozburun, S., “An endoscopy capsule for well- confined and angle-controlled photothermal mucosa ablation,” Proc. SPIE. 11958:119580C1-5 (2022).
- Turker-Burhan, M.¨ , Bagrıyanık, A. and Tozburun, S., “Ex-vivo Model Experimental and Simulation Results˘ Suggesting Effective and Superficial Mucosal Photothermal Ablation at 1505 nm,” European Conferences on Biomedical Optics (ECBO) 2021, OSA Technical Digest. Paper ETh2A.8 (2021).
- Turker-Burhan, M.¨ and Tozburun, S., “Monte-Carlo Based Simulations of Photothermal Response of Nerve Tissue for Laser Wavelengths of 1455 nm, 1490 nm, 1550 nm,” Proc. SPIE. 11238:1123814 (2020).
- Turker, M.¨ and Tozburun, S., “Simulations for Modeling the Photothermal Response of Nerve Tissue,” Proc. SPIE.11079:110791N (2019). Abstracts:
- Unal, S., Gulcan, G., Turker-Burhan, M.¨ and Tozburun, S., “Computer Modeling for Heat Transfer in Circumferential Mucosal Surface,” Fotonik 2022. Turkey (2022).
- Turker-Burhan, M.¨ Ersoy, N., Bagriyanik, H. and Tozburun, S., “A Guide Map for Effective Superficial Photothermal Coagulation of the Esophagus,” Fotonik 2022. Turkey (2022).
- Turker-Burhan, M.¨ and Tozburun, S., “An Image Analysis Protocol for the Assessment of Photothermal Mucosal Coagulation,” Fotonik 2021. Turkey (2021).
- Turker-Burhan M.¨ and Tozburun, S., “A Simulation Study for the Optimization of Photothermal Ablation of Abnormal Mucosal Tissue,” Onkolojide ˙Iz Bırakanlar 2019. Antalya, Turkey (2019).
- Turker-Burhan, M.¨ and Tozburun, S., “A Map of the Area of Photothermal Damage in Mucosal Tissue,” Fotonik 2019. Istanbul, Turkey (2019).
- Turker-Burhan, M.¨ and Tozburun, S., “Monte-Carlo Simulations for Uniform Distrubition of Laser-Induced Mucosal Tissue Ablation During Surface Scanning,” BIOMED 2019. C¸es¸me, Izmir, Turkey (2019).
- Turker, M.¨ , Yetis¸, O. and Tozburun, S., “Computer Simulations of Photothermal Applications Including Tissue Surface Scanning and Subsurface ONS,” Fotonik 2018. Ankara, Turkey (2018).
- Turker, M.¨ and Tozburun, S., “An Original Endoscopy Probe Head Providing Well-Confined Photothermal Mucosa Ablation,” Fotonik 2017. Istanbul, Turkey (2017) .

PRESENTATIONS

- *2023* European Conferences on Biomedical Optics (ECBO) - Munich (1)
- *2023* European Conferences on Biomedical Optics (ECBO) - Munich (2)
- *2022* 23.Ulusal Optik, Elektro-Optik ve Fotonik C¸alıs¸tayı - Ankara

- *2022* Aegean Start-ups Pitch Deck (CapSTAR) - Izmir • *2022* Internal Seminar - IBG

- *2022* SPIE Photonics West B˙IOS - San Francisco
- *2021* 22.Ulusal Optik, Elektro-Optik ve Fotonik C¸alıs¸tayı - Online
- *2021* European Conferences on Biomedical Optics (ECBO) - Online
- *2020* SPIE Photonics West B˙IOS - San Francisco
- *2019* Onkolojide ˙Iz Bırakanlar Zirvesi - Antalya
- *2019* 24.International Biomedical Science and Technology Symposium (BIOMED2019) - C¸es¸me
- *2019* 21.Ulusal Optik, Elektro-Optik ve Fotonik C¸alıs¸tayı - Istanbul
- *2019* European Conferences on Biomedical Optics (ECBO) - Munich
- *2018* 20.Ulusal Optik, Elektro-Optik ve Fotonik C¸alıs¸tayı - Ankara
- *2017* 19.Ulusal Optik, Elektro-Optik ve Fotonik C¸alıs¸tayı - Istanbul
- *2017* Internal Seminar - IBG

LANGUAGES

- Turkish (Native)
- English (Advanced; YDS score:86.25/100; YOKD¨ ˙IL score: 92.5/100)
- Spanish (Intermediate; A2 Certificate by TOMER)¨

PROFESSIONAL SOCIETIES

- *2019 - present* Society of Photo-Optical Instrumentation Engineers (SPIE) Member

SPECIAL INTERESTS

- Reading, swimming, dancing, painting, learning new skills, designing and decorating

7.4. Publications

Accepted: 6 August 2022

DOI: 10.1002/lsm.23595

PRECLINICAL REPORTS

Guide mapping for effective superficial photothermal coagulation of the esophagus using computer simulations with ex vivo sheep model validation study

Merve **Turker-Burhan** BS[1,2] | Nevin Ersoy PhD[3] |
Husnu A. Bagriyanik MD, PhD[1,3] | Serhat Tozburun PhD[1,2,4]

[1]Izmir Biomedicine and Genome Center, Izmir, Turkey

[2]Izmir International Biomedicine and Genome Institute, Dokuz Eylul University, Izmir, Turkey

[3]Department of Histology and Embryology, Faculty of Medicine, Dokuz Eylul University, Izmir, Turkey

[4]Department of Biophysics, Faculty of Medicine, Dokuz Eylul University, Izmir, Turkey

Correspondence
Serhat Tozburun, PhD, Izmir International Biomedicine and Genome Institute, Dokuz Eylul University, Izmir 35340, Turkey. Email: serhat.tozburun@deu.edu.tr

Funding information
Türkiye Bilimsel ve Teknolojik Arastirma Kurumu, Grant/Award Number: 117E985; H2020 Marie Sklodowska-Curie Actions, Grant/Award Number: 835907

Abstract

Objectives: The transfer and widespread acceptance of laser-induced thermal therapy into gastroenterology remain a topic of interest. However, a practical approach to the quantitative effect of photothermal injury in the esophagus needs further investigation. Here, we aim to perform computer simulations that simulate laser scanning and calculate the laser-induced thermal damage area. The simulation engine offers the results in a guide map for laser coagulation with a well-confined therapeutic area according to laser irradiance and surface scanning speed. The study also presents validation experiments that include histology analyses in an ex vivo sheep esophagus model.

Methods: The simulation engine was developed based on the Monte-Carlo method and the Arrhenius damage integral. The computational model mimicked laser scanning by shifting the position of the calculated heat source in the grating system along the axis to be scanned. The performance of the simulations was tested in an ex vivo sheep esophagus model at a laser wavelength of 1505 nm. Histological analysis, hematoxylin–eosin staining, light microscope imaging, and block-face scanning electron microscopy were used to assess thermal damage to the tissue model.

Results: The developed simulation engine estimated the photothermal coagulation area for a surface scanning speed range of 0.5–8 mm/second and laser power of up to 0.5 W at a 0.9-nm laser diameter in a tissue model with a volume of $4 \times 4 \times 4$ mm^3. For example, the optimum laser irradiation for effective photothermal coagulation in the mucosa and superficial submucosa depths was estimated to be between 16.4 and 31.8 W/cm^2, 23.2 and 38.1 W/cm^2 at 0.5 and 1 mm/second, respectively. The computational results, summarized as a guide map, were directly compared with the results of ex vivo tissue experiments. In addition, it was pointed out that the comparative theoretical and experimental data overlap significantly in terms of energy density.

Conclusions: Our results suggest that the developed simulation approach could be a seed algorithm for further preclinical and clinical trials and a complementary tool to the laser-induced photothermal coagulation technique for superficial treatments in the gastrointestinal tract. In future preclinical studies, it is thought that the simulation engine can be enriched by combining it with an in vivo model for different laser wavelengths.

KEYWORDS
esophageal mucosa, laser coagulation, laser therapy, Monte-Carlo simulations

INTRODUCTION

Of the four layers (mucosa, submucosa, muscularis externa, and serosa) that constitutes the gastrointestinal wall,[1] the mucosa is the first tissue layer to be accessed in endoscopic procedures. This structure facilitates minimally invasive treatment of mucosal lesions when necessary in certain critical cases, as precancerous mucosal lesions are associated with gastrointestinal tract malignancies (e.g., esophageal cancer, gastric cancer, colon cancer, and rectal cancer).[2] In surgical treatments, endoscopic therapeutic interventions are widely used to eliminate abnormal mucosal tissue (e.g., Barrett's esophagus, a precancerous esophagus condition)[3] that may spread to deeper tissue structures over time. Endoscopic mucosal resection and endoscopic thermal therapy are generally accepted treatment methods among these interventions.

We can list various techniques for endoscopic thermal therapy,[3–5] such as multipolar electrocoagulation, radiofrequency (RF) ablation, argon plasma coagulation, cryotherapy, and photothermal coagulation. RF ablation and argon plasma coagulation are two noticeable techniques for exposing the tissue to heat energy. In RF ablation, the delivery of high-frequency alternating current (350–500 kHz) through electrodes in direct contact with tissue provides heat generation for thermal injury.[6] Argon plasma coagulation inflicts thermal damage to the target tissue by transmitting high-frequency energy through argon gas flow to induce heat generation in a noncontact manner.[7]

However, although endoscopic therapeutic interventions efficiently eradicate superficial abnormal tissues, the main challenge with their current deployments is that the therapy depth typically has a more profound thermal injury than the target layer.[8] This unintentional failure of possible thermal damage, coupled with multiple treatment sessions, results in organ narrowing, bleeding, or perforation. To address this challenge, an approach that provides a limited depth of the thermal effect to the epithelial layer (~500 μm thick),[9,10] particularly at the micrometer scale, may be of interest. With the latest developments in fiber optic components and diode laser technologies, laser-

induced photothermal coagulation (i.e., laser therapy method) may once again come to the fore as the closest approach.

Photothermal coagulation uses laser radiation to deliver heat energy to the esophageal mucosal lining. The primary mechanism is to match the laser wavelength and corresponding optical penetration depth to the therapeutic depth in the targeted layer. In this context, various laser types and laser wavelengths have been tried before in mucosal ablation applications.[11–16] Despite some limitations, these studies have shown promising results in clinical settings. However, the treatment parameters, including laser irradiance, surface scanning speed, and laser energy density, provide a relatively sizeable variable matrix that must be optimized for consistent and reliable superficial treatment. Besides, these critical parameters have been chosen empirically without adequate comparison with the theory in the literature. Therefore, it may be necessary to develop a simulation algorithm (i.e., simulation engine) that simulates photothermal coagulation of esophageal layers in optimizing the parameters.

This study presents computer simulations that calculate a guide map of the area of irreversible thermal damage at a well-confined depth. The map simplified a matrix of laser irradiance, beam diameter, and surface scanning speed for successful superficial laser therapy. The study also included validation of the map in an ex vivo sheep model using a 1505-nm laser operated in continuous-wave (CW) mode with constant beam diameter.

MATERIALS AND METHODS

Laser-induced photothermal coagulation simulations

A simulation engine was developed to examine the matrix formed by the laser irradiance and surface scanning speed parameters, mainly to calculate the wavelength-dependent, depth-resolved photothermal coagulation area (i.e., the laser-induced thermal damaged area). Figure 1 shows the block flowchart of the four-module model. The first module was based on the Monte-Carlo technique[17,18] using the multilayer approach and estimated the threedimensional (3D) photon weight distribution of an infinitely narrow photon beam with circular symmetry. The calculation corresponded to the probability of absorption and scattering events. In light propagation with randomly sampled step sizes, the events at each step were described by the following wavelength-dependent optical properties: absorption coefficient, scattering coefficient, relative refractive index, and anisotropy factor. In the second module, the calculated photon weight distribution was interpolated on a 3D grid in the Cartesian coordinate system, normalized to 1 in power, and convolved to derive a Gaussian laser beam profile. Thus, the power density was estimated as a function of the grid system and beam diameter inputs. The physical size of the single-layer, homogeneous tissue model was 4 mm in all axes (x,y,z). A uniform grid system (i.e., 100 × 100 × 100) with a mesh size of 40 × 40 × 40 μm^3 constituted the 3D structure. The thickness of the tissue sample was determined to be 4 mm, which is the sum of mucosal layer thickness (0.54 mm), submucosal layer thickness (0.55 mm), muscularis layer thickness (0.63 mm), and muscle layer (>2 mm).[9] The third module simulated the time-dependent heat diffusion generated by laser power density (i.e., laser irradiance) utilized as a heat source. The numerical model of heat diffusion was based on a partial differential equation governed by the heat transfer laws.[19] The equation was solved by the finite difference method over time and space,

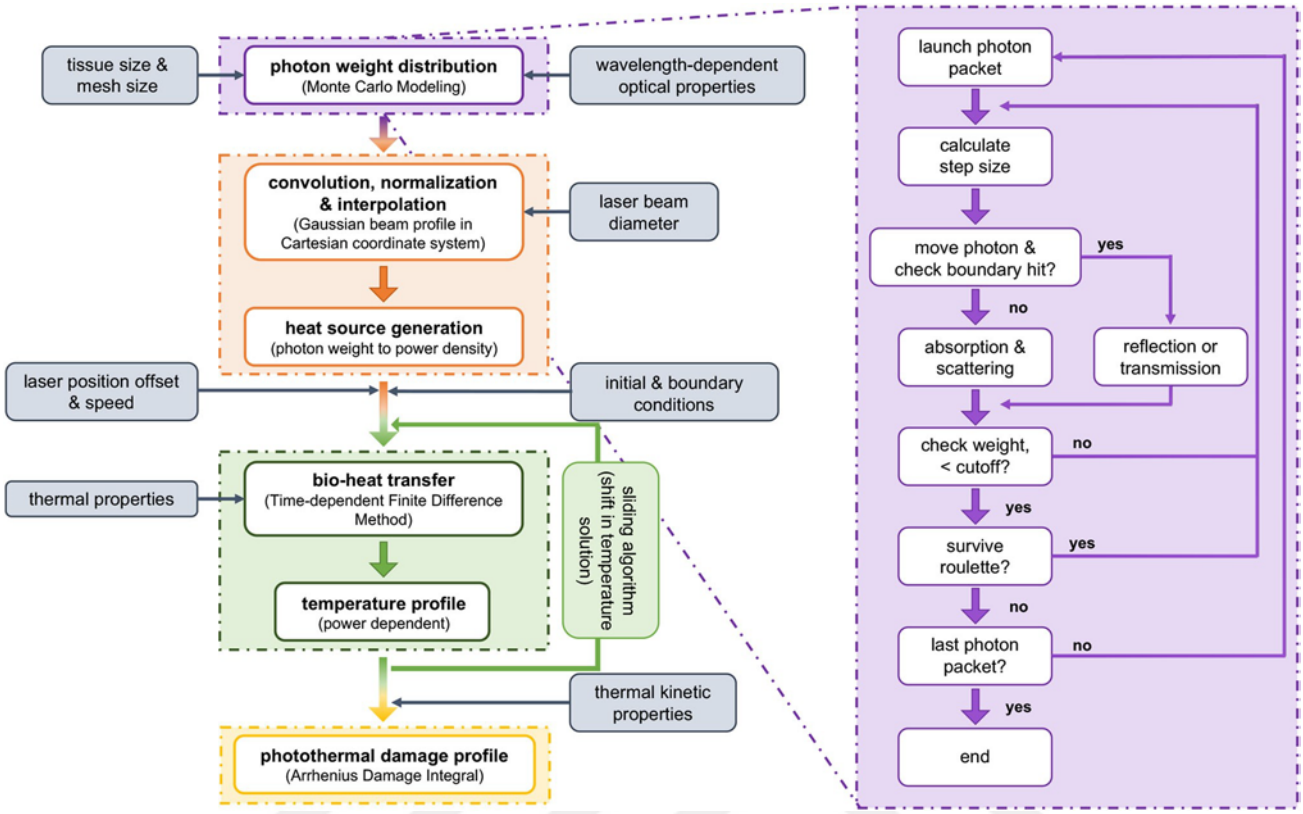


FIGURE 1 Flowchart of the four-module simulation engine

performed on a custom-written Objective-C++ code by Xcode (Apple, Inc.)

$$\rho C \frac{\partial T}{\partial t} = k\nabla^2 T + Q, \quad (1)$$

where ρ is the density, C is the specific heat capacity, and k is the thermal conductivity, Q represents the heat source computed by using Modules 1 and 2, and T is the simulated tissue temperature (x,y,z, time).

The initial position of the calculated heat source in the grid system was shifted along the axis to be scanned to mimic the scanning of laser radiation on the tissue surface. The mesh size of 40 μm was the unit shift distance. The unit time step corresponding to the calculated surface scanning speed was assigned according to the mesh size of 40 μm. For instance, the unit step time is defined as 40 ms for a 1 mm/ second scanning speed and 80 milliseconds for 0.5 mm/ second. To avoid discrete calculations, the partial differential equation is iteratively solved in 10 microseconds unit time, including the new boundary conditions at each heat source shift. Due to limited memory usage, a total of 1000 solutions were saved at equal intervals from the high number of iterations.

For example, Figure 2A shows representative simulation results of transient temperature calculations from the surface at selected time points from 25 milliseconds (t_0) to 2.5 seconds (t_{999}) for the scanning speed of 1 mm/ second. The laser power was 309 mW, corresponding to the irradiance of 48.6 W/cm^2 for a fixed laser spot diameter (0.9 mm at the surface). In the calculations, the initial tissue temperature was set to 37°C. Figure 2B shows the 3D temperature distribution in the tissue model when the highest temperature 1.37 seconds (t_{547}) is reached during the simulation (from t_0 to t_{999}). Both surface and cross-sectional views are provided for a clear presentation of 3D transient temperature calculations. The customized color bar indicates the temperature range from 37°C to 115°C.

In the last module, laser-induced thermal damage was estimated in four-dimensions (x,y,z, time) using simulated temperature distributions for different sets of laser irradiation and surface scanning speeds, as exemplified for a single set in Figure 2. The module was based on the Arrhenius damage integral[20] to generate the thermal injury parameter (Ω) followed by a normalization factor, representing the fraction of coagulated proteins in a given volume

$$\Omega = \xi \int_0^{\tau} e^{-E_a/RT} dt, \quad (2)$$

where is ξ the frequency factor, τ is the total heating time, E_a is the activation energy of transformation, R is the universal gas constant, and T is the absolute temperature of the tissue in Kelvin.

The damage index, called the damage probability, was produced by normalizing the thermal injury parameter to 1. The damage index grade is 1, corresponding to a necrotic cell concentration of 63%, while 4.6 corresponds to a necrotic cell concentration of 99%.

The optical properties at 1505 nm, thermal properties, and kinetic coefficients of the tissue model used in the simulation were compiled from the literature (Table 1). Besides, it was assumed that the coefficients are independent of temperature changes. Body temperature was fixed to 37°C during all simulations. The total number of unit-weighted photons required to accurately simulate the absorbed radiation distribution in the tissue model with sufficient spatial resolution was determined as one million. Modules 1 and 3 of the simulation engine were developed with the C programming language. Calculations in Modules 2 and 4 and all graphical analyses of the simulation engine have been completed on MATLAB (Mathworks, Inc.).

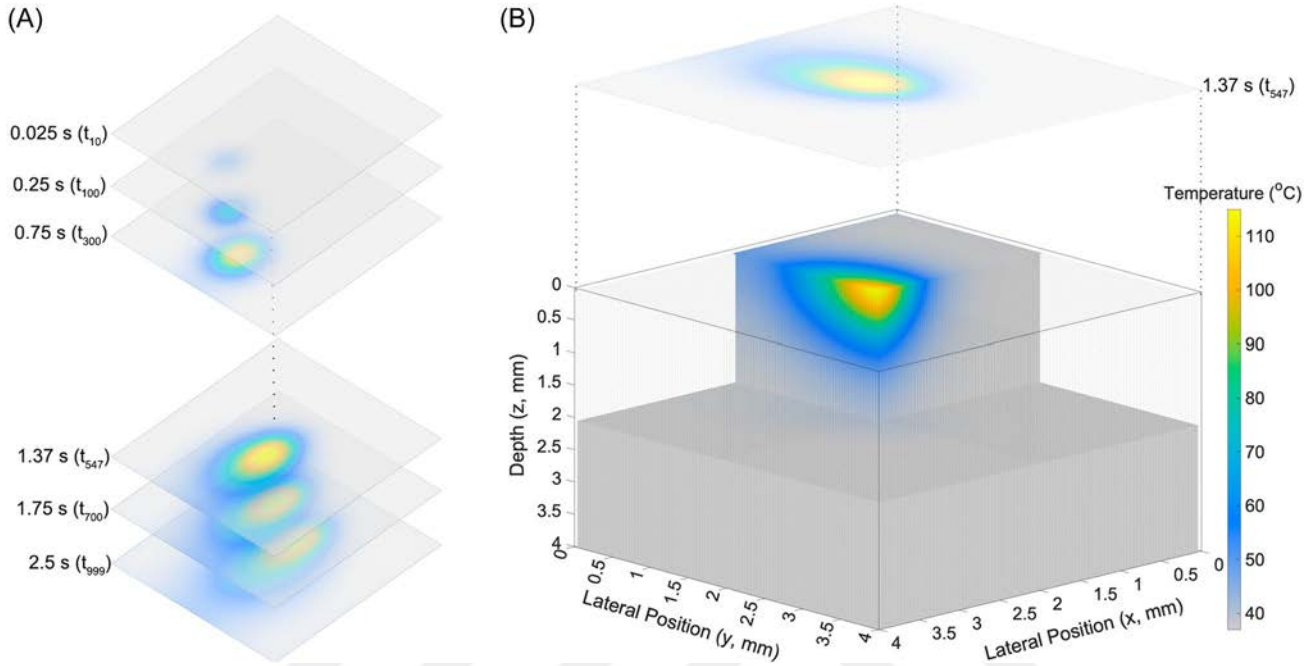


FIGURE 2 Representative simulation results of transient temperature calculations from the surface at selected time points from 25 milliseconds (t_0) to 2.5 seconds (t_{999}) (A). Three-dimensional temporal temperature distribution in the tissue model when the highest temperature is reached during the simulation (B). The laser power is set to 309 mW, corresponding to 48.6 W/cm² radiation for a 0.9 mm beam diameter, and the surface scanning speed is 1 mm/second.

Experimental setup for ex vivo tissue studies

At this early stage, we planned ex vivo tissue studies as a guide, albeit limited, and thus also took into account the replacement approach of the 3Rs (replace, reduce, and refine). The sheep esophagus was chosen as the tissue model because of its easy accessibility and similarity to the human

TABLE 1 Optical properties, thermal properties, and thermal kinetic properties used in simulation studies

	Tissue
Optical properties at 1505 nm	Mucosa
Absorption coefficient (cm^{-1})	12[21]
Reduces scattering coefficient (cm^{-1})	9.5[21]
Anisotropy factor	0.6[21]
Refractive index	1.33
Thermal properties	Esophagus
Thermal conductivity (W/m°C)	0.527[22]

Specific heat (J/kg°C)	3720[22]
Density (kg/m^3)	1050[22]
Kinetic coefficients	
Frequency factor (second^{-1})	1.3e95[23]
Activation energy (J/mol)	4.6e5[23]
Universal gas constant (J/kmol)	8.32

esophagus in terms of morphology and layer thickness.[24–27] All ex vivo esophageal studies were performed in a fume hood (Köttermann), which provides a biologically safe environment, as approved by the Biosafety Board of the Izmir Biomedicine and Genome Center.

The surface of the fresh sheep esophagus, taken from the slaughterhouse, was cleaned with saline solution. We obtained a 20-mm-long rectangular form from a cylindrical structure by performing full-thickness longitudinal dissection to reach the inner surface of the esophagus. Before photothermal coagulation studies, the tissue surface was made as flat as possible with a small metal spatula. We then investigated coagulation parameters (i.e., laser power at fixed spot size, scanning speed, scanning time) with a raster scanning pattern. While the surface scanning speed was determined and kept constant in each pattern, the laser power was increased for each line. The protocol was repeated for each ex vivo tissue to explore different scanning speeds. In this context, experiments were carried out in four groups for speeds of 0.5, 1.0, 1.5, and 2.0 mm/second.

Figure 3 also presents measurements of the laser parameters used in the study in panels B, C, and D. For example, the central wavelength of the diode laser operated in CW mode was measured as 1502.83 nm (AQ6370D; Yokogawa), shown in Figure 3B. The probe produced a laser output power of up to 390 mW (Figure 3C). Output power for each scanning speed was set to a total of seven values ranging from 133 to 309 mW, as shown in the blue shaded area in Figure 3C. Using the knife-edge measurement technique, we characterized the probe, which delivers an ~0.9 mm diameter beam (1/e^2)

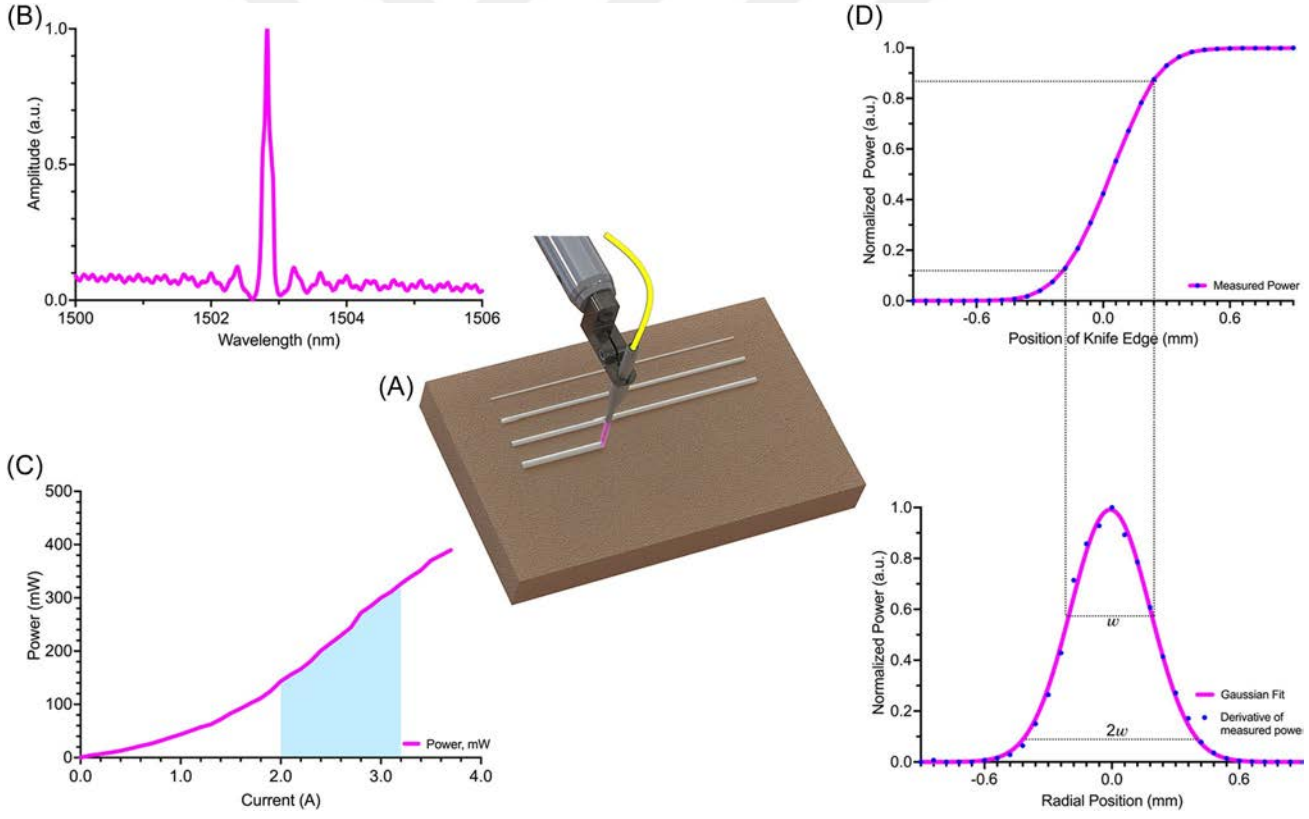


FIGURE 3 Schematic representation of the protocol followed in ex vivo tissue studies (A). The emission spectrum of the diode laser used in the experiments (B). The wavelength was measured as 1502.83 nm. A graph of the laser output power delivered through a GRIN lens as a function of the applied electric current (C). The light blue area indicates the power range (133–309 mW) used during laser coagulation studies. Normalized laser powers along the knife-edge position and Gaussian fitted first derivatives (D). The estimated diameter of the laser beam produced by the GRIN lens using the knife-edge method was ~0.9 mm (1/e^2).

Figure 3A shows the protocol followed in ex vivo tissue studies.

on the tissue surface (Figure 3D) and maintains the beam diameter at a working distance of 20 mm. Therefore, the power range corresponded to incident irradiance values between 20.9 and 48.6 W/cm^2 for a fixed laser spot diameter (0.9 mm at the surface).

Figure 4 shows the experimental setup used in ex vivo studies. The setup mainly consisted of a laser source, an XYZ linear translation optomechanical stage, a hot plate, and a digital microscope. A single-mode fiber-coupled diode laser (BrightLock; QPC

Lasers Inc.) emitting laser power up to 500 mW at a wavelength of 1505 nm was used as the near-infrared (near-IR) light source. We combined the laser output with a pigtailed GRIN collimator (Go4Fiber) housed in glass tubing used as a probe. Laser radiation at 1505 nm provided an optical penetration depth of >0.57 mm in water,[28] the primary chromophore for soft tissues in the near-IR spectrum. With the identical motorized micrometer actuators (Z825B; Thorlabs), the three-axis optomechanical stage provided excellent probe control across the tissue surface, parallel and perpendicular, respectively. The actuator offered a relatively accurate scanning speed of up to 2.3 mm/second with a maximum travel length of 25 mm with a step size of 0.029 µm. Ex vivo tissue at room temperature of 22°C was placed in a tray in contact with a hot plate (Thermo Fisher Scientific) set to 45°C to raise it to body temperature (37°C). We constantly checked the surface temperature with a thermocouple. A digital microscope (AM4815ZTL Dino-Lite) helped align the probe while recording the photothermal coagulation process in the invisible wavelength range.

Histology

After the photothermal coagulation studies, tissue samples (~20 mm long) were collected to measure the depth and area of thermal damage. The collected samples were fixed in 10% neutral formalin to preserve their current state and embedded in paraffin to prepare for the sectioning process. Then, the region of interest was longitudinally sectioned from the paraffin blocks at a thickness of 5 µm. Finally, tissue processing steps were followed for standard histology analysis and electron microscopy.

For the histological study, hematoxylin–eosin (H&E) staining was performed for further microscopy examination, including brightfield and darkfield imaging. In addition, we coated some tissue sample pieces with 5-nmthick gold using the rotary pump coating system and imaged them to support the determination of the damage boundary by electron microscopy examination.

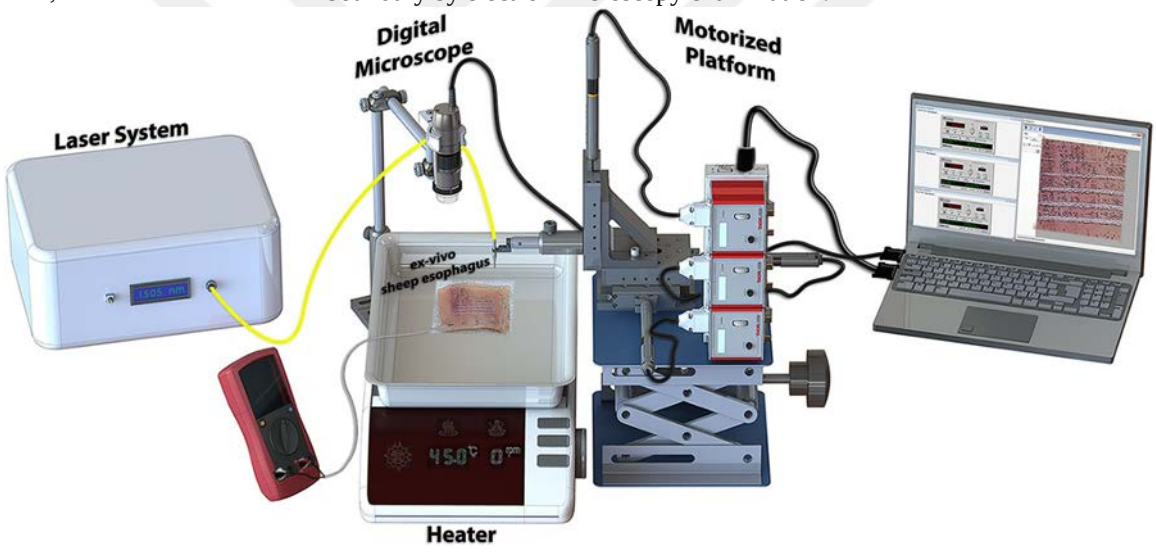


FIGURE 4 Schematic drawing of the experimental setup used in an ex vivo sheep esophagus model. A single-mode fiber-coupled diode laser at 1505 nm is used as the near-infrared light source. The laser is coupled with a pigtailed GRIN collimator housed in glass tubing used as a probe. The setup also includes an XYZ linear translation optomechanical stage for precise control of the fiber probe across the ex vivo tissue surface, a thermocouple for instantaneous temperature measurement of the tissue, a digital microscope for alignment, and a hot plate to maintain the tissue temperature at 37°C.

RESULTS

This section shows laser-induced thermal calculations based on computer simulations developed using the Monte-Carlo technique. For simplicity, we present the calculations as a guide map of the thermally damaged area as a function of two variables: laser irradiance and surface scanning speed. Various studies are then covered, including ex vivo fresh sheep esophagus experiments and histology analysis to validate the simulation results.

Mapping photothermal coagulation of esophageal layers

In the simulation study, laser-induced thermal injury of mucosal tissue was estimated in a depth-resolved manner for various scanning speeds and laser power settings (for a

fixed beam diameter of 0.9 mm, the corresponding laser beams were subsequently calculated). A guide map of the formation of the damaged area was created for easier reading of the results produced with the developed simulation engine. Figure 5 shows a map of the estimated damaged area as a function of laser irradiance (or flux density) and surface scanning speed. The map was created in three stages: first, we simulated sliding the probe along the surface of the esophagus in one direction at a constant speed. The four-dimensional (4D) temperature distribution was calculated by iteratively solving the partial differential equation (Equation 1) in 10 microseconds unit time, including the new boundary conditions at each heat source shift. As depicted in Figure 2,

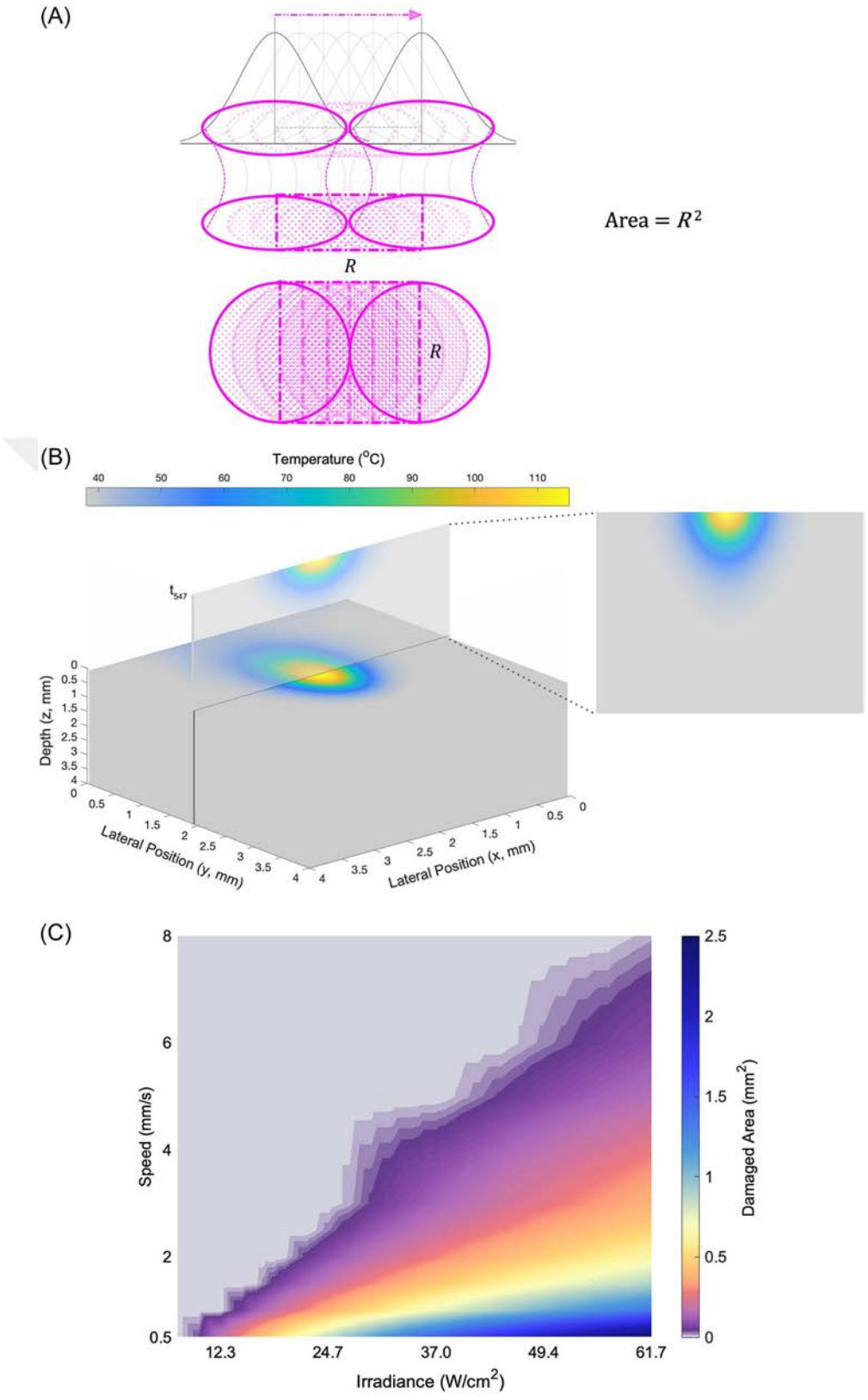


FIGURE 5 In calculating laser irradiance, the surface area perpendicular to the beam propagation is assumed as a square given the >99% overlap of the laser beam and approximates to the square of the beam diameter (A). Surface area = R^2. The cross-sectional (y,z) solutions of the highest temperature (T_{max}) reached during the simulation are gathered from the calculated temperature distributions (x,y,z, time) for each surface scanning speed and laser power (B). A map of

the estimated damaged area as a function of laser irradiance (i.e., flux density) and surface scanning speed (C). Laser power varies from 60 to 500 mW with a step size of 20 mW. Scanning speeds: 0.5, 1, 1.5, 2, 2.5, 3, 5, 6, and 8 mm/second. The color code represents that the damaged area varies across the graph by interpolating the calculated values for a nondiscrete data display.

a total of 1000 solutions were recorded evenly spaced from multiple iterations. The simulations were then repeated for speeds between 0.5 and 8mm/s. In the simulation of laser surface scanning at a distance of 2.5 mm, the mimicked near-IR laser exposure time was 5 seconds for 0.5 mm/s and ~0.3 seconds for 8 mm/ second. At each scanning speed, the CW laser power was altered from 60 to 500 mW at a step size of 20 mW.

The surface area used in the irradiance calculation was accepted as the area scanned by the laser beam at one diameter distance. As shown in Figure 5A, the surface area perpendicular to the beam propagation was assumed to be a square given the >99% overlap of the laser beam and approximated to the square of the beam diameter (surface area = R^2). Therefore, the laser power from 60 to 500 mW corresponded to an irradiance range of 7.4 to 61.7 W/cm^2 for a 0.9 mm diameter.

The thermally damaged area was calculated from the cross-sectional temperature solutions in the transverse plane to facilitate histology analysis, which is part of the validation studies. As shown in Figure 5B, the cross-sectional (y,z) solutions of the highest temperature (T_{max}) reached during the simulation were gathered from the calculated temperature distributions $(x,y,z,time)$ for each surface scanning speed and laser power in the second stage. Based on temperature changes over time (i.e., gathered temperature distributions) and thermal kinetics of mucosal tissue, the laser-induced photothermal injury was defined by the concentration of necrotic cell death. The grade of damage index determined by solving the Arrhenius integral quantified the concentration of necrotic cell death. At the last stage, the damage degree index threshold was set to >0.99 to assign irreversible thermal damage. Thus, it was assumed that the tissue coagulated completely in grids with a damage index >0.99. We estimated the thermally damaged area using these designated grids with a mesh size of 40 × 40 × 40 μm^3.

According to the map, the optimum laser irradiance for effective photothermal coagulation at sufficient depth was estimated to be between 16.4 and 31.8 W/cm^2 at the lowest scanning speed of 0.5 mm/second, and between 23.2 and 38.1 W/cm^2 at 1 mm/second in a single axis. The highest damaged area was calculated as 2.514 mm^2 for 0.5 mm/second at 61.7 W/cm^2. For scanning speeds above 1 mm/second with all laser powers, the calculated damage area was below 0.9 mm^2. Besides, it was estimated that 7.7 W/cm^2 laser irradiation at 1505 nm wavelength did not cause mucosal tissue damage for all scanning speeds.

Ex vivo tissue studies

We performed ex vivo tissue studies to examine the accuracy of the created guide map. The analysis included laser scanning in an ex vivo sheep esophagus model at four scanning speeds (0.5, 1.0, 1.5, and 2.0 mm/second) for seven different power settings (133, 150, 188, 220, 258, 284, and 309 mW) with the setup described in Figure 4. Laser powers corresponded to the irradiance of 16.4, 18.5, 23.2, 27.2, 31.9, 35.1, and 38.1 W/cm^2, respectively, for laser beam overlapping of >99% (i.e., surface area = R^2). The tissue was moistened with saline solution during the experiments to prevent the ex vivo sheep esophagus from drying out. Therefore, we assumed that the percentage of water did not change significantly, and the absorption coefficient of the tissue model was as constant as possible.

Figure 6A shows an example of mucosal whitening seen in gross anatomy, corresponding to thermally induced visual changes in tissue during 1 mm/second laser surface scanning. It has been hypothesized that coagulation necrosis causes such optically detectable changes in soft tissue. Note that the whitening thickness increased as a function of laser irradiance at fixed scanning speed. In comparison, it decreased relatively with increasing scanning speed at constant laser irradiance.

Samples collected at the end of the experiment were used for (1) light and (2) electron microscopy examinations to assess thermal damage to biological tissues further. Thus, in addition to observing whitening, the examination identified morphological changes in the context of evaluation response to photothermal coagulation therapy. The region of interest (magenta dashed line in Figure 6A) was sectioned from the paraffin-embedded sample blocks. Figure 6B,C shows cross-sectional histological images of H&E-stained tissue. The images were created by merging 27 images acquired at ×4 magnification in the brightfield and darkfield side by side. The primary difference between coagulated and uncoagulated areas was the hue. This difference was expressed separately by the esophageal layers.

In the brightfield image shown in Figure 6B, the epithelium became lighter while the connective tissue darkened if affected by photothermal coagulation. Indeed, the characterized morphological changes justified the color differences. Disruption of intercellular junction integrity, formation of intracellular spaces, and loss of cell contours gave the epithelium a transparentblurry appearance, resulting in a light pink manifestation. Starting with a laser power of 188 mW, epithelium dissociation from the basal lamina occurred, although the entire stratum corneum remained intact. On the other hand, a homogenized and opaque dark

pink-purple manifestation was obtained due to protein degradation in the connective tissue (lamina propria and submucosa). The darker color was probably caused by the high affinity of the free amino groups of the degraded proteins to eosin. As with surface whitening, structural changes at depth were proportionally associated with increased irradiance at constant beam diameter and decreased scanning speed (i.e., increased energy density, J/cm^2).

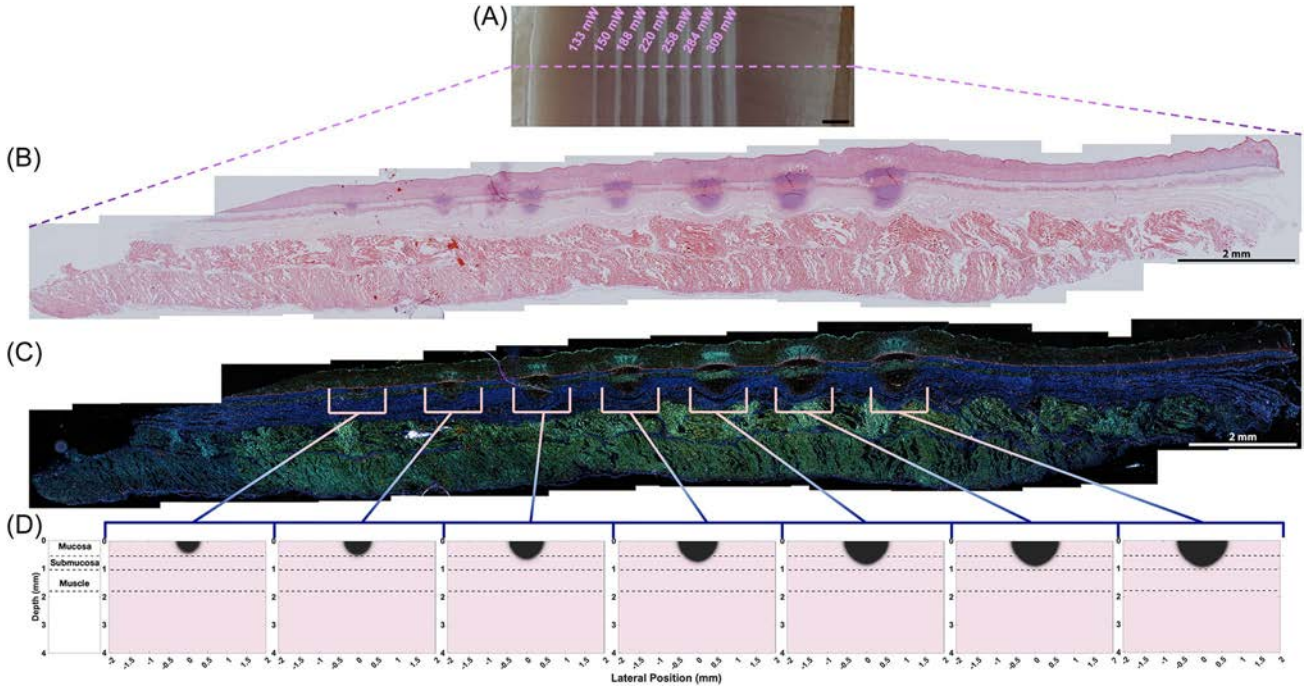


FIGURE 6 Photograph of visible thermal damage (mucosal whitening) after laser irradiation of sheep esophagus, ex vivo (A). Wavelength = 1505 nm, laser power = 133, 150, 188, 220, 258, 284, and 309 mW, surface scanning speed = 1 mm/second. Scale bar = 2 mm. Brightfield (B) and darkfield (C) microscopy images of ex vivo sheep esophagus stained with hematoxylin and eosin. The images show the merging of 27 images acquired at ×4 magnification (0.13 NA). Laser-induced thermal damage results, which are generated by the simulation engine for seven laser powers at a scanning speed of 1 mm/second (D). Tissue damage areas are marked with black contrast to light pink. Measured thermal injury depths were approximately 0.40, 0.66, 0.74, 0.82, 0.92, 1.00, and 1.08 mm. The corresponding simulation calculations were 0.36, 0.56, 0.68, 0.76, 0.84, 0.92, and 0.96 mm, respectively.

Darkfield microscopy images of the same H&Estained sample were obtained, as shown in Figure 6C. In darkfield imaging, which excludes unscattered light, the original hue of the stain, the thickness of the tissue sample, and the tissue density all affected the color perceived from the specimen. Dense pieces of tissue tended to reflect light more than refracting it and appear darker accordingly. In contrast, softer tissues refracted light more and shifted wavelengths significantly. As a result, a more distinct image can be acquired with different colors representing individual esophageal tissue layers; for example, the cell nucleus is in red, the muscle and cell membrane are in shades of green, and the connective tissue is in blue. The black appearance of the coagulated areas of the connective tissue in the lamina propria and submucosa layers can be explained by the tissue's relatively homogeneous and opaque formation.

Figure 6D shows the corresponding laser-induced thermal damage results of the simulation studies for seven laser powers at a scanning speed of 1 mm/second, and areas of tissue damage are marked with black. Although the tissue model was constructed as a single layer for the simulation study, the effect of photothermal coagulation on depth was estimated if the thicknesses of the esophageal tissue layers[9] were assigned accordingly. Damaged tissue depth was limited within the mucosa for 133 and 150 mW, and in the submucosa without affecting the muscle layer for 188, 220, 258, 284, and 309 mW, as seen in Figure 6—the depth and extent of tissue damage as a function of increasing power values correlated with experimental results. For example, thermal injury depths were measured approximately 0.40, 0.66, 0.74, 0.82, 0.92, 1.00, and 1.08 mm, while the corresponding simulation results were 0.36, 0.56, 0.68, 0.76, 0.84, 0.92, and 0.96 mm.

The darkfield microscopy image lacked structural details, although it increased contrast and distinguished individual tissue fragments. Therefore, we mathematically subtracted the brightfield microscope from the darkfield microscope to obtain a high-contrast image with morphological details. Figure 7 shows samples of the brightfield (A) and darkfield

(B) microscope images and the subtraction result (C) for 284 mW laser power (35.1 W/cm^2) at a laser scanning speed of 1 mm/second. With a color subtraction approach (e.g., magenta − red = blue), uncoagulated (i.e., pink in epithelial and muscularis mucosa, yellow-orange in lamina propria and submucosa) and coagulated tissue fragments (i.e., reddish in epithelial and muscularis mucosa, purple in lamina propria and submucosa), easily detectable to identify the photothermally affected area. Brightfield's limited damage analysis of H&E staining was insufficient

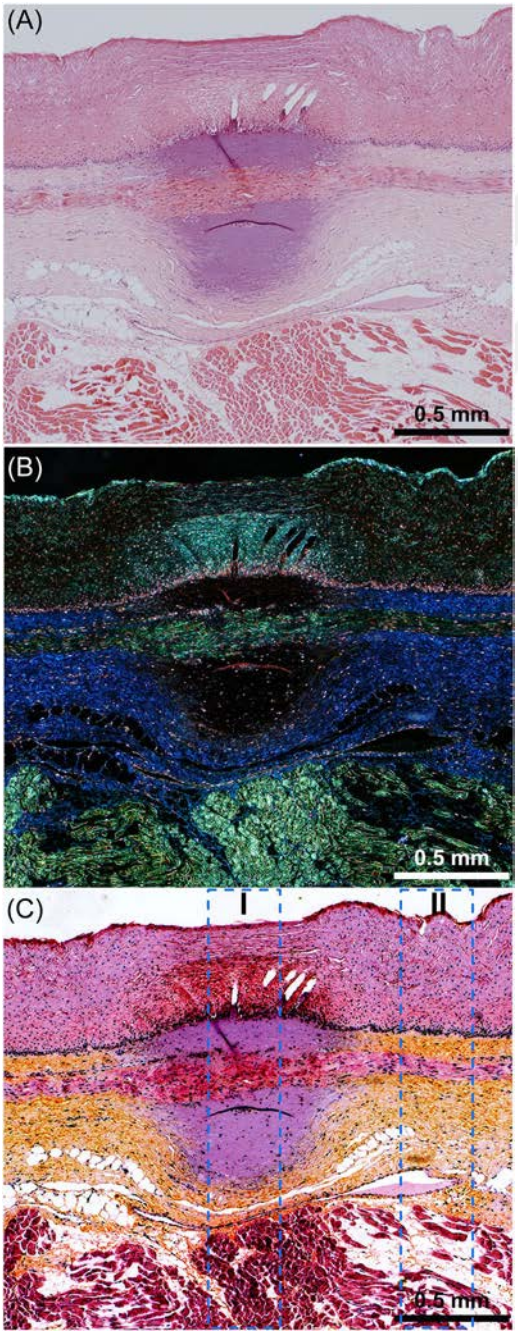


FIGURE 7 An example of highlighting contrast and morphological information of a thermally damaged area with the color subtraction approach. Samples of the brightfield (A) and darkfield (B) microscopy images of ex vivo sheep esophagus stained with hematoxylin and eosin and the color subtraction result (C) for 284 mW laser power (35.1 W/cm^2) at a laser scanning speed of 1 mm/second. Blue dashed rectangles indicate coagulated (I) and uncoagulated control (II) tissue sections further investigated under electron microscopy; ×4 magnification (0.13 NA). Scale bar = 0.5 mm.

to detect accurate margins but the most major thermal injury. Electron microscopy imaging was performed on unstained tissue samples from the consecutive slice to clearly understand and characterize the effect of photothermal coagulation at the cellular level. From the coagulated (Figure 7C,I) and control (i.e., uncoagulated) (Figure 7C,II) regions marked with blue dashed rectangles, a vertical portion of the gold-coated tissue sample was examined from the epithelial layer to the muscle.

Figure 8 shows the block-face scanning electron microscopy (Sigma 500l Zeiss) images acquired at ×1500 magnification from coagulated (I) and control (II) regions. Enlarged views of the circle area from the panels highlight the epithelium, basal lamina, lamina propria, muscularis mucosa, submucosa, and muscle layers and reveal changes compared to control.

After coagulation, the integrity of most of the cells was disrupted, and the cell nucleus or chromatin structure was lost in the epithelial layer. The basal lamina showed similar changes but was milder than the epithelium. Similarly, it was difficult to distinguish cell nuclei or chromatin structures within the basal lamina. Also, the cells were different in that they appeared cubically in uncoagulated tissue, elongated vertically after coagulation. Another profound change manifested in the lamina propria and submucosa, which usually have fibrillar, viscous, and less dense structures, transforming into homogeneous, dense, and opaque structures. Thickening of the muscularis mucosa was observed due to the separation of the muscle fibers forming the internal spaces after coagulation. Tear-like mechanical damage was observed at the intersection of the submucosa and muscle layers caused by high laser energy. The absence of any changes in the muscle layer indicated that the depth of laser-induced damage was limited to the submucosa at 35.1 J/cm^2 laser energy density.

Comparison of the simulation results with ex vivo tissue studies

Finally, we validated the guide map shown in Figure 5 with experimental thermally damaged area results and compared these results directly as a function of energy density (i.e., fluence, J/cm^2). Figure 9A shows a reconstructed version of Figure 5 with validation study results for an acceptable irradiance range and surface scanning speeds, given the limited resources for experimental studies. Discrete data sets

were interpolated for a seamless display while reconstructing the guide map with simulation and experimental results. The color bar indicates the interpolated laser-induced thermally damaged area.

As a next step, energy density was calculated to compare the simulation results with the experimental results more straightforwardly. Figure 9B demonstrates the logic followed in calculating the fluence to which the tissue is exposed during the laser scan. Energy density was directly proportional to laser power and inversely proportional to beam diameter (R) and surface scanning speed (ϑ). This correlation took the scan distance out of the equation with >99% beam overlapping, as in Figure 5.

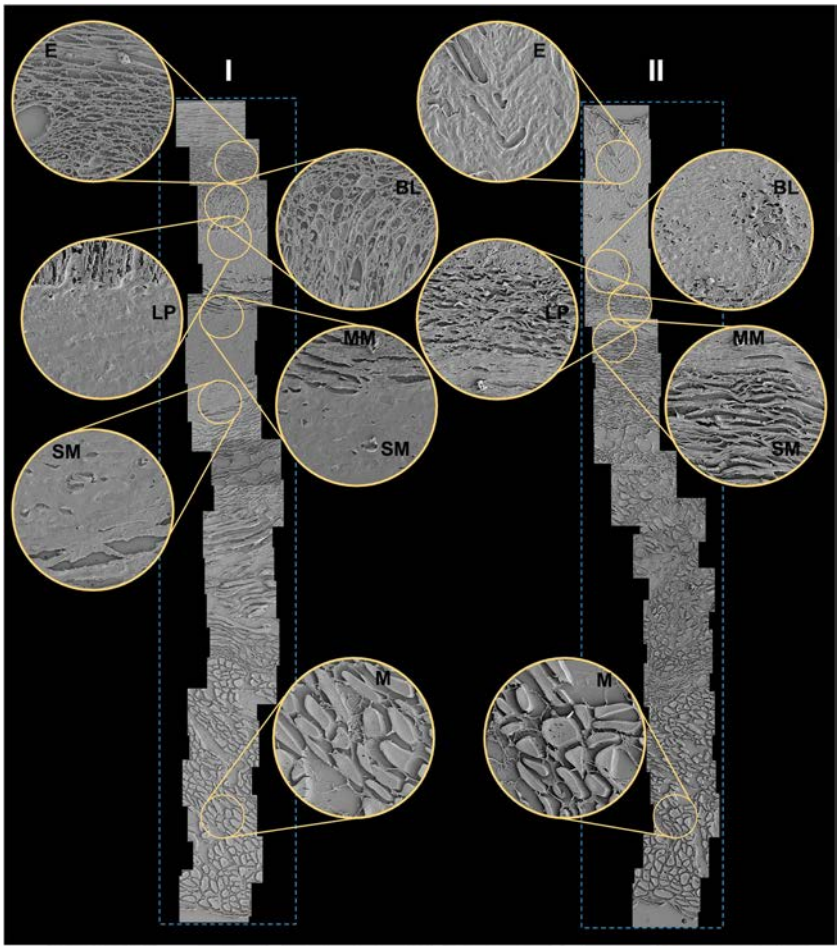


FIGURE 8 Images of coagulated (I) and uncoagulated control (II) tissue sections were further investigated under the block-face scanning electron microscopy. Enlarged views of the circle area from the panels highlight the epithelium (E), basal lamina (BL), lamina propria (LP), muscularis mucosa (MM), submucosa (SM), and muscle (M) layers and reveal changes compared to control in terms of morphological alterations at the cellular level.

The damaged area plot as a function of energy density in Figure 9C directly compares simulation and experiment results. As before, discrete data sets were interpolated for a seamless plot. The orange line shows the damaged area measured from cross-sectional histology samples obtained during laser scans at different scanning speeds ranging from 0.5 to 2 mm/second, and the orange region represents the standard deviation. The blue dashed line marks the simulation results.

The correlation of simulation and experiment results suggested that thermal damage and laser energy deposited into the tissue are directly related and define laser-induced photothermal coagulation. The results confirmed the onset of acute thermal injury symptoms at 10 J/cm^2. Although the fluctuation in the experimental results was obtained within a limited range (25–40 J/cm^2), the comparison study showed that the simulation engine generally provided estimates consistent with the ex vivo tissue model. It was determined that the standard deviation of the damaged area measurements increased relatively at an energy density of 60 J/cm^2 and above. It was evaluated that the increase in error in area measurements could be due to heat-induced mechanical damage at the intersection of the submucosa and muscle layers at the high laser energy. In Figure 8, for example, heat-induced mechanical damage between the submucosa and muscle layers was observed for laser powers of 284 and 309 mW, which was limiting in defining the area of thermal damage.

DISCUSSION

Laser-induced photothermal therapy has been used in gastroenterology studies since the late 1970s. In general, several laser types have been used, including argon laser at 514 nm, KTP-YAG laser at 532 nm, and Nd:YAG laser at

1064 nm.[29–31] Studies of the endoscopic laser-induced thermal method were mainly in the case of massive hemorrhage[32] and or the palliation of advanced, inoperable cancers of the upper and lower gastrointestinal tract.[33,34] The method has also played an important role in studies of superficial abnormal tissue treatment,[35,36] such as the management of Barrett's esophagus. Although endoscopic laser therapy has been explored to treat uncomplicated Barrett's mucosa, other thermal ablative methods such as RF ablation and argon plasma coagulation are widely preferred for this purpose. However, the multiple procedures of the contact RF ablation method limit the control of treatment depth. In the noncontact

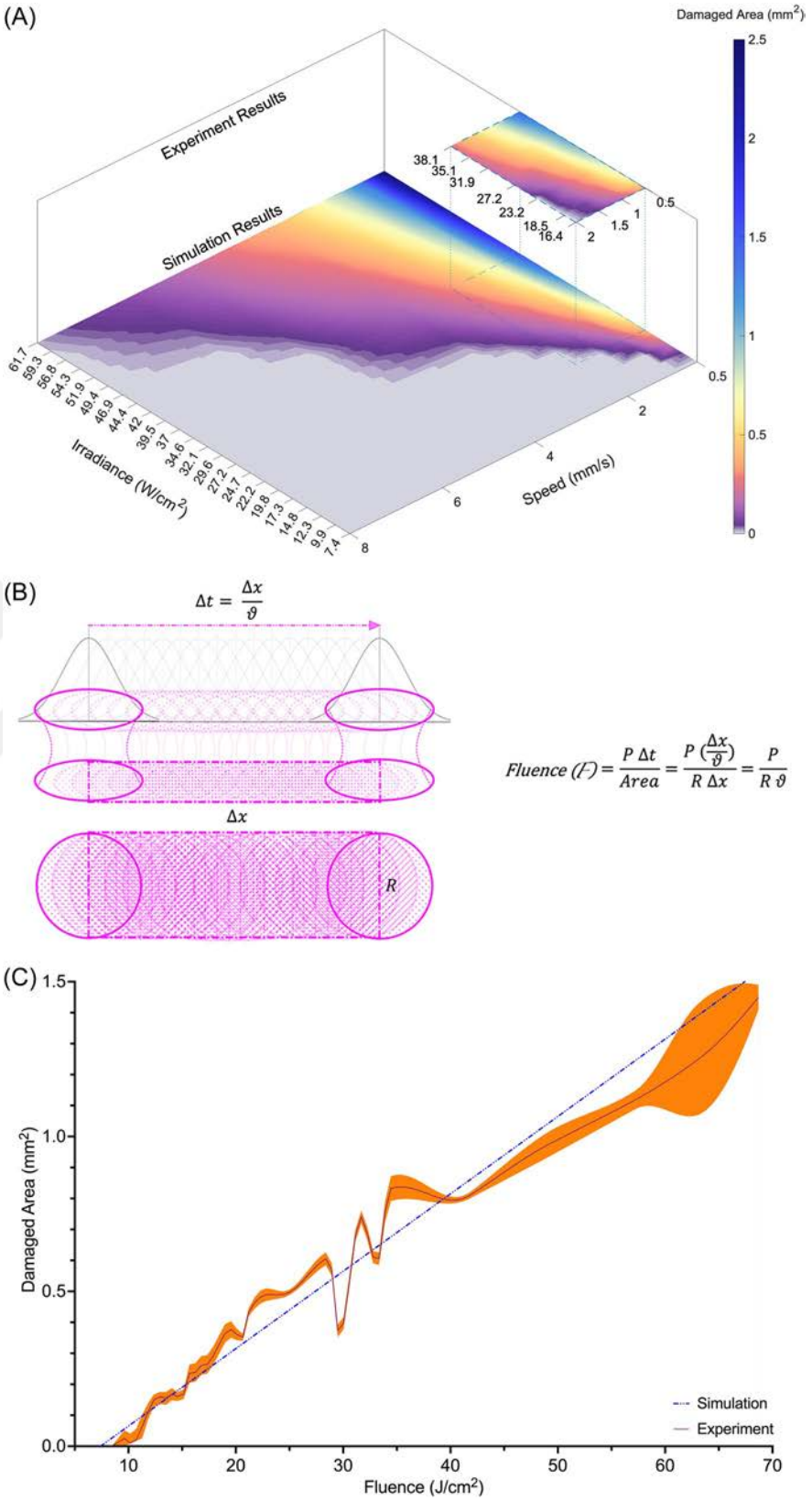


FIGURE 9 Reconstructed version of the guide map, including validation study results for an acceptable irradiance range and surface scanning speeds given the limited resources for experimental studies (A). Logic calculated the fluence to which the tissue is exposed during the laser scan (B). Energy density is directly proportional to laser power and inversely proportional to beam diameter (R) and surface scanning speed (ϑ). This correlation takes the scan distance from the equation with >99% beam overlap. A plot of the damaged area plot as a function of energy density to directly compares simulation (blue dashed line) and experiment results (C). The orange line shows the damaged area measured from crosssectional histology samples obtained at different scanning speeds ranging from 0.5 to 2 mm/second. The orange region represents the standard deviation. Discrete data sets are interpolated for a seamless plot.

argon plasma coagulation method, the coagulation depth depends on the distance between the probe and the target lesion and the application time. For these reasons, the experience and technique of the operator are very important for successful treatment in both methods. Besides, an unconfined depth of thermal effect produced can intrinsically lead to the risk of muscle scarring or even perforation, resulting in treatment failure.

Endoscopic management of superficial abnormal tissue remains a valid challenge. Even though laser therapy (i.e., laser-induced photothermal coagulation) has been gradually abandoned to treat superficial abnormal tissues,[37] it still has the potential for high safety and efficacy with minimal side effects. In addition, developments in optical imaging, fiber optical components, and diode laser technologies, which enable new probe designs, will bring laser therapy to the agenda more strongly again. The problem is that parameters such as laser irradiance and energy density are chosen quite empirically without adequate comparison with theory. In this context, it may be of interest to develop a numerical model simulating laser-induced photothermal mucosa coagulation.

This article presents a computer simulation engine that predicts laser-induced thermal damage by calculating the energy deposition of absorbed photons in the mucosa tissue layer. The developed computational model was able to map the area of irreversible thermal damage with accurate depth. The guide map simplified a matrix of treatment parameters (such as laser irradiance, beam diameter, and surface scanning speed) for successful photothermal mucosal therapy. In addition, the guide map created for a CW laser operated at 1505 nm in the ex vivo sheep model was verified. It has been noted that the theoretical and experimental data compared in terms of energy density are highly overlapping.

The various assumptions and limitations of the study should be discussed. First, the absorption and scattering coefficients and thermal properties of the tissue model were assumed to be constant over time during simulation studies. This assumption may be a reasonable and practical approximation for tissue-laser interaction that does not cause a considerable temperature variation. However, this can limit the simulation run, especially in the case of large thermal gradients where the tissue undergoes a phase change.

Second, soft tissue contains 70% water, and water can be the primary chromophore for soft tissues in the nearIR spectrum. Therefore, we hypothesized that the optical properties might not differ much between the layers of the esophagus. Nevertheless, these data may be needed to fine-tune the simulation model. However, the literature lacks optical and thermal properties for all layers of the esophagus.

Third, compared to pulsed lasers, the diode laser operating in CW mode over a telecommunications wavelength range stood out for its relative costeffectiveness and potential damage reduction in optical fiber evaluations. However, completing the validation work with a CW laser can be limiting. Thus, the work can be expanded by considering the pulsed laser case.

Fourth, the effect of surrounding uncoagulated tissue responses on healing was not considered in the model at this stage. Similarly, autolytic processes (i.e., postmortem degeneration and necrosis) in the ex vivo tissue were ignored in the study. Although the ex vivo tissue model provides relatively sufficient thermal response data, the notable importance of the in vivo animal model, which is beyond the scope of this study, is noted for future studies, including the analysis of acute and chronic thermal injury. Additionally, the effect of convective blood flows on mucosal coagulation can be analyzed by adding forced convection as a layer to the tissue model in simulation.

Finally, a more rigorous histological analysis of thermal damage to the esophagus is required for the in vivo animal model and a long-term study to determine the extent of progressive chronic damage. For histological analysis, nitroblue tetrazolium chloride staining, active for the cytoplasmic marker enzyme lactate dehydrogenase, can be used to provide high contrast between healthy tissue and laser-induced thermally damaged tissue.

CONCLUSION

The photothermal coagulation technique, which is included in the endoscopic thermal therapy method, can adequately respond to the needs of superficial treatments in the gastrointestinal tract. The potential of the photothermal coagulation technique can be reassessed with advances in optical imaging, fiber optic components, and diode laser technology at the telecommunication wavelength range. The presented results have demonstrated that the simulation engine can be a valuable tool to optimize coagulation variables to eradicate superficial abnormal tissue structures. Validation studies performed for a laser wavelength 1505 nm in ex vivo sheep esophagus support this assumption. The developed simulation engine can be enriched for different laser wavelengths combined with a suitable in vivo model for further studies.

ACKNOWLEDGMENTS

The authors thank Defne Ozturk (electron microscopy) and Ece Uzun (histology) from the IBG core facilities.

CONFLICT OF INTEREST

The authors declare no conflict of interest.

ORCID

Mervehttps://orcid.org/0000-0001-7101-3835
Nevin Ersoy http://orcid.org/0000-0002-6992-8451
Husnu A. Bagriyanik http://orcid.org/0000-0003-4064-7637
Serhat Tozburun http://orcid.org/0000-0002-4397-4011

REFERENCES

1. Liao D-H, Zhao J-B, Gregersen H. Gastrointestinal tract modelling in health and disease. World J Gastroenterol.

2009;15(2):169–76.
2. Chung C-S, Wang H-P. Screening for precancerous lesions of upper gastrointestinal tract: from the endoscopists' viewpoint. Gastroenterol Res Pract. 2013;2013:1–18.
3. Martinucci I, de Bortoli N, Russo S, Bertani L, Furnari M, Mokrowiecka A, et al. Barrett's esophagus in 2016: from pathophysiology to treatment. World J Gastrointest Pharmacol Ther. 2016;7(2):190–206.
4. Garud SS, Willingham FF, Cai Q. Diagnosis and management of Barrett's esophagus for the endoscopist. Therap Adv Gastroenterol. 2010;3(4):227–38.
5. Watson TJ. Endoscopic therapies for Barrett's neoplasia. J Thorac Dis. 2014;6(Suppl 3):298–308.
6. Shaheen NJ, Sharma P, Overholt BF, Wolfsen HC, Sampliner RE, Wang KK, et al. Radiofrequency ablation in Barrett's esophagus with dysplasia. N Engl J Med. 2009;360(22):2277–88.
7. Johanns W, Luis W, Janssen J, Kahl S, Greiner L. Argon plasma coagulation (APC) in gastroenterology: experimental and clinical experiences. Eur J Gastroenterol Hepatol. 1997;9(6):581–7.
8. Kallam A, Alsop BR, Sharma P. Limitations of endoscopic ablation in Barrett's esophagus. Expert Rev Gastroenterol Hepatol. 2015;9(4):487–96.
9. Hohmannohmann M, Lengenfelder B, Kanawade R, Klämpfl F, Douplik A, Albrecht H. Measurement of optical properties of pig esophagus by using a modified spectrometer set-up. J Biophotonics. 2018;11(1):e201600187.
10. Ribeiro SR, Pinto Júnior PE Jr, Miranda AC, Bromberg SH, Lopasso FP, Irya KSH. Weight loss and morphometric study of intestinal mucosa in rats after massive intestinal resection: influence of a glutamine-enriched diet. Rev Hosp Clin Fac Med Sao Paulo. 2004;59(6):349–56.
11. Schena E, Saccomandi P, Fong Y. Review laser ablation for cancer: past, present and future. J Funct Biomater. 2017;8(2):1–15.
12. Marmur ES, Schmults CD, Goldberg DJ. A review of laser and photodynamic therapy for the treatment of nonmelanoma skin cancer. Dermatol Surg. 2004;30:264–71.
13. Lee H, Lee Y, Song C, Cho HR, Ghaffari R, Choi TK, et al. An endoscope with integrated transparent bioelectronics and theranostic nanoparticles for colon cancer treatment. Nat Commun. 2015;6:1–10.
14. Dix T, Barr H. Photothermal ablation of metaplastic columnarlined (Barrett's) esophagus, experimental studies for safe endoscopic laser therapy. Proc SPIE. 1996;2922:2750280.
15. Salo JA, Salminen JT, Kiviluoto TA, Nemlander AT, Rämö OJ, Färkkilä MA, et al. Treatment of Barrett's esophagus by endoscopic laser ablation and antireflux surgery. Ann Surg. 1998;227(1):40–4.
16. Bowers SP, Mattar SG, Waring PJ, Galloway K, Nasir A, Pascal R, et al. KTP laser ablation of Barrett's esophagus after anti-reflux surgery results in long-term loss of intestinal metaplasia. potassium-titanyl-phosphate. Surg Endosc. 2003;17(1):49–54.
17. Wilson BC, Adam G. A Monte Carlo model for the absorption and flux distributions of light in tissue. Med Phys. 1983;10(6):824–30.
18. Wang LH, Jacques SL, Zheng Z. MCML—Monte Carlo modeling of light transport in multi-layered tissues. Comput Methods Programs Biomed. 1995;47(2):131–46.
19. Pennes HH. Analysis of tissue and arterial blood temperature in the resting human forearm. J Appl Phys. 1948;1:93–102.
20. Henriques FC, Moritz AR. Studies of thermal injury: I. The conduction of heat to and through skin and the temperatures attained therein. A theoretical and an experimental investigation. Am J Pathol. 1947;23(4):531–49.
21. Bashkatov AN, Genina EA, Kochubey VI, Gavrilova AA, Kapralov SV, Grishaev VA, et al. Optical properties of human stomach mucosa in the spectral range from 400 to 2000 nm: prognosis for gastroenterology. Med Laser Appl. 2007;22(2):95–104.
22. Collins CM, Smith MB, Turner R. Model of local temperature changes in brain upon functional activation. J Appl Physiol. 2004;97:2051–55.
23. Pearce JA. Relationship between Arrhenius models of thermal damage and the CEM 43 thermal dose. Proc. SPIE 7181, Energybased Treatment of Tissue and Assessment V (Ed: Ryan TP), 2009.
24. Liu JB, Miller LS, Goldberg BB, Feld RI, Alexander AA, Needleman L, et al. Transnasal US of the esophagus: preliminary morphologic and function studies. Radiology. 1992;184(3):721–27.
25. Taniguchi DK, Martin RW, Trowers EA, Silverstein FE. Simultaneous M-mode echoesophagram and manometry in the sheep esophagus. Gastrointest Endosc. 1995;41(6):582–6.
26. Glanzmann TM, Zellweger MP, Borle F, Conde R, Radu A, Ballini JP, et al. Assessment of a sheep animal model to optimise photodynamic therapy in the oesophagus. Lasers Surg Med. 2009;41(9):643–52.
27. Radu A, Conde R, Fontolliet C, Wagnieres G, Van den Bergh H, Monnier P. Mucosal ablation with photodynamic therapy in the esophagus: optimization of light dosimetry in the sheep model. Gastrointest Endosc. 2003;57(7):897–905.
28. Hale GM, Querry MR. Optical constants of water in the 200 nm to 200 μm wavelength region. Appl Opt. 1973;12(3):555–63.
29. Fleischer D. Endoscopic laser therapy for gastrointestinal disease. Arch Intern Med. 1984;144(6):1225–30.
30. Hunter JG. Endoscopic laser applications in the gastrointestinal tract. Surg Clin North Am. 1989;69(6):1147–66.
31. Schwesinger WH. Laser treatment of esophageal and gastric lesions. Surg Clin North Am. 1992;72(3):581–95.
32. Swain CP. Laser therapy for gastrointestinal bleeding. Gastrointest Endosc Clin N Am. 1997;7(4):611–39.
33. Brunetaud JM, Maunoury V, Cochelard D. Lasers in digestive endoscopy. J Biomed Opt. 1997;2(1):42–52.
34. Courtney ED, Raja A, Leicester RJ. Eight years experience of high-powered endoscopic diode laser therapy for palliation of colorectal carcinoma. Dis Colon Rectum. 2005;48(4):845–50.
35. Weston AP. Use of lasers in Barrett's esophagus. Gastrointest Endosc Clin N Am. 2003;13(3):467–81.
36. Polese L, Angriman I, Scarpa M, Pagano D, Parente P, Erroi F, et al. Diode laser treatment of Barrett's esophagus: long-term results. Lasers Med Sci. 2011;26(2):223–8.
37. Rouphael C, Anil Kumar M, Sanaka MR, Thota PN. Indications, contraindications and limitations of endoscopic therapy for Barrett's esophagus and early esophageal adenocarcinoma. Therap Adv Gastroenterol. 2020;13:1756284820924209.

How to cite this article: Turker-Burhan M, Ersoy N, Bagriyanik HA, Tozburun S. Guide mapping for effective superficial photothermal coagulation of the esophagus using computer simulations with ex vivo sheep model validation study. Lasers Surg Med. 2022;54:1116–1129. https://doi.org/10.1002/lsm.23595

Turkish Journal of Electrical Engineering and Computer Sciences

Volume 30 | Number 7 Article 9

1-1-2022

Monte-Carlo method based simulations for photothermal mucosa coagulation with accurate depth limits

MERVE TÜRKER BURHAN

SERHAT TOZBURUN

Follow this and additional works at: https://journals.tubitak.gov.tr/elektrik

 Part of the Computer Engineering Commons, Computer Sciences Commons, and the Electrical and Computer Engineering Commons

Recommended Citation
BURHAN, MERVE TÜRKER and TOZBURUN, SERHAT (2022) "Monte-Carlo method based simulations for photothermal mucosa coagulation with accurate depth limits," Turkish Journal of Electrical Engineering and Computer Sciences: Vol. 30: No. 7, Article 9. https://doi.org/10.55730/1300-0632.3958 Available at: https://journals.tubitak.gov.tr/elektrik/vol30/iss7/9

This Article is brought to you for free and open access by TÜBİTAK Academic Journals. It has been accepted for inclusion in Turkish Journal of Electrical Engineering and Computer Sciences by an authorized editor of TÜBİTAK Academic Journals. For more information, please contact academic.publications@tubitak.gov.tr.

TÜBİTAK

Turkish Journal of Electrical Engineering & Computer Sciences

http://journals.tubitak.gov.tr/elektrik/

Research Article

Turk J Elec Eng & Comp Sci
(2022) 30: 2605 – 2616
© TÜBİTAK
doi:10.55730/1300-0632.3958

Monte-Carlo method based simulations for photothermal mucosa coagulation with accurate depth limits

Merve TÜRKER-BURHAN[1,2,1], **Serhat TOZBURUN**[1,2,3]
[1]İzmir Biomedicine and Genome Center, İzmir, Turkey
[2]İzmir International Biomedicine and Genome Institute, Dokuz Eylül University, İzmir, Turkey
[3]Department of Biophysics, Faculty of Medicine, Dokuz Eylül University, İzmir, Turkey

Received: 08.06.2022 • **Accepted/Published Online:** 08.10.2022 • **Final Version:** 28.11.2022

Abstract: The mucosa layer, the innermost layer of the gastrointestinal (GI) system, is of great importance in carcinogenesis since most cancerous tissues occur as superficial lesions. Although various treatment strategies exist, the main difficulty in eradicating lesions is unintentional damage to healthy tissues with the uncontrolled depth of treatment. This study proposes a computer modeling approach for simulating depth-resolved photothermal (laser) mucosal coagulation therapy. Computer modeling mimics the thermal dynamics of mucosal tissue to characterize the total heat energy required for successful superficial coagulation, which can be controlled by the scan rate, scan time, output power, and beam diameter of the applied laser. It consists of three steps: 1) Monte Carlo simulation to generate a laser energy distribution profile. 2) Heat transfer simulation to calculate the resulting tissue temperature. 3) Thermal damage estimation based on the calculated dead cell ratio. This computer modeling was performed for a laser wavelength of 1500 nm. Transient temperature profiles and a corresponding thermal damage map were generated as functions of laser scanning speed, power, and beam diameter. The guide map estimates that mucosal coagulation can be achieved with the accurate depth limits at 1500 nm laser wavelength, 1 mm beam diameter, 0.33-0.43 W/cm^2 irradiation range, and 1-3 mm/s scanning speeds. This computing approach may hold promise in determining optimal therapy parameters for depth-resolved adequate coagulation in a single session with further development.

Key words: Computer modeling, Monte-Carlo method, photothermal mucosal coagulation, mucosal lesions

1. Introduction

The gastrointestinal (GI) tract consists of four layers of tissue: mucosa, submucosa, muscularis externa, and serosa. The innermost layer, the mucosa, is first exposed to the lumen, making it susceptible to lesion formation. Precancerous lesions in the mucosa layer can progress to deeper layers and cause esophageal cancer, stomach cancer, colon cancer, and rectal cancer [1]. Therefore, the mucosa layer is highly critical for malignancies of the GI tract.

Various treatment strategies are available for mucosal lesions [2–4]. Ablation therapy, a minimally invasive procedure based on thermal injury, is the preferred treatment strategy to remove the target lesion. However, the constant treatment depth provided by commonly used ablation techniques such as argon plasma coagulation, multipolar electrocoagulation, cryoablation, and radiofrequency ablation cannot accommodate mucosal thickness ranging from 0.4 to 1.0 mm in different parts of the GI tract [5–7]. This insufficient depth of therapy can lead to under or overtreatment.

As an alternative ablative therapy, photothermal (i.e. laser) coagulation causes denaturation of proteins and even sudden cell death due to high temperature from heat generation [8–16]. Depending on the wavelength and operating mode of the laser and the tissue type, the heat accumulation in the tissue may differ. The measure of depth at which light can pass through tissue defines the optical penetration depth (OPD). The wavelengthdependent optical properties of tissue,

[1] Correspondence: merve.turker217@ogr.deu.edu.tr

This work is licensed under a Creative Commons Attribution 4.0 International License.

such as absorption coefficient, scattering coefficient, anisotropy factor, and refractive index, define light penetration into the tissue.

In this context, laser-tissue interactions can be predicted by modeling light propagation in a homogeneous medium. As a common practice, the Monte-Carlo method has been used for years to analyze the interaction of light with biological tissue [17–19].

It uses a statistical approach to track random walking steps that models the propagation of light subjected to scattering and absorption events in a single or multilayer tissue sample. The step size is randomly sampled based on the optical properties of the tissue model. With each step (i.e. scattering), the unit weight of the photon decreases in proportion to its absorption probability. The scattering event is renewed until the emitted photon is completely absorbed (loss in unit weight). The iteration is for the total number of photons (Figure 1, [20]). As a result, a three-dimensional probability distribution of laser energy based on absorption and scattering events for tissue is obtained. This laser energy is the heat source that can be transferred and causes a temperature increase in the tissue.

$$\rho C \frac{\partial T}{\partial t} = k\nabla^2 T_{(x,y,z,t)} + Q \tag{1}$$

Heat transfer equation (1) describes heat transfer by calculating transient energy and temperature in a unit of time and space [21] regarding thermal properties of tissue; ρ is the density, C is the specific heat, and k is the thermal conductivity. $T_{(x,y,z,t)}$ is the resulting tissue temperature obtained in functions of time and space. Q represents the heat source of the laser irradiation (computed by the Monte-Carlo method).

$$\Omega_{(x,y,z,t)} = \xi \int_0^{\tau} e^{\frac{-E_a}{RT_{(x,y,z,t)}}} dt \tag{2}$$

$$P_{dead\ cell\ (\%)} = 100(1 - e^{-\Omega_{(x,y,z,t)}}) \tag{3}$$

The rapid increase in temperature associated with the accumulated heat energy primarily results in cell death. Therefore, the photothermal effect of the laser on the tissue can be expressed as the degree of thermal damage, Ω, using the Arrhenius integral (2, [22]) based on the thermal kinetics of the tissue. ξ is the frequency factor, E_a is the activation energy of the transformation, τ is the total heating time, R is the universal gas constant, and T is the absolute temperature of the tissue in Kelvin. The percentage of dead (necrotic) cells ($P_{deadcell(\%)}$) can be derived from Equation 3 for a given time and space. Overall, the calculated thermal damage can define the extent of photothermal coagulation.

This study presents a computer modeling approach that combines the Monte-Carlo method and aforementioned mathematical models to mimic mucosal tissue's thermal dynamics/responses to characterize the total heat energy required for successful coagulation with accurate depth limits (i.e. well-confined photothermal coagulation). Since the simulation parameters of the applied laser, such as scan speed, scan time, irradiance (W/cm^2) and laser driving modes (e.g., continuous or pulsed) show a large matrix of variables that must be op-

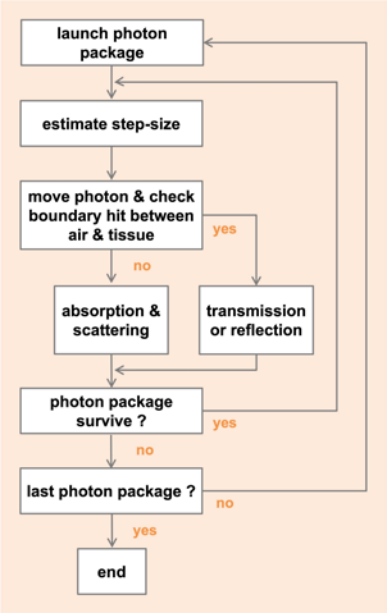


Figure 1. Block diagram of Monte-Carlo method.

timized to perform a safe, adequate, and efficient treatment; this study may give an idea about the photothermal coagulation of mucosa tissue.

2. Materials and methods

The computer modeling approach consisted of three interrelated steps (Figure 2). The first step was Monte-Carlo simulation to determine the distribution of photons in tissue as functions of wavelength-dependent refractive index, absorption, scattering, and anisotropy coefficients. The second step used the photon distribution profile as the heat source in a time-dependent heat diffusion model to calculate the temperature profile in the tissue over time. As the final step, thermal damage was calculated using the temperature-based Arrhenius integral to generate the damage index, followed by a normalization factor representing the fraction of cell necrosis in a given volume.

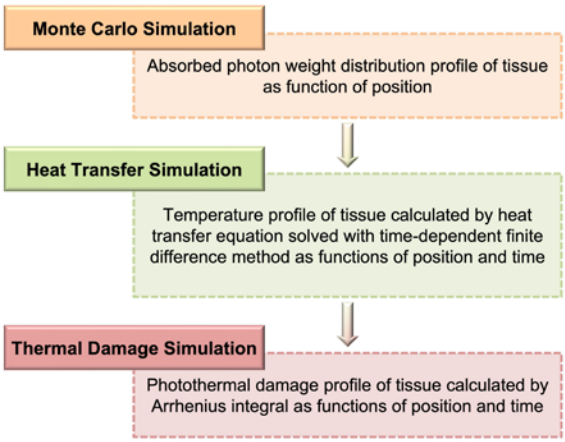


Figure 2. Three step computer modeling approach.

2.1. Computing engine

2.1.1. Monte-Carlo method

Each layer constituting the target tissue was defined in a cylindrical coordinate system (r, z) with a thickness (t, mm) and wavelength-dependent variables, including refractive index (n), scattering coefficient (μs, cm^{-1}), absorption coefficient (μa, cm^{-1}) and anisotropy factor (g). The scattering coefficient and the absorption coefficient were used to describe the probability of scattering and absorption events in one step. The anisotropy factor determined the first-order probability distribution of the scattering angles. The total number of photons per unit weight was 1 million to have a correct path in the simulation and increase spatial resolution.

The weight distribution of the photon absorbed in the tissue model was calculated using the source code available in Ref. [20] with the indicated variables used as input data. The numerical results were then combined with a Gaussian beam profile (convolution), and the value of the absorbed photon weight was numerically normalized. A collimated laser beam was produced during this process, including interpolation to the Cartesian coordinate system (x, y, z). The oriented Gaussian profile was converted to a fractional heat source (J/s/mm^3 or W/mm^3) based on the absorbed photon weight distribution, laser power per unit volume, and unit time
(1 J = 1 W × 1 s).

The tissue model was defined in a 600 × 600 × 18 uniform 3D grid system with a grid size of 100 μm across all dimensions corresponding to 60 mm (x-axis) × 60 mm (y-axis) × 1.8 mm (z-axis, depth). The physical dimensions of the modeled tissue, especially the mucosal tissue thickness, have been determined in the literature by considering the size of the sheep esophagus [23, 24]. Tissue was considered homogenous; therefore, optical parameters of mucosa tissue at 1500 nm wavelength were defined as the same for each grid (Table 1).

2.1.2. Heat transfer

Table 2 summarizes the thermal properties compiled from the literature. The heat transfer law governed the diffusion of heat produced by laser radiation. Heat transfer equation (1) was employed in this context. This equation was solved using the time-dependent finite difference method (FDM) for a unit of time. The sliding algorithm was created by interpolating the initial condition and using the time step solution as an initial condition for the following solution over time. The temperature tracking solver used object-oriented programming techniques to complete a data structure representing a depth marker that moves across the tissue.
A custom class of markers was employed to store the trajectory and temperature along the time.

Table 1. Optical properties of mucosa tissue [25].

Absorption coefficient, cm^{-1}	1 2
Scattering coefficient, cm^{-1}	2 3
Anisotropy factor, (g)	
Refractive index, (n)	

Table 2. Thermal properties of mucosa tissue [26].

Thermal conductivity, W/m$\cdot$C	0.527
Specific heat, J/kg$\cdot$C	3720
Density, kg/m^3	1126

The time step in the heat transfer equation was assigned values such as Δt = 3 ms, 6 ms, 9 ms for the temperature's time- and space-dependent solutions. In other words, the temperature solution was shifted in the x-

direction after each time step to mimic the uniaxial sliding of the light source through the tissue at a constant velocity. Thus, the spatial coordinate of the simulated volume became $x_{new} = x_{reference} + vx$ with each new step, showing the temperature-time trace of a fixed location in the moving frame. Transient temperature solutions were obtained for laser irradiation at the same peak power in both pulsed and continuous wave modes. The period was set to 60 ms with a 50% duty cycle (i.e. a pulse width of 30 ms).

2.1.3. Photothermal damage

The thermal damage simulation relied on the Arrhenius integral (2) to calculate laser-induced thermal damage to the target tissue. The thermal kinetic parameters of the tissue (Table 3) were used to determine the morphological changes in the tissue related to the thermal degradation of proteins. The damage index (i.e. the extent of the damage) was normalized to produce the fraction of surviving cells in each volume. Regarding protein degradation (coagulation) of biological constructs per unit volume, the index corresponded to a concentration of 63% to 99% necrotic cells in the range of 1 to 4.6. For damage estimates, $60 \circ C$ was used as the critical temperature, and $\Omega = 3.9$ (98% necrotic cell concentration) was used as the threshold value for protein degradation per unit volume of biological constructs. Unit volumes with an index greater than or equal to 3.9 were considered damaged tissue.

Table 3. Thermal kinetics of mucosa tissue [27].

Frequency factor, s-1	1.3×10^{95}
Activation energy, J/mol	6.4×10^{5}
Universal gas constant, J/molK	8.314

2.2. Creating the guide map

Figure 3 shows a block diagram of the computer modeling developed for simulation studies of laser scanning induced coagulation on a mucosal tissue model. The optical and thermal properties of the tissue defined for the next three steps were utilized in the relevant simulation sections. A customized sliding algorithm to mimic laser scanning advanced the computations in every step. As the results of the computer modeling approach, the temperature profile of the tissue and the photothermal damage profile were obtained as functions of space and time. The initial tissue temperature was set to $37 \circ C$.

Figure 4 presents the range of laser scanning speed and beam diameter to generate a temperature and corresponding thermal damage map. The black dashed lines show the diameters of the laser beam ranging from 1 mm to 3 mm, while the colored bar shows a range of scanning speeds and directions of motion along the tissue surface (x-axis). In addition, the laser output power was between 20 mW and 500 mW.

In addition to the single scan along the x-axis and the method of averaging the highest tissue temperatures obtained during the scan, the listed procedures were followed to calculate the thermal damage index and rate, respectively. (i) The temperature measurement time step used in each x-axis scan simulation performed at different speeds was determined. Table 4 lists the time steps used for each surface scan rate. (ii) The calculated peak tissue temperature at the end of each temperature measurement time step was recorded. (iii) Based on Equation 2 (thermal damage index) using the recorded peak temperature as input, the thermal damage rate was calculated along a single scanline (Equation 3).

3. Results

Figure 5 shows an example of a transient solution of the heat transfer equation, which describes tissue temperature as a function of depth and lateral positions over time. Accordingly, representative surface and section temperature profiles were selected for the last time point of the x-axis scan. In this simulation, the scan (slide)

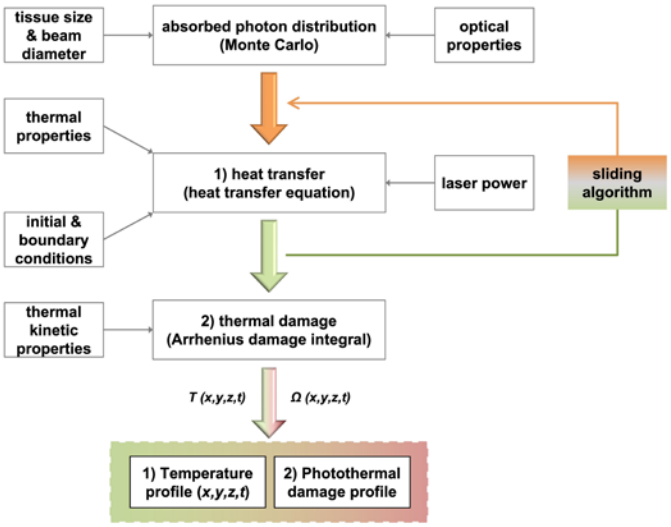


Figure 3. Block diagram of the computer modeling.

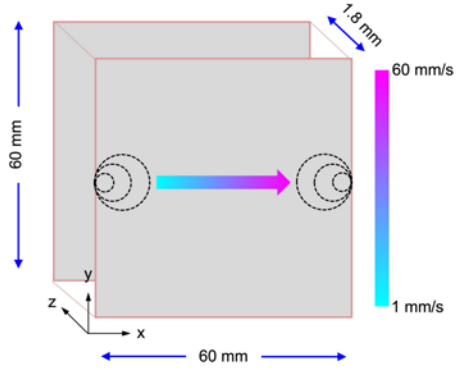


Figure 4. Tissue model used in simulation studies. The black dashed lines indicate different diameters (1 mm-3 mm) of the laser beam, while the color bar indicates a range of scanning speed and direction of travel along the mucosa surface (x-axis).

Table 4. X-axis scanning speeds and the corresponding temperature-calculation time step.

Speed, mm/s	Temperature-calculation time step, s
1	0.06
2	0.03
3	0.02
5;6	0.012
8	0.009
10;12	0.006

30;60	0.003

speed in the x-axis was set to 1 mm/s, corresponding to a temperature calculation time step of 0.06 s. The total scan time was calculated as 59 s. Moreover, the laser beam diameter was 1 mm, while the laser power was defined as 120 mW. These values correspond to an irradiance of 15.28 W/cm^2 at a point, so considering the overlapping Gaussian beam series throughout the entire scan, the laser energy density (i.e. fluence) to which the tissue is exposed was calculated as approximately 12 J/cm^2 (Figure 5 A) for continuous-wave mode and
6 J/cm^2 for pulsed mode (30 ms pulse width with a 50% duty cycle, Figure 5 B) by Equation 4 as follows,

$$Fluence = \frac{P}{Rv} \tag{4}$$

where P is power (W), R beam diameter (mm) and v scanning speed (mm/s).

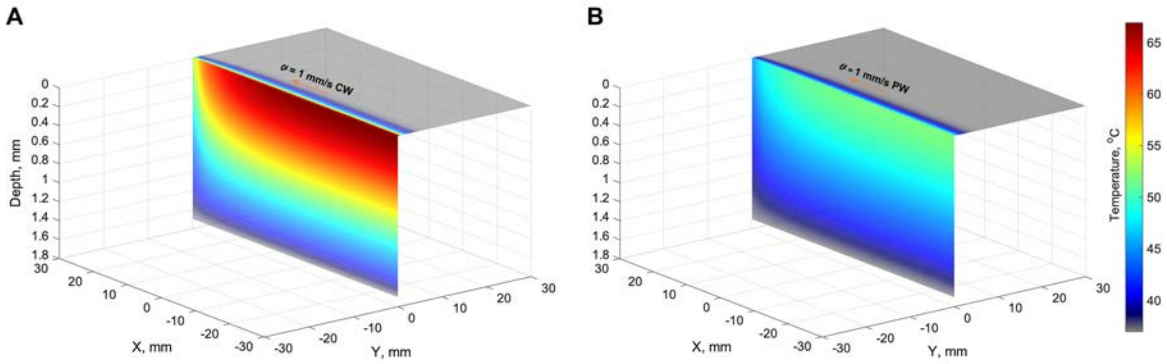


Figure 5. Surface and cross-sectional frames of the transient tissue temperature profile for the surface scanning speed of 1 mm/s during 59 s with a laser beam diameter of 1 mm and 120 mW laser power. Continuous wave mode (A), pulsed mode (B).

The maximum tissue temperature reached during this x-axis line scan was calculated as 66.98 ◦C for continuous wave laser and 51.87 ◦C for the pulsed laser, respectively. For continuous wave laser application, tissue layers deeper than 1 mm were predicted to remain below the critical temperature required for protein degradation. Considering the depth-resolved photothermal mucosal coagulation treatment, it was consistent with the 0.4 mm to 1 mm thick sheep mucosal layer.

Similar simulations were repeated for different scanning speeds, laser diameters, and laser powers, as shown in the transient tissue temperature profile example. A matrix map, created with the highest tissue temperatures reached during line scanning, was produced with that varied scan speed, beam diameter, and laser power. Figure 6 shows the generated map showing a comprehensive combination of laser irradiance (laser power and beam diameter) and scan speed (energy density = laser power/beam diameter/scan speed). The Arrhenius integral model calculated a theoretical damage index at each laser power varying in step size of 20 mW for a combination of beam diameter and scanning speed. In all damage calculations, the critical damage threshold ratio was 98 % (damage index, $\Omega_{(x,y,z,t)} = 3.9$). Since the critical temperature was determined as 60 ◦C, the frequency factor (1.3×10^{95} s^{-1}) and activation energy (6.04×10^5 J/mol) coefficients presented by Diller et al. [27] were used in the calculations, as shown in Table 3. The peak tissue temperatures obtained at the end of the x-axis scan and the thermal damage indices for the single scan time were estimated. In Figure 6, the solid

white line defined the limit of coagulation parameters that resulted in a thermal damage index equal to or higher than the threshold ($\Omega = 3.9$). Y axes on the map are set in logarithmic scale.

Figure 7 shows the longitudinal damaged areas calculated as functions of irradiance and scan rates for different beam diameters of the laser operated in continuous wave mode. The 0.23 W/cm^2 laser irradiation corresponded to an energy density range of 1.14 J/cm^2 and 13.77 J/cm^2 for scanning speeds from 1 mm/s to 12 mm/s with a beam diameter of 1 mm. In this case, the areas with longitudinal damage to the tissue were between 0.02 cm^2 and 0.59 cm^2. We also estimated the laser irradiance required to generate a 0.02 cm^2 damaged area in tissue to be 0.4 W/cm^2 at 30 mm/s and 0.63 W/cm^2 at 60 mm/s. The same scan rates and 2-mm beam diameter required higher laser irradiation (i.e. > 0.3 W/cm^2 corresponding to a higher energy density range of 1.52 J/cm^2 and 16.4 J/cm^2) to produce the same amount of damaged mucosal areas. Rapid scanning speeds ($\geqslant$ 30 mm/s) did not cause thermal damage at laser irradiation of 0.4 W/cm^2 per laser beam diameter. The same laser irradiance caused more extensive tissue damage at a slower scan rate. However, the exposure time of the tissue to the laser irradiation decreased in parallel with the increase in scanning speed. This reduction increased laser power to keep the energy level to which the tissue was exposed. In general, laser irradiance between 0.33 W/cm^2 and 0.44 W/cm^2 (for 1 mm beam diameter) provided a sufficient thermal response in the 1 to 3 mm/s range to achieve well-circumscribed longitudinal coagulation in mucosal tissue.

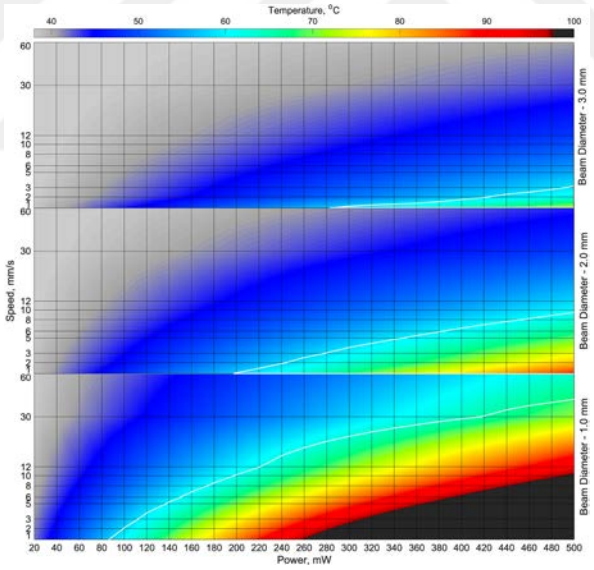


Figure 6. A map of the predicted peak mucosal temperatures during scanning on the x-axis as the functions of both laser beam diameter and laser power for different scanning speeds. The solid white line shows 98% proportional thermal damage calculated based on 60 °C critical temperature from laser irradiation. Y axes on the map are set in logarithmic scale.

Figure 8 shows the estimated results of scanning laser coagulation in pulsed mode with the same peak power as in continuous wave. Figure 8 A presents a map generated by the logic mentioned above in Figure 6 for a beam diameter of 1 mm. As expected, the 50% duty cycle of the pulsed laser reduced the energy accumulated in the tissue; therefore, the predicted temperature was lower than that of the continuous wave laser with the same peak power. Figure 8 B shows the corresponding longitudinal damaged areas calculated as a function of laser irradiance. Laser irradiance is doubled in pulsed mode with a 50% laser exposure duty cycle compared to continuous wave mode. For example, the irradiance

corresponding to energy density range of 1.14 - 13.77 J/cm^2 (between 1 mm/s and 12 mm/s) was 0.46 W/cm^2. Also, the estimated laser irradiance required to generate an area of damaged tissue of 0.02 cm^2 at 30 mm/s was 0.63 W/cm^2, calculated for 60 mm/s for continuous wave laser.

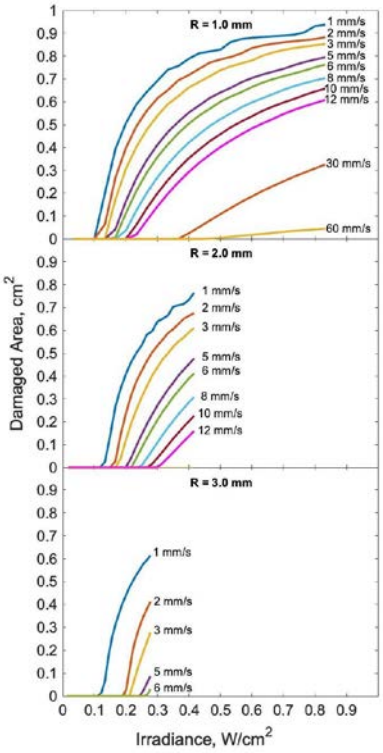


Figure 7. The graphs of damaged area as functions of scanning speed and irradiance for 1 mm, 2 mm and 3 mm of beam diameters of continuous wave laser application.

4. Discussion and conclusion

A computer modeling approach was developed to simulate photothermal mucosal coagulation with accurate depth limits by defining optimal parameters, including laser scanning speed, laser beam diameter, and laser power. Thus, a map was produced that simplifies a complex parameter matrix. This approach was based on three independent models: the Monte-Carlo method, heat transfer equation, and the Arrhenius damage integral. The steps were correlated using the output of one as the input of the other. The photon weight distribution estimated by the Monte-Carlo method was used as a heat source in the heat transfer process to calculate the laser-induced temperature response of the mucosa model. The sliding of the laser beam over the tissue was simulated by redefining the heat source coordinate for each time step and calculating the transient temperature profile in the tissue. The thermal damage index was calculated for each unit cell in the tissue-defining grid system to estimate the degree of coagulation based on temperature distribution over time and exposure time using the thermal kinetic coefficients of the tissue. The mucosa layer's optical and thermal properties and kinetic coefficients were compiled from the literature and were accepted as the same in all tissue layers.

Based on the temperature and thermal damage profiles calculated with the developed computer modeling approach, we correlated the heat effect of varying laser power and scanning speeds on tissue with nonlinearity for different beam diameters. According to the generated guideline map, we predicted that depth-limited mucosal coagulation could be achieved for continuous wave 1500 nm laser exposure with 0.33-0.43 W/cm^2 (beam diameter of 1 mm and scanning

speed range from 1 mm/s to 3 mm/s). The white line on the map represented a threshold for damaged areas with a damage depth of 0.4 mm and above. We considered scanning speed, laser power, and beam diameter as combinations of parameters that can describe a depth of injury close to the

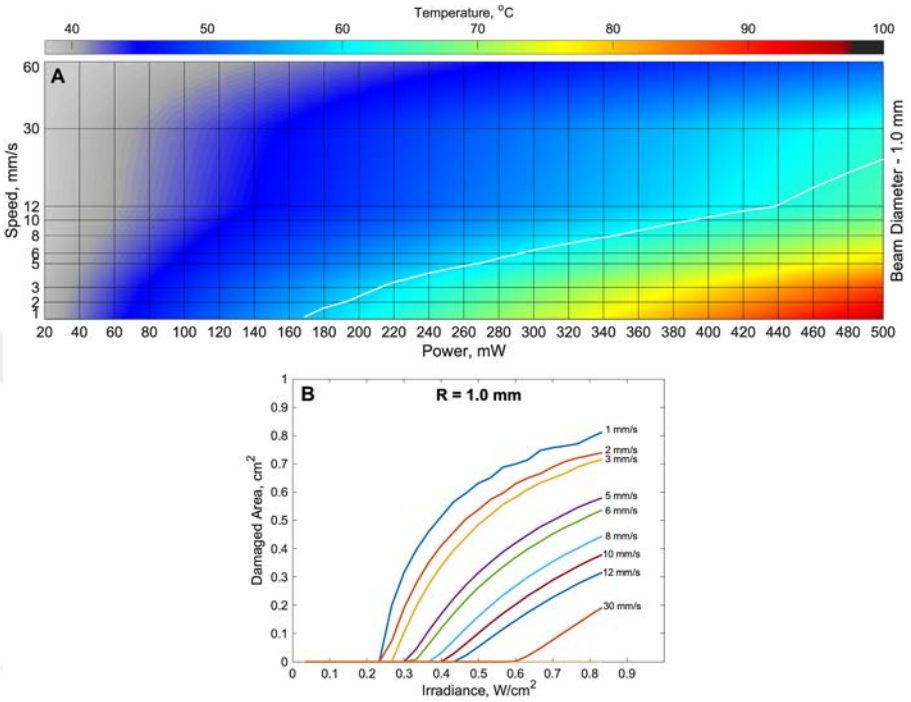


Figure 8. A map of the predicted peak mucosal temperatures during pulsed laser scanning on the x-axis as the function laser power for different scanning speeds with a laser beam diameter of 1 mm. The solid white line shows 98% proportional thermal damage calculated based on 60 °C critical temperature from laser irradiation. Y axes on the map are set in logarithmic scale (A). A graph of the damaged area as functions of scanning speed and irradiance for 1 mm of beam diameter pulsed laser (B).

mucosal thickness. In addition, although the applied laser energy was equal, the slower scanning speed provided deeper damage than the rapid scanning speed. The model also calculated that scanning performed at a longer time but at a higher rate resulted in shallower thermal damage than scanning performed at a low speed in a short time.

Similarly, a relatively deep and wide thermal effect of short-duration high power laser irradiation in continuous-wave mode has been also detected in the biological tissue sample [28] and agar-based gel [29]. With the evaluation made together, it has been revealed that the application method (fixed/moving) as well as the amount of laser energy applied has undeniable effects on the resulting thermal energy.

Although the calculated values give an insight into the laser parameters for well-confined photothermal damage, a few points should be briefly discussed to improve the computer modeling approach further:

1. This study assumes that the tissue's absorption and scattering coefficients and thermal properties are constant during laser radiation. The effect of temperature change on tissue structure is neglected.

2. Since dynamic blood flow significantly affects heat dissipation, more complex tissue structures, including blood vessels, may also need to be investigated to analyze heat dissipation.

3. An area scan simulation can be performed instead of just a linear scan to expand the variable matrix that makes up the map for a comprehensive analysis.

4. Computer modeling can be validated by planning in vivo experimental studies in an appropriate animal model.

In conclusion, this study successfully demonstrated a computer modeling approach that can complement future preclinical and clinical photothermal coagulation studies. The approach's applicability for various parameters provides an opportunity to advance improvements. With the numerical specification of the parameters for adequate photothermal coagulation, the necessity for repeated preclinical studies will be decreased.

Acknowledgment

This work was supported partially by TÜBİTAK grant no. 117E985, and the European Union's Horizon 2020 Research and Innovation Programme under the Marie Skłodowska-Curie grant agreement no. 835907. Merve
Turker Burhan was supported by a Turkish Council of Higher Education 100/2000 and BİDEB 2211-A doctoral scholarships.

References

[1] Chung C-S, Wang H-P. Screening for precancerous lesions of upper gastrointestinal tract: from the endoscopists' viewpoint. Gastroenterology Research and Practice 2013; 2013 681439: 1-18. doi: 10.1155/2013/681439

[2] Martinucci I, de Bortoli N, Russo S, Bertani L, Furnari M et al. Barrett's esophagus in 2016: From pathophysiology to treatment. World Journal of Gastrointestinal Pharmacology and Therapeutics 2016; 7 (2): 190-206. doi: 10.4292/wjgpt.v7.i2.190

[3] Garud SS, Willingham FF, Cai Q. Diagnosis and management of Barrett's esophagus for the endoscopist. Therapeutic Advances in Gastroenterology 2010; 3 (4): 227-238. doi: 10.1177/1756283X10365439

[4] Watson TJ. Endoscopic therapies for Barrett's neoplasia. Journal of Thoracic Disease 2014; 6 (SUPPL.3): 298-308. doi: 10.3978/j.issn.2072-1439.2014.03.35

[5] Kallam A, Alsop BR, Sharma P. Limitations of endoscopic ablation in Barrett's esophagus. Expert Review of Gastroenterology and Hepatology 2015; 9 (4): 487-496. doi: 10.1586/17474124.2015.976554

[6] Hohmann M, Lengenfelder B, Kanawade R, Klämpfl F, Douplik A et al. Measurement of optical properties of pig esophagus by using a modified spectrometer set-up. Journal of Biophotonics 2018; 11 (1). doi: 10.1002/jbio.201600187

[7] Ribeiro SR, Pinto PE Jr, de Miranda AC, Bromberg SH, Lopasso FP et al. Weight loss and morphometric study of intestinal mucosa in rats after massive intestinal resection: influence of a glutamine-enriched diet. Revista do Hospital das Clinicas da Faculdade de Medicina da Universidade de Sao Paulo 2004; 59 (6): 349-356. doi: 10.1590/s0041-87812004000600007

[8] Ashraf O, Patel NV, Hanft S, Danish SF. Laser-Induced Thermal Therapy in Neuro-Oncology: A Review. World Neurosurgery 2018; 112: 166-177. doi: 10.1016/j.wneu.2018.01.123

[9] Schena E, Saccomandi P, Fong Y. Review Laser Ablation for Cancer: Past, Present and Future. Journal of Functional Biomaterials 2017; 8 (2): 1-15. doi: 10.3390/jfb8020019

[10] Stafford RJ, Fuentes D, Elliott AA, Weinberg JS, Ahrar K. Laser-Induced Thermal Therapy for Tumor Ablation. Critical Review in Biomedical Engineering 2010; 38 (1): 79-100. doi: 10.1615/CritRevBiomedEng.v38.i1.70

[11] Marmur ES, Schmults CD, Goldberg DJ. A Review of Laser and Photodynamic Therapy for the Treatment of Nonmelanoma Skin Cancer. Dermatologic Surgery 2004; 30: 264-271. doi: 10.1111/j.1524-4725.2004.30083

[12] Carroll L, Humphreys TR. Laser-tissue interactions. Clinics in Dermatology 2006; 24 (1): 2-7. doi: 10.1016/j.clindermatol.2005.10.019

[13] von Maltzahn G, Centrone A, Park JH, Ramanathan R, Sailor MJ et al.Sers-coded gold nanorods as a multifunctional platform for densely multi-plexed near-infrared imaging and photothermal heating. Advanced Materials 2009; 21: 3175-3180. doi: 0.1002/adma.200803464

[14] Lee H, Lee Y, Song C, Cho HR, Ghaffari R et al. An endoscope with integrated transparent bioelectronics and theranostic nanoparticles for colon cancer treatment. Nature Communications 2015; 6: 1-10. doi: 10.1038/ncomms10059

[15] Tuttle BW, Seibel EJ. Delivery of therapeutic laser light using a single mode silica fiber for a scanning fiber endoscope system. Proceedings of SPIE 2006; 6083 (608307): 1-12. doi: 10.1117/12.648228

[16] Blank ABM, Friedrich M, Hamilton JD, Lee P, Berg J et al.Laser scanning dental probe for endodontic root canal treatment. Proceedings of SPIE 2011; 7884 (788403): 1-7. doi: 10.1117/12.875274

[17] Metropolis N, Ulam S. The Monte Carlo method. Journal of the American Statistical Association 1949; 44 (247): 335-341.

[18] Wilson BC, Adam G. A Monte Carlo model for the absorption and flux distributions of light in tissue. Medical Physics 1983; 10 (6): 824-830. doi: 10.1118/1.595361

[19] Flock ST, Patterson MS, Wilson BC, Wyman DR. Monte-Carlo modeling of light-propagation in highly scattering tissues. I. Model predictions and comparison with diffusion theory. IEEE Transactions on Biomedical Engineering 1989; 36 (12): 1162-1168. doi: 10.1109/TBME.1989.1173624

[20] Wang LH, Jacques SL, Zheng Z. MCML - Monte-Carlo modeling of light transport in multilayered tissues. Computer Methods and Programs in Biomedicine 1995; 47 (2): 131-146. doi: 10.1016/0169-2607(95)01640-F

[21] Pennes HH. Analysis of Tissue and Arterial Blood Temperature in the Resting Human Forearm. Journal of Applied Physics 1948; 1: 93-102. doi: 10.1152/jappl.1948.1.2.93

[22] Henriques FC, Moritz AR. Studies of Thermal Injury: I. The Conduction of Heat to and through Skin and the Temperatures Attained Therein. A Theoretical and an Experimental Investigation. The American Journal of Pathology 1947; 23 (4): 531-549.

[23] Liu JB, Miller LS, Goldberg BB, Feld RI, Alexander AA et al. Transnasal US of the esophagus: Preliminary morphologic and function studies. Radiology 1992; 184 (3): 721-727. doi: 10.1148/radiology.184.3.1509056

[24] Taniguchi DK, Martin RW, Trowers EA, Silverstein FE. Simultaneous M-mode echoesophagram and manometry in the sheep esophagus. Gastrointestinal Endoscopy 1995; 41 (6): 582-586. doi: 10.1016/S0016- 5107(95)70195-8.

[25] Bashkatov AN, Genina EA, Kochubey IV, Gavrilova AA, Kapralov SV et al. Optical properties of human stomach mucosa in the spectral range from 400 to 2000 nm: Prognosis for gastroenterology. Medical Laser Application 2007; 22 (2): 95-104. doi: 10.1016/j.mla.2007.07.003

[26] Collins CM, Smith MB, Turner R. Model of local temperature changes in brain upon functional activation. Journal of Applied Physiology 2004; 97: 2051-2055. doi: 10.1152/japplphysiol.00626.2004

[27] Diller KR, Klutke GA. Accuracy analysis of the Henriques model for predicting thermal burn injury. In: Proceedings of the 1993 ASME Winter Annual Meeting, New Orleans, LA, USA; 1993.

[28] Kopyeva MS, Filatova SA, Kamynin VA, Trikshev AI, Kozlikina EI et al. Ex-vivo Exposure on Biological Tissues in the 2-μm Spectral Range with an All-Fiber Continuous-Wave Holmium Laser. Photonics 2022; 9 (1): 20. doi: 10.3390/photonics9010020

[29] Fichera L. Modeling the Laser Ablation Process. In: Cognitive Supervision for Robot-Assisted Minimally Invasive Laser Surgery. Springer Thesis. Springer, Cham, 2016; pp. 63-78.